Heteroaggregation processes in colloidal particle and cell systems

Dissertation
zur Erlangung des akademischen Grades

Doktoringenieur
(Dr.-Ing.)

von: Dipl.-Ing. Sascha Rollié
geb. am: 17. April 1979
in: Oelde

genehmigt durch die Fakultät für Verfahrens- und Systemtechnik
der Otto-von-Guericke-Universität Magdeburg

Gutachter: Prof. Dr.-Ing. habil. Kai Sundmacher
Prof. Dr. techn. Johannes Khinast

eingereicht am: 1. März 2010
Promotionskolloquium am: 27. April 2010

Forschungsberichte aus dem Max-Planck-Institut
für Dynamik komplexer technischer Systeme

Band 26

Sascha Rollié

Heteroaggregation processes in colloidal particle and cell systems

Shaker Verlag
Aachen 2010

Bibliographic information published by the Deutsche Nationalbibliothek
The Deutsche Nationalbibliothek lists this publication in the Deutsche Nationalbibliografie; detailed bibliographic data are available in the Internet at http://dnb.d-nb.de.

Zugl.: Magdeburg, Univ., Diss., 2010

Printed in Germany.

ISBN 978-3-8322-9171-6
ISSN 1439-4804

Shaker Verlag GmbH • P.O. BOX 101818 • D-52018 Aachen
Phone: 0049/2407/9596-0 • Telefax: 0049/2407/9596-9
Internet: www.shaker.de • e-mail: info@shaker.de

Zusammenfassung

Motiviert durch die selektive Adsorption von funktionalisierten Wirkstoffträgerpartikeln an bestimmte Zelltypen für medizinische Anwendungen werden in dieser Arbeit grundlegende Heteroaggregationsphänomene unter besonderer Berücksichtigung des dynamischen Verhaltens in physikalischen und biologischen Modellsystemen untersucht. Die Adsorption von Antikörpern als mögliche funktionelle Einheit an Rezeptoren auf Zelloberflächen stellt einen entscheidenden ersten Schritt in einer Reihe weiterer Transportbeschränkungen bei der zellulären Aufnahme funktionalisierter Wirkstoffträgerpartikel dar. Zur Etablierung geeigneter wissenschaftlicher Methoden für die Analyse von selektiven und kompetitiven Heteroaggregationsprozessen, wurden spezifische Interaktionen sowie die Heteroaggregation von mehreren unterschiedlichen kolloidalen Spezies zunächst in physikalischen Partikelsystemen untersucht. Die experimentellen Methoden umfassen vorrangig die Durchflusszytometrie sowie diverse mikroskopische Verfahren, während die Simulationen auf Populationsbilanzgleichungen basieren mit Kernen, die in klassischen kolloidchemischen Grundlagen wurzeln. Beide Ansätze wurden auf biologische Systeme angewendet, um eine quantitative Beschreibung der Dynamik und Effizienz von medizinischen Wirkstoffapplikationsprozessen zu erreichen. Dies könnte sich als wertvoll für künftige Optimierungsbestrebungen erweisen.

Zur Bestimmung der Aggregatzusammensetzung und ihrer Dynamik in Heteroaggregationsprozessen hat sich die Durchflusszytometrie als leistungsfähiges Messverfahren erwiesen. Sie ermöglicht eine unabhängige und sehr detaillierte Auflösung mehrdimensionaler Verteilungen durch eine zuverlässig automatisierte Einzelpartikelanalyse. Die Untersuchungen in binären und ternären Partikelgemischen fokussieren auf elektrostatische De- und Restabilisierungseffekte, die durch die Auswahl geeigneter Partikelspezies und deren Mischungsverhältnis maßgeblich gesteuert werden können. Die experimentellen Ergebnisse wurden mit mehrdimensionalen deterministischen Populationsbilanzen nachgestellt, in denen die internen Koordinaten die Partikelanzahl der jeweiligen Spezies in einem Aggregat abbilden. Der physikalisch diskrete Eigenschaftsraum wurde adaptiv mit einer semi-heuristischen Methode so reduziert, dass nur Eigenschaftskoordinaten mit hohen Partikelkonzentrationen im Modell berücksichtigt werden. Die verwendeten Aggregationskerne basieren auf deterministischen Modellen aus der Kolloidchemie, insbesondere der DLVO Theorie, und verknüpfen die Interaktionen auf der Einzelpartikelskala mit dem makroskopischen Verhalten mehrerer Partikelpopulationen. Die an Partikelsystemen entwickelten Methoden wurden erfolgreich für eine systematische, modellgestützte Aufklärung präferentieller Aggregationsprozesse in einem ternären System aus Antikörpern und zwei humanen Tumorzelllinien (KARPAS-299 und U-937) eingesetzt. Trotz angenommener instantanter Aggregation bei Rezeptor-Ligand-Kollisionen, verursacht die geringe Rezeptorkonzentration auf den Zelloberflächen einen ratenlimitierten Aggregationprozess (engl.: *rate limited cluster aggregation*, RLCA). Populationsbilanzsimulationen mit Kernen, die stark heterogene Oberflächenstukturen der aggregierenden Spezies berücksichtigen (*patchy particles*), bestätigen die experimentellen Befunde. Die zielgerichtete Verabreichung pharmazeutischer Wirkstoffe mittels funktionalisierten Trägerpartikeln an spezifische Zellen unter Minimierung nachteiliger Beeinflussung anderer Zelltypen (*targeted drug delivery*) stellt ein potentielles Anwendungsgebiet dieser Ergebnisse dar.

Abstract

Motivated by the selective adsorption of functionalised drug carrier particles to certain cell types for medical applications this thesis investigates fundamental heteroaggregation phenomena under special consideration of the dynamic behaviour in physical and biological model systems. The adsorption of antibodies as possible functional moieties to receptors on cell surfaces represents an essential first step in a series of further transport limitations for the cellular uptake of functionalised drug carrier particles. To establish suitable scientific methods for the analysis of selective and competitive heteroaggregation processes, the specific interaction and heteroaggregation of multiple colloid constituents was studied in physical particle systems first. Experimental methods primarily include flow cytometry and diverse microscopic techniques, while simulations are based on population balance equations with kernel models rooting in classical colloid science. Both approaches were transferred to biological systems to achieve a more rigorous description of drug delivery dynamics and efficiency. This could prove valuable for future optimisation efforts.

Flow cytometry was established as a very powerful and convenient tool to characterise cluster composition and its dynamics in heteroaggregation processes. It enables an independent and very detailed resolution of multidimensional distributions by a reliably automated single particle analysis. Investigations in binary and ternary particle mixtures focus on electrostatic de- and restabilisation phenomena, that can be tailored by the choice of suitable particle species and their mixing ratio. Experimental results were reconstructed by multivariate population balance simulations in which the internal coordinates represent the particle number of the respective species inside an aggregate. The physically discrete property state space was adaptively reduced by a semi-heuristic approach, so that only property coordinates featuring high aggregate concentrations were considered in the model. The applied aggregation kernels are based on deterministic models from colloid science, in particular DLVO theory, and connect interactions on the single-particle level with the macroscopic behaviour of multiple particle populations. The methods established for particle systems were successfully transferred to a systematic, model-based investigation of preferential aggregation processes in a ternary system of antibodies and two human tumour cell lines (KARPAS-299 and U-937). Despite the assumed instantaneous aggregation following receptor-ligand collisions, the low receptor expression on cellular surfaces causes a rate limited aggregation process (RLCA). Population balance simulations with kernels that consider the strong surface heterogeneities of the aggregating species (patchy particles) confirm the experimental results. The targeted administration of pharmaceutical compounds by functionalised carrier particles to specific cells under minimisation of adverse effects represents a potential area of application of these results.

Preface

The work presented within this thesis was conducted during my time as scientific employee at the Max Planck Institute for Dynamics of Complex Technical Systems in Magdeburg from May 2006 until April 2010.

My special thanks is directed to Prof. Dr. Kai Sundmacher for the interesting and challenging topic as well as for the granted trust and scientific freedom. I am very grateful for many fruitful and supportive discussions, the luxury to pursue what the topic demanded in a rather unconstrained fashion as well as making numerous participations at national and international conferences possible. Additional thanks I owe to Prof. Dr. Johannes Khinast (Technical University of Graz, Austria) for reviewing and evaluating my thesis.

In completing this work I have benefited from the help of many people. I would like to thank all of my collaborators, in particular Prof. Dr. Heiko Briesen, Prof. Dr. Uwe Lendeckel, Dr. Fabian Heitzeberg, Prof. Dr. Michael Naumann, Prof. Dr. Udo Reichl, Dr. Michael Kappl, Dr. Rüdiger Berger and Prof. Dr. Hans-Jürgen Butt for their scientific input and kind support. I address my sincere appreciation to Dr. Thomas Hempel for preparing numerous electron micrographs, some of which are presented in the thesis, and to the laboratory staff, especially to Bianka Stein for her boundless energy, refreshing creativity and jovial nature, but also to Markus Ikert for his patience in conducting the AFM measurements. I am further indebted to my students Jens Karschau, Britta Ebeling and Annika Willitzki who considerably supported my research activities as well as to Dipl.-Biotech. Josef Schulze Horsel for his support in flow cytometry and to Dr. Peter Heidebrecht and Dr. Björn Niemann for fruitful discussions.

I value the time I could spend with my colleagues and friends from the Max Planck Institute. Special thanks is directed to my colleagues from the Physical and Chemical Process Engineering group and from the Chair of Process Systems Engineering at the Otto-von-Guericke-University Magdeburg, in particular to my office mates and aisle neighbours, as well as to the entire support staff of the Max Planck Institute.

Finally, I am truly grateful for the continuous support and encouragement by my beloved family and dear friends throughout the course of the thesis.

Sascha Rollié Magdeburg, May 2010

Contents

List of symbols

Symbols that are only of local interest within the thesis will be explained where applied and are not included here.

Physical constants

e	Elementary charge	$1.6021 \cdot 10^{-19}$	[C]
ε_0	Dielectric static permittivity in vacuum	$8.8542 \cdot 10^{-12}$	$[\mathrm{A\,s\,V^{-1}\,m^{-1}}]$
h	Planck's constant	$6.6261 \cdot 10^{-34}$	[J s]
N_A	Avogardo's number	$6.0221415 \cdot 10^{23}$	$[\mathrm{mol^{-1}}]$
k_B	Boltzmann's constant	$1.3804 \cdot 10^{-23}$	$[\mathrm{J\,K^{-1}}]$
R	Universal gas constant	8.3143	$[\mathrm{J\,mol^{-1}K^{-1}}]$

Latin symbols

A	Hamaker constant	[J]
a	Surface-to-surface separation distance	[m]
B	Hydrodynamic correction factor	[−]
b	Hardness factor	[−]
C^m	Mean curvature	$[\mathrm{m^{-2}}]$
C	Electrical capacitance	[F]
$\mathcal{C}$	Fitting constant	[−]
c	Number concentration	$[\mathrm{m^{-3}}]$
c^M	Mass concentration	$[\mathrm{kg\,m^{-3}}]$
D	Diffusion coefficient	$[\mathrm{m^2\,s^{-1}}]$
d	Diameter	[m]
d_f	Fractal dimension	[−]
$\vec{e}$	Property coordinate vector	[a.u.]
F	Force	[N]
FL	Fluorescence intensity	[a.u.]
$FL^0_{/}$	Autofluorescence intensity	[a.u.]
FS	Forward scatter signal	[a.u.]
f	Number density function	$[\Pi_k^K\,[\mathrm{e_k}]^{-1}\ \mathrm{m^{-3}}]$
f_F	Probability function of formation	[−]
fl	Volume specific fluorescence intensity	$[\mathrm{a.u.\,m^{-3}}]$
g_i	Steric correction factor	[−]
i, j, k	Particle numbers	[−]
I	Ionic strength	$[\mathrm{mol\,m^{-3}}]$
J	Diffusive particle flux with superimposed drift	$[\mathrm{s^{-1}}]$
J_0	Diffusive particle flux	$[\mathrm{s^{-1}}]$
K	Cantilever spring constant	$[\mathrm{n\,m^{-1}}]$
k_f	Scaling factor	[−]

k^0	Extrapolated contact force	$[\mathrm{N\,m^{-1}}]$
l	Unreduced number of rows	$[-]$
$\overline{M}$	Molar mass	$[\mathrm{kg\,mol^{-1}}]$
$\mathcal{M}$	Mobility	$[\mathrm{m\,s^{-1}\,N^{-1}}]$
m	Mass	[kg]
N	Particle number	$[-]$
N_{11}	Number of collisions per encounter	$[-]$
N_i^{max}	Maximum number of surface receptors	$[-]$
n	Relative refractive index	$[-]$
P	Probability	$[-]$
P', P'', P	Particle or cluster	$[-]$
P^c	Probability of multiple collisions per encounter	$[-]$
$\mathcal{P}$	Property space	$[-]$
Q	Charge	[C]
r	Radius or radial coordinate	[m]
r^G	Radius of gyration	[m]
r_σ	Zero-potential separation	[m]
SS	Side scatter signal	[a.u.]
T	Temperature	[K]
t	Time	[s]
V	Potential energy	[J]
V_P	Particle volume	$[\mathrm{m^3}]$
$\dot{V}$	Flow rate	$[\mathrm{m^3\,s^{-1}}]$
W	Stability ratio	$[-]$
w_e	Velocity	$[[\mathrm{e_k}]\ \mathrm{s^{-1}}]$
w_x	Velocity	$[\mathrm{m\,s^{-1}}]$
x, y, z	Spatial coordinates	[m]
y	Property state of surrounding continuous phase	[a.u.]
z_i	Ion valency	$[-]$

Greek symbols

α	Scaling parameter	$[-]$
Γ_N	Transport across control volume boundary	$[\mathrm{s^{-1}}]$
γ	Excluded surface area	$[-]$
δ_{ij}	Kronecker function	$[-]$
ε_r	Relative static dielectric perimittivity	$[-]$
ζ	Zeta-potential	[V]
η	Dynamic viscosity	[Pa s]
κ^{-1}	Debye length	[m]
λ	Decay length or wavelength	[m]
ν_P	Dimensionless particle volume	$[-]$
ξ	Threshold value	$[-]$
ρ	Density	[a.u.]
Σ_N	Source / sink of control volume	$[\mathrm{s^{-1}}]$
σ_N	Source / sink of control volume	$[\Pi_\mathrm{k}^\mathrm{K}\,[\mathrm{e_k}]^{-1}\ \mathrm{m^{-3}\,s^{-1}}]$
σ	Surface charge density	$[\mathrm{C\,m^{-2}}]$
σ^2	Variance	[a.u.]
υ	Daughter particle number	$[-]$

ϕ	Covered surface fraction	$[-]$
$\phi_{N,e}$	Transport density, internal coordinates	$[\Pi_k^{K-1}\,[e_k]^{-1}\ m^{-3}\,s^{-1}]$
$\phi_{N,x}$	Transport density, external coordinates	$[\Pi_k^{K}\,[e_k]^{-1}\ m^{-2}\,s^{-1}]$
Ψ	Interaction potential	$[V]$
ω	Transfer frequency	$[s^{-1}]$
ω_{Agg}	Aggregation rate	$[m^3\,s^{-1}]$

Subscripts

0	Surface
∞	Infinite distance from surface
AB	Antibody
Agg	Aggregation
Ar	Argon
Br	Breakage
$CD13$	Cell surface protein, aminopeptidase N
$CD33$	Cell surface protein, myeloid-associated marker
c	Cantilever
dl	Diffuse layer
e	Internal coordinates of property space
em	Emission
ex	Excitation
$FITC$	Fluorescein isothiocyanate
$HeNe$	Helium-Neon
$hydr$	Hydration
$IgG1$	Cell surface protein, Immunoglobulin G
i	Ion
$KARPAS-299$	Human tumour cells (anaplastic large cell lymphoma)
M	Molar
MF	Melamine formaldehyde
m	Monolayer
mol	Molecular
Nuc	Nucleation
P', P'', P	Particle or cluster
PBS	Phosphate buffered saline
PE	Phycoerythrin
PI	Propidium iodide
PS	Polystyrene
p	Piezoelement
RhB	Rhodamine B
RL	Receptor-ligand interaction
$RPMI$	Roswell Park Memorial Institute cell culture medium
Sol	Solvation
s	Stern layer
$U-937$	Human tumour cells (histiocytic lymphoma)
x	External coordinates of property space

Supercripts

0	Surface
$+$	Source
$-$	Sink
$\pm$	Source and sink
add	Additional particles
B	Brownian
Born	Born interaction
C	Charge
D	Diffusive
E	Collision efficiency
eff	Effective
el	Electrostatic interaction
eq	Equilibrium
exp	Experimental
F	Collision frequency
hydr	Hydration
m	Mean
max	Maximum
min	Minimum
N	Particle number
NaCl	Sodium chloride
R	Reduced
rec	Receptor
sim	Simulated
sol	Solvation interaction
spec	Specific
tot	Total
unspec	Unspecific
vdW	Van der Waals interaction

Chapter 1
Introduction

With scientific progress over the past decade, activities on the micro- and nanoscale have greatly intensified and open up new possibilities for technological and industrial use. However, the processing of matter on these scales remains difficult since direct mechanical handling is usually not feasible, especially on the nanoscale. To overcome this limitation for particulate materials, natural self-assembly processes can be harnessed in a bottom-up approach to direct aggregation and the formation of new functional materials. In this context particles with tailored surface heterogeneities, like Janus particles, may attain an important function as building blocks[19,45,107,157].

An application of directed aggregation processes with strong impact is found in the recent field of nanomedicine. Within this rapidly evolving and highly interdisciplinary research area strong efforts are aimed at improving the delivery of pharmaceutical compounds by innovative drug targeting methods[112]. In this context directed aggregation processes between a carrier entity to which the drug is bound and the target cell represent one of the key issues in improving the efficiency of drug delivery processes and reducing adverse medical effects at the same time. Common carrier systems include micro- or nanoscale biodegradable particles or capsules and vesicles like liposomes with tailored surface properties in order to evade premature degradation by the immune system and to target specific cells, followed by an optimal release of the drug[34,91,112,129,139].

An abundant diversity of carrier design and drug release studies can be found in the literature[31,38,105,136,143,158]. Most of these, however, are of a qualitative experimental nature and lack a rigorous, quantitative approach by simulation. This can be attributed to the profound complexity and high level of interdisciplinarity that investigations of mammalian cells tend to present. Therefore, despite the possible scientific impact, only few simulation efforts exist - some in the field of virus infection - in which the transport process of a biological entity (e.g. antibody, protein, virus) or a drug carrier particle and its dynamics are investigated in detail along the route to the intracellular target destination[6,43,137,153].

From a chemical engineers point of view, this route constitutes three central transport limitations on the single cell level: transport from the medium to the cell surface, transport of adsorbed particles through the cell membrane and further intracellular transport or degradation mechanisms. The first issue represents the main focus of this thesis. In order to tackle the challenges, skills from diverse scientific disciplines, including biology, medicine, physics as well as colloidal and engineering sciences, can deliver valuable synergetic insights for an improved understanding and optimisation of drug targeting processes.

Motivation and scope

Attempting a more rigorous understanding of the targeted transport process to the cell surface, this thesis investigates the aggregation dynamics of model drug carrier particles to cellular surfaces experimentally and by simulation. Figure 1.1 schematically illustrates the scope of the thesis with the adopted structure.

Since directed assembly processes on the micro- and nanoscale are strongly related to colloidal sciences and aggregation / breakage phenomena in particular, preliminary studies in particle systems under exclusion of biological variabilities are conducted first. In these, the fundamental understanding of heteroaggregation between different species from the molecular scale towards the scale of a particle ensemble are attained. Model aggregation processes in multi-species particle systems are investigated by closely monitoring the dynamics of the cluster composition. For this purpose, flow cytometry on the experimental side and population balance modelling on the simulation side represent the central techniques extensively used during the investigations. Both satisfy the requirements to deal with multi-dimensionally distributed dynamic systems. Results for binary and ternary particle systems are analysed with respect to different mixing ratios and dosage experiments. They demonstrate the unmatched level of detail reached by the applied methods. The experimental heteroaggregation dynamics are successfully reconstructed by a bivariate population balance equation on a physically discrete and adaptively reduced state space. Literature models describing the aggregation rates under consideration of DLVO theory are extended to heteroaggregation in binary systems. The modified rate models are used as kernels in the population balance equation. In an attempt to explain

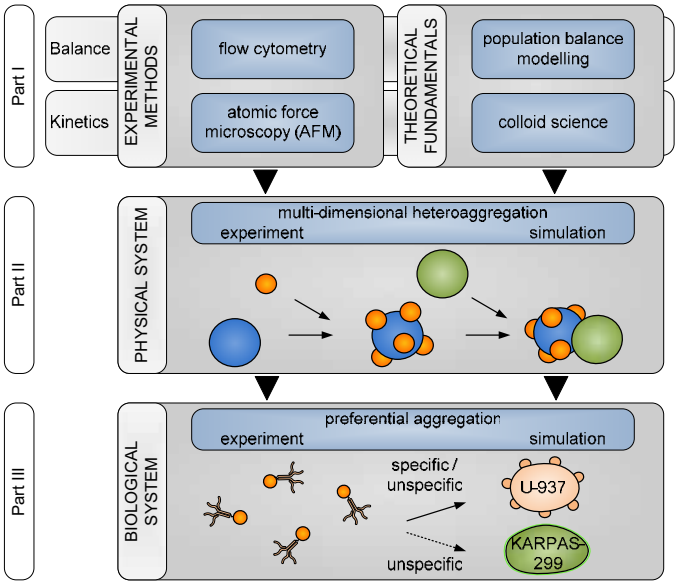

Figure 1.1: Schematic representation outlining the scope and structure of this thesis.

differences in macroscopic aggregation dynamics for diverse primary particles, the pair interaction energies on a single particle level are determined by colloidal probe microscopy. This approach aims at establishing the causality between microscopic interactions on the single particle level and the macroscopic aggregation behaviour of the different particle standards.

By means of the experimental and simulation methods developed with the model particle systems the targeted transport process to cell surfaces can now be investigated in a multi-species biological system (Figure 1.1). This second main pillar of the thesis focuses on cellular targeting in a mixed suspension of two model human tumour cell lines by antibody-antigen specific interactions. An interesting model system with a potential biomedical application is represented by aminopeptidase N (CD13) receptors on human tumour cells. Aminopeptidase N is known to represent a functionally important marker of angiogenically active vasculature and might represent an important marker for tumours[15,36,106,145]. The selective and specific drug delivery to these target cells thus represents a future application in therapeutic medicine. Bearing this in mind, preferential aggregation was studied with aminopeptidase N antibodies in a mixture of two human tumour cell lines differing with regard to their CD13 expression on the cellular surface. U-937 cells isolated from histiocytic lymphoma and KARPAS-299 cells from anaplastic large cell lymphoma were selected as cellular system. As in the particle systems, experimental investigations of aggregation dynamics by flow cytometry are complemented by population balance simulations. The aggregation kernels are adapted to biological interactions by non-DLVO interaction potentials between the aggregating entities. By means of simulation, the dynamics of larger biofunctionalised carrier particles with different surface characteristics could also be predicted.

In summary, this thesis combines aspects of colloidal sciences with dynamic population balance simulations for the application to biological systems in the area of preferential cell targeting to provide a more rigorous theoretical approach in describing the dynamics and efficiency of drug delivery processes.

The thesis was conducted under supervision of Prof. K. Sundmacher in his group Physical and Chemical Process Engineering at the Max Planck Institute for Dynamics of Complex Technical System in Magdeburg. Due to its complexity and the high level of interdisciplinarity the work was integrated into the activities of the Research Centre 'Dynamic Systems in Biomedicine and Process Engineering' at the Otto-von-Guericke-University Magdeburg. In particular, a cooperation with Prof. M. Naumann and Prof. U. Lendeckel (now at the Institute of Medical Biochemistry and Molecular Biology, Ernst-Moritz-Arndt University Greifswald) of the Institute of Experimental Internal Medicine was initiated. Experimental investigations with the atomic force microscope were supported by group of Prof. H.-J. Butt investigating the Physics of Polymers at the Max Planck Institute for Polymer Research in Mainz. Furthermore, in-house cooperations with Prof. U. Reichl of the Bioprocess Engineering group and Prof. H. Briesen (now chair of Process Systems Engineering at the Technical University of Munich) were launched.

Content and structure of the thesis

The scope of the thesis shown in Figure 1.1 inherently represents the adopted structure. Faced with the multitude of scientific disciplines, some having been developed over more than a century, only brief introductions to central theoretical and experimental aspects of colloidal science are provided in Part I. It first focuses on fundamental theoretical issues regarding the stability of colloidal dispersions in Chapter 2. This is followed by a short discussion of important experimental techniques to characterise colloidal suspensions, highlighting atomic force microscopy and flow cytometry in Chapter 3. Finally in Chapter 4, an overview of the simulation methods is given with special emphasis on population balance equations and their numerical solution. Based on these foundations, aggregation phenomena and their dynamics in multi-species colloid systems are studied in the following parts.

Part II focuses on electrostatically induced heteroaggregation in multi-species particle systems. The experimental results are presented in Chapter 5 for binary and ternary particle mixtures. These mainly rely on flow cytometric measurements, but also contain microscopic validations and electrophoretic measurements. Some results concerning the influence of the surface functionalisation on the aggregation dynamics are included in this chapter. By using particle species from two different manufacturers and employing colloidal probe microscopy on a single particle level, different macroscopic aggregation behaviour is explained on the population level between the two sets of polystyrene particle standards used in the respective experiments. For a more detailed understanding of the aggregation process, a bivariate population balance simulation is defined in Chapter 6 on a discrete state-space which was adaptively reduced by a semi-heuristic algorithm. The aggregation kernels are developed under consideration of literature models for perikinetic systems based on DLVO and non-DLVO interaction potentials. Simulation results show excellent agreement with experimental distribution data.

In Part III the fundamental insights on colloidal aggregation phenomena in multi-species mixtures are applied to a biological system. The investigations focus on the preferential aggregation of antibodies in an incubated mixture of human U-937 and KARPAS-299 tumour cells. This part is structured in accordance with Part II, first presenting the experimental results in Chapter 7, followed by the detailed development of the population balance model and a discussion of results in Chapter 8.

Apart from concise summaries following every milestone, concluding statements and a short outlook for the thesis as a whole are given in Chapter 9.

Part I

Theoretical and experimental background

Colloidal science concerns disperse phase systems in which one or more of the components has at least one dimension within the nanometre to micrometre range[135]. Technically important disperse phase systems involve numerous combinations of solid, liquid and gaseous substances, of which dispersed solid particles in a continuous liquid phase represent the most common class dealt with in the scope of colloidal science. Solid particles may include inorganic materials as well as organic polymer particles. Although polymers show different material properties compared to inorganic materials, giving rise for instance to swelling and gelation phenomena, their approximative treatment as solid is usually justified. For biological matter this approximation can often not be maintained, especially if the particulate phase consists of fluid volumes surrounded by flexible biomembranes, as is the case for cells or liposomes. Depending on membrane flexibility, deformations on the interface can exert dominant influences usually of hydrodynamic origin on the interaction properties between disperse elements. However, for the treatment within this thesis any detailed hydrodynamic analyses on the microscale are neglected and also biologically disperse elements are considered as particles. All particulate entities used within this thesis range between 10 nm and 10 μm in size and are thermodynamically unstable due to their high surface free energies.

Colloid science is a very interdisciplinary research area. Owing to the complexity of most colloidal systems, the subject often cannot be treated with the exactness that tends to be associated with the respective areas of physics and physical chemistry. It is probably a combination of this lack of precision and its interdisciplinary nature, rather than a lack of technical importance, that has favoured work with well-defined systems, like single component monodisperse suspensions or the use of pure surface active agents. Despite the large number of variables which are often involved, research of colloidal systems coupled with advances in understanding of the fundamental principles of physics and chemistry has made it possible to formulate coherent theories related to many aspects of colloidal behaviour. Since colloidal science can be understood at both descriptive and theoretical levels, the study of this area ranges widely from relatively simple descriptive material to extremely complex theory.

For well over a century colloids and their aggregation behaviour have been studied intensely, ever since focusing on stability as a central issue. Theoretical considerations culminated in a first coherent theory in the 1940's, which was developed independently by Derjagiun and Landau[23] as well as Verwey and Overbeek[151] and became known as DLVO theory. Because of its importance in describing the stability of colloidal materials, central aspects of DLVO theory are presented in Chapter 2. Hand in hand with theoretical progress, several techniques for the characterisation of colloidal materials have been developed, most of them relying on the diffraction of light transmitted through a sample, like microscopic and scattering techniques. Some important methods that were employed within this thesis, like atomic force microscopy and flow cytometry, are discussed in Chapter 3. This is followed by a short introduction into modelling tools used to describe aggregation dynamics in colloidal dispersions. Population balance treatments date back to von Smoluchowski's seminal paper of 1917. With the advent of computer technology, modelling methods were considerably extended beyond the realm of analytical solutions. Numerical solutions of predictive models, like population balances or molecular modelling, were complemented by stochastic Monte Carlo methods. A brief overview of the most important methods in the context of colloidal aggregation phenomena is presented in Chapter 4.

Chapter 2

Stability of colloidal dispersions

A characteristic feature of colloidal dispersions is the large area-to-volume ratio for the particles involved[135]. At the interface between the dispersed phase and the dispersion medium, characteristic surface properties, such as adsorption and electric double layer effects, play a very important role in determining the physical properties of the system. But despite the high area-to-volume ratio, the amount of surface-active material required to achieve modification of the interfaces in a typical colloidal dispersion can be quite small because the material within some molecular layers of the interface exerts by far the greatest influence on particle-particle and particle-dispersion interactions. Substantial changes of the bulk properties can thus be effected by small quantities of suitable additives. A very important physical property of colloidal dispersions affected by surface additives is the tendency of the particles to aggregate. Depending on particle concentration, encounters between particles dispersed in liquid media may occur frequently and the stability of a dispersion is determined by the interaction between the particles during these encounters.

Colloidal stability is influenced by a variety of mechanisms. Apart from steric interactions which play a decisive role for rough polymeric surfaces where segments of lyophilic polymer chains extend some distance into the dispersion medium, potential interaction energies between the particle surfaces exert an essential influence on the aggregation behaviour. It is by tuning these interaction potentials, that aggregation can be tailored according to technical demands for designed processes. All predominant forces between colloidal particles arise from electromagnetic interactions on the molecular scale. This is encapsulated in the Hellman-Feynman theorem, which states that once the spatial distribution of the electron clouds has been determined by solving the Schrödinger equation, the intermolecular forces may be calculated on the basis of classical electrostatics[68]. But since exact solutions of the Schrödinger equation are not easily accessible, it has been found useful to classify intermolecular forces into a number of seemingly different categories, such as van der Waals, Coulombic and solvation forces, hydrophobic interactions as well as ionic and hydrogen bonding, often accompanied by further divisions into strong and weak or short ranged and long ranged interactions.

Regarding the range of interaction, three main areas of recent activities can be identified[68], two of which investigate short ranged forces in quantum mechanical or statical mechanical approaches to describe chemical bonding in solids or to derive physical bulk properties of single atoms or molecules. The third deals with the long range interactions between surfaces and small particles in colloid science. Here, effects at short range take place at very close to molecular contact (< 1 nm) and long range forces are rarely important beyond 100 nm[68]. A rough categorisation of typical in-

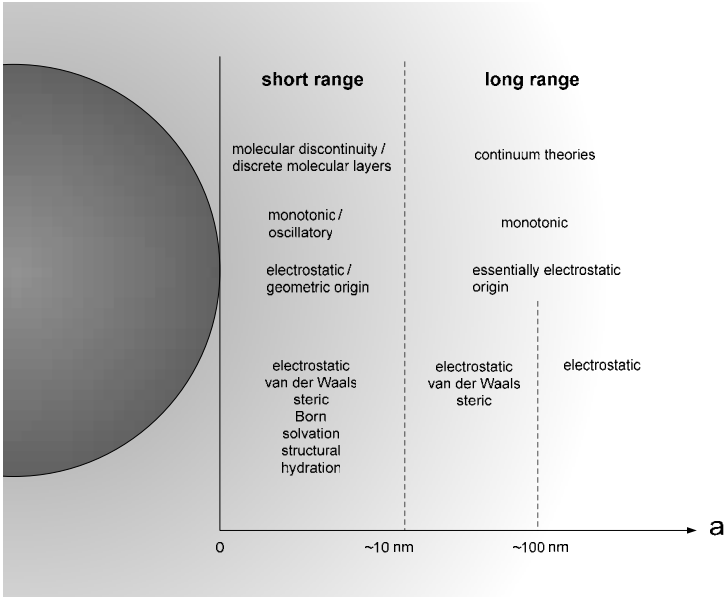

Figure 2.1: Overview and categorisation of interactions between particles.

teractions and their theoretical descriptions is presented in Figure 2.1 in dependence of the separation distance between two solid surfaces. While molecular theories attempt to describe the long range interactions all the way from atomic dimensions, the central focus of this thesis is directed at continuum models that apply for interactions beyond the molecular scale. Although the assumption that some of the bulk properties hold right down to the molecular scale presents some serious conceptual problems and neglects some highly specific solvent effects, for example expressed by oscillating interaction forces at separation distances of molecular dimensions[68], these models present an acceptable level of approximation for the length scales examined in this thesis.

In the following sections, first the electrical properties at solid-liquid interfaces will be discussed, before potential interaction energies are derived for macroscopic spheres which are used to assess the stability in a colloidal mixture.

2.1 Electrical properties of interfaces

Most substances acquire an electric surface charge when brought into contact with a liquid medium. Possible charging mechanisms depend on the chemical composition and include ionisation, ion adsorption or ion desorption. For example oxides usually develop a surface charge as result of adsorption or desorption of protons, hydroxide or other dissolved ions, while in salt-like colloids ions adsorb to the surface and produce surface charge. A prominent example is solid silver-iodine, where iodine ions preferentially adsorb to the surface of AgI crystals and reduce the point of zero

charge from $p\mathrm{Ag} = 8$ as expected from the solubility product to $p\mathrm{Ag} = 5.7$[78]. The surface charge at solid interfaces influences the distribution of nearby ions in the surrounding liquid phase. Ions of opposite charge (counter-ions) are attracted towards the surface and ions of like charge (co-ions) are repelled. In combination with thermal motion, the interactions between immobile and mobile charges gives rise to an electric double layer, with an excess of neutralising counter-ions over co-ions distributed near the charged surface in a diffuse manner. Despite the local separation of electrical charges, the condition of electro-neutrality is always maintained for the total system.

2.1.1 Electrical double layer

The adsorption of mobile charges at solid-liquid surfaces was first treated by Helmholtz[55] in 1853. In his model, the charged solid surface is covered by a single layer of oppositely charged counter-ions referred to as Helmholtz layer. Gouy[46] and Chapman[18] independently refined this theory in the early 20th century by replacing the single counter-ion layer by an exponentially decreasing ion concentration layer. This is achieved if the concentration of the counter-ions is assumed to be Boltzmann distributed at chemical equilibrium. In 1924 Otto Stern drew attention to contradictions encapsulated in the Gouy-Chapman model, which become especially apparent for highly charged surfaces, and offered a solution by combining both concepts[142]. In his model of an electric double layer, the charged solid surface is covered by an immobile compact layer of counter-ions (Stern layer) followed by a diffuse layer of mobile charges analogous to Gouy-Chapman's diffuse layer. The main assumptions include a flat uniformly charged surface of infinite extent, point charge ions, a dielectric permittivity constant throughout the double layer and equal to the bulk value, as well as the restriction to a single symmetric electrolyte. Despite its limitations, the combined Gouy-Chapman-Stern model is still frequently applied. In later years the double layer theory was subject to further modifications with ever increasing levels of detail. For ions not longer considered as point charges, two layers within the Stern model were introduced: one with strongly adsorbed pure counter-ions, referred to as the inner Helmholtz plane, and a second layer of slightly larger solvated counter-ions in the outer Helmholtz plane[47]. In the treatment of aggregation adopted in this thesis, the prediction of colloidal stability is predominantly influenced by the long range interactions between the particles. The Gouy-Chapman model, which accounts for the diffuse part of the electrical double layer, provides a sufficient level of detail for describing the electrostatic effects in colloidal suspensions with long range interaction energies. To this end, substitute particles are defined by the solid particles including their surrounding Stern shell. Therfore the Gouy-Chapman model without any Stern layer is described in the following.

A detailed analysis of the electrostatic field surrounding a solid interface in an electrolyte solution, requires knowledge about the ion distributions. As mentioned before, counter-ions with charges opposite in sign to the surface charge will be attracted and like-charged co-ions will be repulsed, while the charge balance condition is maintained globally. At the same time, each ion participates in the randomising thermal motion of the solution. The electrostatic potential of distributed charges must sat-

isfy the Poisson equation, which relates the mean force potential Ψ to the electric free charge density ρ_{dl}^{C} [127].

$$\nabla \cdot (-\varepsilon_0 \varepsilon_r \nabla \Psi) = \rho_{dl}^{C} \tag{2.1}$$

with ε_0 as vacuum and ε_r as relative static dielectric permittivity. Because the ions in the diffuse region are considered to be in equilibrium, the force which equals the gradient of the mean electrostatic potential Ψ^m must vanish in [68,127]

$$k_B T \nabla \ln c_i + z_i e \nabla \Psi^m = 0 \tag{2.2}$$

with c_i as ion concentration in the diffuse layer with valency z_i and e as elementary charge. From Eq. (2.2) the Boltzmann distribution of the ion concentration follows as

$$c_i = c_{i,\infty} \exp\left(-\frac{z_i e \Psi^m}{k_B T}\right) . \tag{2.3}$$

Recognising that the free charge density ρ_{dl}^{C} equals the local excess of ionic charge arising from N ionic species $\rho_{dl}^{C} = \sum_{i=1}^{N} z_i e c_i$ and assuming that the potential of mean force Ψ is equal to the average electrostatic potential Ψ^m, the Poisson-Boltzmann equation is derived as [127]

$$\varepsilon_0 \varepsilon_r \nabla^2 \Psi = -e \sum_{i=1}^{N} z_i c_{i,\infty} \exp\left(-\frac{z_i e \Psi}{k_B T}\right) . \tag{2.4}$$

It represents the basis of the Gouy-Chapman model of the diffuse layer surrounding an electrically charged surface. For a diffuse layer near a flat half-plane for a single z_i-z_i electrolyte, we obtain

$$\frac{\mathrm{d}^2 \Psi}{\mathrm{d}x^2} = \frac{2 e z_i}{\varepsilon_0 \varepsilon_r} c_i \sinh\left(\frac{e z_i \Psi}{k_B T}\right) , \tag{2.5}$$

with x indicating the distance from the half-plane. Linearisation of sinh for small dimensionless potentials $e z_i \Psi / (k_B T) \ll 1$ leads to the Debye-Hückel approximation

$$\frac{\mathrm{d}^2 \Psi}{\mathrm{d}x^2} = \frac{2 e^2 z_i^2 c_i}{\varepsilon_0 \varepsilon_r k_B T} \Psi = \kappa^2 \Psi . \tag{2.6}$$

The prefactor on the right hand side of Eq. (2.6) expresses the Debye decay length κ^{-1}, which represents a measure for the extent of the diffuse double layer. The dimensionless quantity κr_P represents the ratio of curvature to the double layer thickness and is frequently used to generate approximate solutions. For small κr_P, a charged particle may be treated as a point charge; for large κr_P, the double layer is effectively flat [29]. From Eq. (2.6) we obtain an exponential decay of the potential within the diffuse layer following $\Psi = \Psi_{dl} \exp(-\kappa x)$. Due to the condition of global electroneutrality, the potential at the surface balances all diffuse charges $\sigma_0 + \sigma_{dl} = 0$ in the Gouy-Chapman model. The area specific surface charge σ_0 is obtained by integrating over the charge density ρ_{dl}^{C}

$$\sigma_0 = -\sigma_{dl} = -\int_0^\infty \rho_{dl}^{C} \mathrm{d}x , \tag{2.7}$$

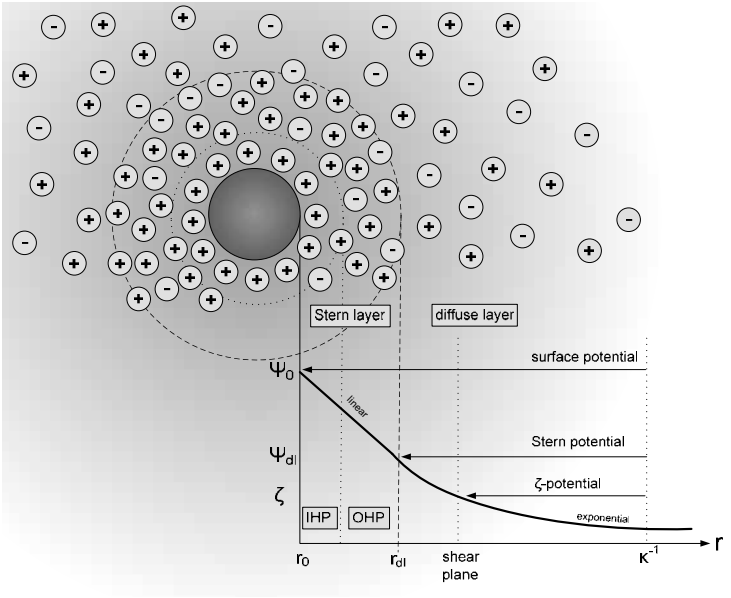

Figure 2.2: Schematic illustration of the electrostatic double layer surrounding a negatively charged particle in an electrolyte solution with positive and negative ions. (IHP: inner Helmholtz plane, OHP: outer Helmholtz plane)

and by applying the Poisson-Boltzmann distribution $\rho_{dl}^{C} = \varepsilon_0 \varepsilon_r \nabla^2 \Psi$, we obtain[127,135]

$$\sigma_0 = \sqrt{8\varepsilon_0 \varepsilon_r k_B T c_i} \sinh \frac{e z_i \Psi_0}{2 k_B T} \approx \varepsilon_0 \varepsilon_r \kappa \Psi_0 \tag{2.8}$$

for the surface charge with the Debye-Hückel approximation for low surface potentials Ψ_0.

The treatment of the diffuse double layer so far is based on the assumption of point charges in the electrolyte medium. The finite size of the ions will, however, limit the inner boundary of the diffuse part of the layer, since the centre of an ion can only approach the surface to within it hydrated radius without becoming specifically adsorbed[135]. The diffuse layer was complimented with a plane located at about a hydrated ion radius from the surface by Stern in 1924, thus establishing the theory of an electric double layer. This concept is illustrated in Figure 2.2. Since the Stern layer contains charge, the electroneutrality condition now reads as $\sigma_0 + \sigma_s + \sigma_{dl} = 0$, where σ_{dl} in the diffuse part of the layer is given by Eq. (2.8) with the sign reversed and with Ψ_0 replaced by Ψ_{dl}.

In his theory Stern assumed a Langmuir-type adsorption isotherm to describe the equilibrium between the ions adsorbed in the Stern layer and those in the diffuse part

of the double layer[142]. Considering only the adsorption of counter-ions, the surface charge density σ_s is given by[135]

$$\sigma_s = \frac{\sigma_m}{1 + \frac{N_A}{n_{i,\infty} v_{M,i}} \exp\left[\frac{z_i e \Psi_{dl} + V_{vdW}}{k_B T}\right]} \tag{2.9}$$

where σ_m is the surface charge density corresponding to a monolayer of counter-ions and the fraction $N_A / (n_{i,\infty} v_{M,i})$ represents the molar fraction of solvated substance i with N_A as Avogadro's constant, $v_{M,i}$ as molar volume and $n_{i,\infty}$ as solvated amount of moles. The adsorption energy is separated into electrical $z_i e \Psi_{dl}$ and van der Waals Ψ_{vdW} terms.

Within the Stern layer the ions are assumed to be represented by point charges confined to the Stern layer at $x = x_{dl}$[142]. Since measurements indicate that the thickness of the Stern layer ranges around 0.5 nm, so that only a few layers of solvent molecules can be accommodated[64], this approximation is exact enough for our long-range considerations. Thus assuming a region $0 < x < x_{dl}$ free of any charges, the potential difference follows from the Poisson equation as[64]

$$\Psi_0 - \Psi_{dl} = \frac{\sigma_0 x_{dl}}{\overline{\varepsilon_0 \varepsilon_r}} \tag{2.10}$$

where $\overline{\varepsilon_0 \varepsilon_r}$ is an average permittivity over the inner layer region. For constant permittivity Eq. (2.10) thus predicts a linear change in potential.

Before we move on to issues of colloidal stability in which double layer interactions can play a decisive role, a generalised approach is sketched, by which the above interactions between flat planes can be transferred to macroscopic bodies of different geometries. The main types of interaction energies are then shown for spherical geometries.

2.2 Interaction potentials between macroscopic bodies

The potential energy of two macroscopic particles with respect to each other can be obtained, in principle, in two different ways. Either one may try to find an expression for the force between the particles as a function of their distance, or one may determine the free energy difference of the system as a function of the distance[151]. Both methods are equivalent and in the following some light is shed on the first method.

The simplest procedure to calculate the interaction energies between two macrobodies is to use the method of pairwise summation of given intermolecular energies. In a N-body system this is given by

$$V_{mol}^{1,2,\ldots,N} = \frac{1}{2} \sum_{i=1}^{N} \sum_{j=1(\neq i)}^{N} V_{mol}^{ij}\left(r_{ij}\right) \tag{2.11}$$

where $V_{mol}^{ij}\left(r_{i,j}\right)$ is the interaction energy of molecules i and j separated by distance r_{ij} in the absence of any other molecules[64]. Clearly, the error will be least when the molecules are far from one another, so that the individual pair interactions are rela-

tively unaffected by the presence of other molecules. By assuming pairwise additivity and integrating out all molecular interactions in both macroscopic bodies, the interaction energies between two flat half-planes can be derived[64,68].

Interactions between macroscopic shapes of simple geometry can then be calculated by integrating over area specific interaction energies of locally flat parallel half-planes[64]. This approximation holds best, when the distance of closest approach is small compared to the radii of curvature of the two bodies. From this a very useful approximate expression for the interaction energy of the bodies can be derived, as was first done by Derjaguin[24]. A general expression for any type of interaction potential between macroscopic bodies of arbitrary geometry is given by[64]

$$V_{P',P''}(a) = \int_a^\infty F(a')\ \mathrm{d}a' = \frac{2\pi}{\sqrt{C^m}} \int_a^\infty E_{planes}(a')\ \mathrm{d}a' \tag{2.12}$$

where E_{planes} denotes the area specific interaction energy between two half-planes and the mean curvature C^m is given by

$$C^m = \left(\frac{1}{r^{(1)}_{P'}} + \frac{1}{r^{(1)}_{P''}}\right)\left(\frac{1}{r^{(2)}_{P'}} + \frac{1}{r^{(2)}_{P''}}\right) + \sin^2\phi \left(\frac{1}{r^{(1)}_{P'}} - \frac{1}{r^{(2)}_{P'}}\right)\left(\frac{1}{r^{(1)}_{P''}} - \frac{1}{r^{(2)}_{P''}}\right) \tag{2.13}$$

with $r^{(1)}$ and $r^{(2)}$ as the principal radii of curvature of the respective particles, and ϕ as the angle between the principal axes of the two surfaces. Considering $r^{(1)} = r^{(2)} = r_P$ for spherical bodies, the expression readily simplifies to

$$V_{P',P''}(a) = 2\pi \frac{r_{P'} r_{P''}}{r_{P'} + r_{P''}} \int_a^\infty E_{planes}(a')\ \mathrm{d}a'\ . \tag{2.14}$$

In the following sections the interaction energies between macroscopic bodies of spherical geometry are discussed for London-van der Waals and electrostatic double layer interaction. In addition to these interactions some non-DLVO Born repulsion and solvation effects are highlighted which become important in modelling the potential interaction energy at very close particle approach and for biologically mediated aggregation, respectively.

2.2.1 London-van der Waals interaction

As mentioned in the introductory comment to this chapter, attractive forces between neutral, chemically saturated molecules, as postulated by van der Waals to explain non-ideal gas behaviour, are of electromagnetic origin. Three distinct forces contribute to the total long-range interaction between polar molecules, collectively known as van der Waals force: these are the Debye induction force between two dipoles, the Keesom orientation force between a dipole and a non-dipole and the London dispersion forces between two non-polar molecules, each of which has an interaction free energy that varies with the inverse sixth power of the separation distance[68]. In the interaction between two dissimilar molecules of which one is non-polar, the van der Waals energy is almost completely dominated by the dispersion contribution[68]. The origin of dispersion forces may be understood intuitively as follows: for a non-polar atom the time average of its dipole moment is zero, yet at any instant there exists a

finite dipole moment given by the instantaneous positions of the electron about the nuclear protons[68]. This instantaneous field generates an electric field that polarises any nearby neutral atom, inducing a dipole moment in it. The resulting interaction between the two dipoles gives rise to an instantaneous attractive force between the two atoms, and the time average of this force is finite. Unlike Coulomb forces, van der Waals forces are not generally pairwise additive. The net effect on the interaction energy is however usually small, so that the approximations made by Hamaker[51] discussed below are valid to a sufficient level of accuracy[68]. Furthermore, when two atoms are an appreciable distance apart, the propagation time of the electric field can become comparable with the period of the fluctuating dipole itself. With increasing separation, the dispersion energy between two atoms begins to decay faster than r^{-6}, giving rise to retardation effects[68]. Assuming pairwise additivity, Hamaker derived an analytical expression for the van der Waals interaction energy in the non-retarded case[51]. For spherical particles with different radii $r_{P'}$ and $r_{P''}$ it is given by Eq. (2.15):

$$\begin{aligned} V^{vdW}_{P',P''}(a) &= -\frac{A_{P',P''}}{6}\left[\frac{2r_{P'}r_{P''}}{a^2+2a\left(r_{P'}+r_{P''}\right)}+\frac{2r_{P'}r_{P''}}{a^2+2a\left(r_{P'}+r_{P''}\right)+4r_{P'}r_{P''}}\right. \\ &\quad \left.+\ln\left(\frac{a^2+2a\left(r_{P'}+r_{P''}\right)}{a^2+2a\left(r_{P'}+r_{P''}\right)+4r_{P'}r_{P''}}\right)\right] \end{aligned} \tag{2.15}$$

in which $A_{P',P''}$ represents the Hamaker constant between the two particles P' and P'' across the separating liquid medium. The van der Waals contribution to the total energy of interaction is shown for typical cases in Figures 2.3 and 2.4. For the non-retarded case, the Hamaker constant for two macroscopic phases 1 and 2 interacting across medium 3 can be gained from the Lifschitz-theory as[68]

$$\begin{aligned} A_{132} &\approx \frac{3}{4}k_BT\left(\frac{\varepsilon_{r1}-\varepsilon_{r3}}{\varepsilon_{r1}+\varepsilon_{r3}}\right)\left(\frac{\varepsilon_{r2}-\varepsilon_{r3}}{\varepsilon_{r2}+\varepsilon_{r3}}\right) \\ &\quad +\frac{3h\nu_e}{8\sqrt{2}}\frac{\left(n_1^2-n_3^2\right)\left(n_2^2-n_3^2\right)}{\left(n_1^2+n_3^2\right)^{\frac{1}{2}}\left(n_2^2+n_3^2\right)^{\frac{1}{2}}\left[\left(n_1^2+n_3^2\right)^{\frac{1}{2}}+\left(n_2^2+n_3^2\right)^{\frac{1}{2}}\right]} \end{aligned} \tag{2.16}$$

where h is the Planck constant, n represents the relative refractive index and ν_e is the so-called plasma frequency of the free electron gas. From Eq. (2.16) we can observe that the van der Waals force between identical bodies in a medium is always attractive with positive $A_{P',P''}$, while that between different bodies in a medium can be attractive or repulsive[68]. If the medium is vacuum or air, the force is always attractive. To obtain approximate values for unknown Hamaker constants in terms of known ones combining relations are frequently used, but in view of the ease with which Hamaker constants may be reliably computed using Eq. (2.16) or more rigorous numerical methods, their use is not always recommendable[68].

For the interaction of polystyrene surfaces and lipid membranes across water the Hamaker constants are known from literature as $A_{PS-H_2O-PS} \approx 1\cdot10^{-20}$ J[68] and $A_{Lipid-H_2O-Lipid} \approx 4\cdot10^{-21}$ J[54], respectively. The interaction between polystyrene and melamine-formaldehyde across water was determined under consideration of the Lifschitz theory by Eq. (2.16), yielding $A_{PS-H_2O-MF} \approx 2.2\cdot10^{-20}$ J. The calculations are based on the following parameters: the relative static dielectric permittivities were chosen as $\varepsilon_{r,PS} = 2.55$ for polystyrene[22], $\varepsilon_{r,MF} = 6.8$ for melamine-formaldehyde[132] and $\varepsilon_{r,H_2O} = 80$ for water[68]. The absorption frequency ν_e ranges between $(3-5)\cdot10^{15}\,s^{-1}$ and for polystyrene it is approximately[68] $\nu_{e,PS} \approx 2.3\cdot10^{15}\,s^{-1}$.

As refractive indices $n_{H_2O} = 1.33$ for water[68], $n_{PS} = 1.59$ for polystyrene and $n_{MF} = 1.68$ for melamine-formaldehyde as determined by the supplier were assumed. For lipid membranes Israelachvili[68] estimates $n_{lipid} = 1.45$.

2.2.2 Double layer interaction

The calculation of the interaction energy resulting from the overlap of the diffuse parts of the double layer is difficult. Since no exact analytical solutions can be obtained, numerous (sometimes numerical) approximations have been developed[135]. If we assume that the ion adsorption equilibrium is maintained upon approach of two particles, two distinct situations can be distinguished. If the surface charge is the result of potential-determining ions, the surface potential remains constant at the surface and the surface charge density adjusts accordingly. But if the surface charge is the result of ionisation, the surface charge density remains constant and the surface potential adjusts accordingly[135].

Throughout this thesis the constant potential assumption will be applied. It recognises that in the derivation of the Fuchs stability ratio (section 2.3.1), the boundary concentration of a totally absorbing sphere remains zero, which corresponds to a surface with constant potential[6]. The electrostatic interaction between different spherical particles with surrounding double layers has been characterised by Hogg, Healy, and Fuerstenau[60] (HHF theory). For constant surface potentials the interaction potential is given by

$$V^{el}_{P',P''}(a) = 4\pi\varepsilon_0\varepsilon_r \frac{r_{P'} r_{P''} \left(\left(\Psi^0_{P'}\right)^2 + \left(\Psi^0_{P''}\right)^2 \right)}{4\left(r_{P'} + r_{P''}\right)} \cdot \left[\frac{2\Psi^0_{P'}\Psi^0_{P''}}{\left(\Psi^0_{P'}\right)^2 + \left(\Psi^0_{P''}\right)^2} \ln\left(\frac{1+\exp\left(-\kappa a\right)}{1-\exp\left(-\kappa a\right)} \right) + \ln\left(1-\exp\left(-2\kappa a\right)\right) \right] \tag{2.17}$$

with $\kappa = \left(2e^2 z_i^2 N_A I_M / \left(\varepsilon_0\varepsilon_r k_B T\right)\right)^{1/2}$ as reciprocal Debye length with N_A as Avogadro's number and $I_M = \frac{1}{2}\sum_{i=1}^{N} z_i c_i$ as molar ionic strength of the electrolyte solution. In this expression, the particle surface potential Ψ^0_P is regarded equivalent to the potential at the Stern layer Ψ_{dl}. This is justified by the electrophoretic measurement technique, in which actually the potential at a shear plane is measured (section 3.2).

The energy of the electrostatic potential between two spherical particles can be attractive or repulsive. Usually suspensions of colloidal particles are stabilised by surface modifications which yield highly repulsive energies. In heteroaggregation process, however, the electrostatic force can be strongly attractive owing to particle surface potentials of opposite sign. Figure 2.3 illustrates a sample electrostatic pair interaction potential as function of separation distance.

2.2.3 Non-DLVO interactions

In classical DLVO theory, named in honour of their authors Derjagiun and Landau[23] as well as Verwey and Overbeek[151], only electrostatic and van der Waals interactions are considered. However, when two surfaces or particles approach each other closer than a few nanometres, continuum theories may break down or other non-

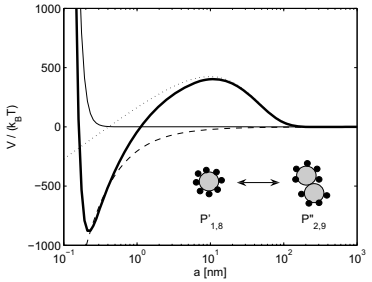

Figure 2.3: Pair interaction energy between particulate heteroaggregates as function of separation distance calculated from DLVO theory with charge-balance model (Eq. 6.9). The total energy (——) decomposes into contributions from Born $V^{Born}_{P',P''}$ (——), van der Waals $V^{vdW}_{P',P''}$ (– –) and electrostatic $V^{el}_{P',P''}$ (· · ·) energies.

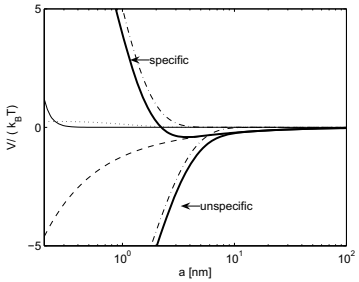

Figure 2.4: Pair interaction energy between biocolloidal particles as function of separation distance. Specific receptor-ligand attractions and unspecific repulsions both show indicated exponential behaviour (·—·—), that can be represented by conceptually similar models. The remaining interactions are encoded identically to Figure 2.3.

DLVO forces come into play. These additional forces can be monotonically repulsive, monotonically attractive or oscillatory, and they can be much stronger than either of the DLVO forces at small separations. The most important non-DLVO forces are the Born repulsion as well as solvation and structural forces and interactions of steric and fluctuation origin[67,68].

Short-range oscillatory solvation forces arise if liquid molecules are induced to order into quasi-discrete layers in highly restricted spaces between two surfaces by strong solvent-solvent or solute-solvent interactions, significantly modifying the properties of the solvent in the solvation zone compared to the bulk values. Such oscillatory forces are mainly of geometric origin[68]. In addition, surface-solvent interactions can induce positional or orientational order in the adjacent liquid and give rise to a monotonic solvation force which usually decays exponentially with separation distance[67,70]. This type of solvation force may be repulsive or attractive, and its range is generally larger than that of oscillatory forces. Solvation forces depend not only on the properties of the intervening medium but also on the chemical and physical properties of the surfaces, for instance on whether they are hydrophilic or hydrophobic.

For non-smooth, fluid-like surfaces steric and fluctuation forces can also have great impact on colloidal interaction. Here, interfaces are spatially diffuse and the forces between them depend on how their diffuse boundaries overlap. A diffuse surface is characterised by its thermally mobile surface groups, as either in inherently mobile interfaces between two fluids or in molecule chains that are fixed at the solid surface and diffusively protrude out into the solution. For both types of diffuse interfaces the interactions are subject to the complex molecular rearrangements and other effects, such as repulsive thermal fluctuations of biological membranes or protrusion forces. Artificially prepared lipid layers have been successfully used as models for studying the interactions of biological membranes[84,89,92]. By direct force measurements (section 2.2.4) it was shown that solvation forces are characterised by an exponential decay function, yielding very strong repulsive forces at close distances.

2.2.3.1 Born repulsion

At subnanoscale separation distances the repulsive overlap of electron clouds determines how close two atoms can ultimately approach each other. At subnanometre separation distances it gains dominance over all other potentials[68]. By applying Derjaguin's approximation under assumption of pairwise additivity of the atomic interaction energies, Feke et al.[33] derived a lengthy expression for the Born energy $V^{Born}_{P',P''}$ between two interacting spheres, which was implemented in the simulations discussed in this thesis. The expression depends on two parameters: the hardness factor b, i.e. the exponent of the Lennard-Jones attractive term, and the separation distance at zero potential r_σ. Throughout this thesis, these were chosen as 12 and 4 Å, respectively. Then the Born repulsion simplifies to

$$V^{Born}_{P',P''}(a) = 4\left(\frac{r_\sigma}{r_{P'}}\right)^6\left(\frac{4}{10}\right)\frac{1}{R}\left[\frac{-R^2-7\left(\frac{r_{P''}}{r_{P'}}-1\right)R-6\left[\left(\frac{r_{P''}}{r_{P'}}\right)^2-7\frac{r_{P''}}{r_{P'}}+1\right]}{\left(R-1+\frac{r_{P''}}{r_{P'}}\right)^7}\right.$$
$$+\frac{-R^2+7\left(\frac{r_{P''}}{r_{P'}}-1\right)R-6\left[\left(\frac{r_{P''}}{r_{P'}}\right)^2-7\frac{r_{P''}}{r_{P'}}+1\right]}{\left(R+1-\frac{r_{P''}}{r_{P'}}\right)^7}$$
$$+\frac{R^2+7\left(\frac{r_{P''}}{r_{P'}}+1\right)R+6\left[\left(\frac{r_{P''}}{r_{P'}}\right)^2+7\frac{r_{P''}}{r_{P'}}+1\right]}{\left(R+1+\frac{r_{P''}}{r_{P'}}\right)^7}$$
$$\left.+\frac{R^2+7\left(\frac{r_{P''}}{r_{P'}}+1\right)R+6\left[\left(\frac{r_{P''}}{r_{P'}}\right)^2+7\frac{r_{P''}}{r_{P'}}+1\right]}{\left(R-1-\frac{r_{P''}}{r_{P'}}\right)^7}\right] \quad (2.18)$$

with $R = (a + r_{P'} + r_{P''})/r_{P'}$. Figures 2.3 and 2.4 show the Born potential energy in dependence of the separation distance of the two spheres. The superposition of van der Waals and Born forces for interaction between single atoms results in a 6-12 Lennard-Jones potential.

2.2.3.2 Modelling biological interactions

As follows from the previous discussion, the four main types of forces acting between surfaces in liquid are: van der Waals, electrostatic, solvation (or hydration if the solvent is water) and steric forces[68]. For colloidal systems of rigid particles in water, the interactions are usually dominated by the first two, as suggested by DLVO theory. In contrast, forces between the highly mobile amphiphilic surfaces of fluid bilayers as in biological membranes can have all four interactions operating simultaneously, as well as other more specific types of interactions[68]. In addition, when two non-rigid structures collide, the forces between them can cause shape deformations. These will remain unconsidered in the treatment adopted in this thesis.

It has long been known that many biological interactions such as those involved in immunological ligand-receptor interactions and cellular contacts can be totally specific for a single molecule. These non-covalent interactions give rise to very strong binding[54,81]. Investigations on the design of effective drug carrier particles attempt to

harness these properties by functionalising the surfaces of drug carrier particles with specific proteins[57,105,158], for instance with antibodies[129]. Provided specific surface receptor(s) by which malign cells can be discriminated from benign ones have been identified, immunological recognition can be utilised for therapeutic purposes[38,136].

The interactions between receptor and ligand proteins including their conformational changes, which provide the basis of the lock-and-key binding mechanism, are subject to numerous detailed molecular dynamics simulations. Such a detailed approach is not considered suitable to describe aggregation dynamics on the mesoscale. Instead, approximate models characterising the specific interactions between ligands and receptors at greater distances are adopted from colloid science. The potential energies involved are subject to direct empirical methods, as discussed in section 3.1.1.

Using the surface force apparatus, interaction potentials between biological compounds were measured, that indicated an exponential decay with increasing separation distance[68]. After normalising the measured force by the radius of the SFA surfaces and converting it into a force between differently sized spheres by applying Derjaguin's approximation, the interaction potential energy $V^{sol}_{P',P''}(a)$ can be obtained from the force by integration as

$$V^{sol}_{P',P''}(a) = 2\pi k^0 \lambda \frac{r_{P'} r_{P''}}{r_{P'} + r_{P''}} \exp\left(-\frac{a}{\lambda}\right) \tag{2.19}$$

with k^0 as maximum extrapolated force at contact and λ as the decay length. An expression like this seems to be suitable for both specific receptor-ligand and unspecific interactions. For biologically unspecific aggregation, the solvation potential equals the repulsive hydration potential $V^{hydr}_{P',P''}(a)$, which originates from strongly bound water molecules on hydrophilic surfaces like cell membranes, with $k^0 = k^0_{hydr} \approx 3 - 30$ mN/m and $\lambda = \lambda_{hydr} \approx 0.6 - 1.1$ nm[68]. For ligand-receptor interactions on the other hand, Eq. (2.19) was applied with negative $k^0 = k^0_{LR}$ and $\lambda = \lambda_{LR}$. For the biotin-streptavidin interaction Leckband et al. found $k^0_{LR} = -2.5/\pi$ mN/m and $\lambda_{LR} = 1.7$ nm[81]. The interaction potentials for specific and unspecific binding are shown in Figure 2.4 as functions of separation distance a. Due to their exponential nature, the solvation potentials outmatch the ones resulting from Born repulsion and DLVO interactions on the considered scale. The total potential energy for specific and unspecific aggregation thus essentially deviate only with respect to the parameters used in the solvation interaction potential $V^{sol}_{P',P''}(a)$.

2.2.4 Direct measurement of surface forces

Much effort has been devoted to the measurement of interaction energies between macroscopic bodies at close separations, owing to their fundamental nature and their practical importance in issues such as colloidal stability. Nowadays, experimental information on surface properties can be gained by colloidal probing techniques, such as atomic force microscopy (AFM)[12,27] and surface force apparatus (SFA)[69,71,80,146]. These methods facilitate measurements of interaction forces on the molecular and single particle scale, which can be transformed into interaction energies by means of Derjaguin's approximation, as discussed in the beginning of this chapter. To date numerous studies on force measurements can be found in the literature[8,13,14,20,28,70,81,84,92,115]. In this thesis colloidal probe measurements were performed to characterise different

particle surface properties, giving rise to different aggregation dynamics. A brief description of AFM is given in section 3.1.1.

2.3 Colloidal stability

Derjagiun and Landau[23] as well as Verwey and Overbeek[151] independently developed a quantitative theory in which the stability of lyophobic sols in solutions of electrolytes is treated in terms of the energy changes upon interparticle approach. The theory considers double layer interactions as well as van der Waals energies in terms of the particle separation distance, as presented in the previous sections. By summation of all interaction potentials the total energy of interaction is obtained. Because the van der Waals force decreases with the inverse square power of the separation distance it dominates at small and large interparticle distances over the double layer energy. At very small separation distances the repulsion of overlapping electron clouds (Born repulsion) predominates when the particles come into contact, and create a deep potential minimum of the energy curve. At intermediate distances, depending on the character of the electrostatic interactions, double layer repulsion may dominate and form a maximum in the energy curve. If the potential energy maximum is large in comparison with the thermal energy $k_B T$ of the particles, the system should be stable, otherwise the system should coagulate irreversibly. Furthermore, at relatively large interparticle distances a secondary minimum can form, causing reversible flocculation.

2.3.1 Stability ratio

Based on the interaction potentials the stability of colloidal suspensions can be assessed. The foundations were laid by Fuchs in his contribution of 1934 which still receives considerable attention to date[37]. It assumes the equivalence of particle aggregation with the diffusion of particles towards an absorbing sphere placed inside an infinite medium with spatially independent particle number concentration $c\,(t=0,\vec{x}) = c_\infty$ and a superimposed force field $\vec{F}$. The radius of the totally absorbing sphere equals the collision radius $2r_P$ between two equally sized particles of radius r_P. From a mass balance of particles surrounding an adsorbing sphere we obtain the following partial differential equation

$$\frac{\partial c}{\partial t} = D_P \vec{\nabla}^2 c - \mathcal{M}_P \vec{\nabla} \cdot \left(\vec{F} c\right) \tag{2.20}$$

with D_P as constant diffusion coefficient and $\mathcal{M}_P$ as the mobility of a particle inside the medium. In anticipation of Chapter 4, the transport density $\vec{\phi}_N$ comprises a diffusive $-\vec{\nabla}\,(D_P c)$ and a convective component $\mathcal{M}_P \vec{F} c$. For a spherically symmetric system in steady-state the particle flux J in terms of centre-to-centre separation distance r follows as

$$J = D_P r^2 \frac{\mathrm{d}c}{\mathrm{d}r} - \mathcal{M}_P r^2 F(r) c \tag{2.21}$$

with the boundary conditions $c\,(t, r \to \infty) = c_\infty$ and $c\,(t, 2r_P) = 0$ at the surface of the adsorbing sphere. By integration within these boundaries and replacing the mobility

$\mathcal{M}_P$ by the Einstein expression $D_P/(k_BT)$ the following expression for the particle flux can be derived

$$J = \frac{D_P c_\infty}{\int\limits_{2r_P}^{\infty} \frac{1}{r^2} \exp\left(\frac{V_P(r)}{k_BT}\right)\, dr} \tag{2.22}$$

with the potential energy $V_P(r) = \int_r^\infty F(r')\ dr'$. The ratio of the particle flux in absence of any force field $J_0 = 2D_P c_\infty r$ to the particle flux inside a force field $V_P(r) \neq 0$, is called stability ratio W and is given by Eq. (2.23).

$$W = \frac{J_0}{J} = 2r_P \int\limits_{2r_P}^{\infty} \frac{1}{r^2} \exp\left(\frac{V_P(r)}{k_BT}\right)\, dr \tag{2.23}$$

For two differently sized particles P' and P'' and a surface-to-surface separation distance a, this expression can be recast as

$$W = (r_{P'} + r_{P''}) \int\limits_0^{\infty} \frac{B_{P',P''}(a)}{(r_{P'} + r_{P''} + a)^2} \exp\left(\frac{V_{P',P''}(a)}{k_BT}\right)\, da \tag{2.24}$$

now with $B_{P',P''}(a)$ introduced as hydrodynamic correction. The potential interaction energy is obtained by superposition of Born $V^{Born}_{P',P''}(a)$, van der Waals $V^{vdW}_{P',P''}(a)$, electrostatic $V^{el}_{P',P''}(a)$ and further non-DLVO components if applicable.

In case the potential energy of interaction does not provide a repulsive barrier against colloidal aggregation, the aggregation process is limited only by the diffusion which determines the frequency with which two aggregates collide. Upon collision, a bond is spontaneously formed. The diffusive fluxes are equal $J_0 = J$ and the stability ratio runs into its lower limit of $W = 1$. This regime is called diffusion limited cluster aggregation (DLCA) or rapid coagulation regime. Should the interaction potential present an energy barrier, aggregation is retarded by the repulsive interactions and not every collision results in the formation of a product aggregate. This regime is named reaction limited cluster aggregation (RLCA) with $W_{P',P''}$ increasing to values greater than one. Colloidal stability is attained when $W \to \infty$. This is either achieved in the absence of any potential minima (thermodynamically stable) or by a potential barrier exceeding the thermal energy of the particles (kinetically stable).

2.3.1.1 Hydrodynamic correction

The viscous resistance of the continuous medium upon very close approach of two particles reduces the coagulation rate by a factor of up to 0.4[61]. To account for this aggregation resistance due to fluid viscosity, the diffusion coefficient for an infinitely diluted system $D^{Brown}_{P',P''}$ is corrected by the hydrodynamic factor $B_{P',P''}(a)$, yielding $D_{P',P''}$ as a more accurate diffusion coefficient. The following empirical correlation for the hydrodynamic correction factor has been developed by Honig et al.[61]:

$$B_{P',P''}(a) = \frac{D^{Brown}_{P',P''}}{D_{P',P''}} \approx \frac{6\left(\frac{a}{a^*_{P',P''}}\right)^2 + 13\left(\frac{a}{a^*_{P',P''}}\right) + 2}{6\left(\frac{a}{a^*_{P',P''}}\right)^2 + 4\left(\frac{a}{a^*_{P',P''}}\right)} \tag{2.25}$$

with $a^*_{P',P''} = 2r_{P'}r_{P''}/(r_{P'} + r_{P''})$. Starting at $B_{P',P''}(a) \gg 1$ for small distances, the correction factor approaches unity at infinite separation distances.

2.4 Aggregate morphology

The theoretical aspects presented to this point give little insight into the structure of the resulting aggregates. Yet aggregation behaviour shows that the aggregate morphology is enormously influenced by these factors[64]. In very rapidly aggregating suspensions the aggregates tend to form very loose, open geometries with large amounts of entrained liquid. Slowly coagulating systems may take much longer to form aggregates but they will be much more compact[64]. In real aggregation processes, aggregates containing thousands of primary particles can arise and a detailed description of their structure is impossible. A convenient method which enables the aggregate structure to be characterised in general terms, but still conveys useful information, is found by recognising aggregates as fractal objects[29].

The morphology of aggregates can be affected by many mechanisms[11]. Classically, diffusion-limited, reaction-limited and ballistic cluster aggregation (DLCA, RLCA, BCA) have been investigated in depth[95]. In early studies, Sutherland[144] studied ballistic cluster aggregation. In ballistic cluster aggregation the primary particles move along straight lines and get instantly attached when they contact the cluster. To consider the diffusivity of the particles, the formation of aggregates has been studied by Witten and Sander[154] and Meakin[94] using stochastic formation algorithms. Their diffusion limited cluster aggregation (DLCA) was modified by Jullien and Kolb[72], who introduced a probability that the particle reaching the aggregate actually gets attached, which represents the reaction limited cluster aggregation (RLCA). One of the main findings is that clusters formed by diffusion or reaction limited cluster aggregation have a fractal nature. This self-similarity in structure allows to characterise aggregates by the fractal dimension d_f[53], which relates the total number of primary particles i in an aggregate consisting of single species particles to the radius of gyration r_P^G normalised by primary particle radius r_1 by the following equation:

$$i = k_f \left(\frac{r_P^G}{r_1} \right)^{d_f} . \tag{2.26}$$

The scaling factor k_f usually remains near unity. The fractal dimension $d_f = [1, \ldots, 3] \in \mathbb{R}$ describes the compactness of the aggregates and can be measured by determining the slope of the structure factor from static light scattering experiments[94,154], as briefly described in section 3.2. A fractal dimension of $d_f = 1$ corresponds to a linear, chain-like aggregate geometry, while the radius of gyration for $d_f = 3$ expresses the radius of a sphere with equal volume. In the DLCA regime without restructuring effects, d_f was found to attain values of approximately 1.8[88] and in RLCA $d_f \approx 2.1$[87]. For single monodisperse particle systems the number of particles i within an aggregate can be expressed by the ratio of aggregate and primary particle mass m_P/m_1[128]. By assuming that the aggregate mass only comprises the total solid mass, the mass ratio is identical to the dimensionless aggregate volume $\nu_P = V_P/V_1$. For homoaggregates, i.e. aggregates of a single species, the dimensionless volume ν_P thus equals the number of primary particles i. This approach is extended to aggregates compris-

ing more than one species, for example binary heteroaggregates $P(i,j)$ composed of i and j particles of different species. Throughout this thesis, particle species with considerable differences in their length scales are used. By neglecting any restructuring effects[95] as well as the monomer volume of the smaller particle species in the denominator due to $r_{0,1}^3 \ll r_{1,0}^3$, the dimensionless aggregate volume is obtained in a similar manner as

$$\nu_P \approx \frac{V_P}{V_{1,0}} = \frac{i\, r_{1,0}^3 + j\, r_{0,1}^3}{r_{1,0}^3} = i + j \left(\frac{r_{0,1}}{r_{1,0}}\right)^3 \tag{2.27}$$

with $r_{1,0}$ and $r_{0,1}$ as monomer radii. The radius of gyration r_P^G for a binary aggregate $P(i,j)$ then follows as

$$r_P^G = r_{1,0} \left(\frac{\nu_P}{k_f}\right)^{\frac{1}{d_f}} . \tag{2.28}$$

It is well known that real particles can hardly ever be represented by a single characteristic length. Even non-agglomerated particles can exhibit complex morphologies that can strongly affect particulate properties[11]. For instance, biological systems may strongly respond to particle shape, as was recently shown by Champion and Mitragotri[17]. This could become essential with respect to bioavailability or to certain drug targeting applications. However, for the investigations treated in this thesis the concept of fractal aggregate geometry is applied to define the radius of gyration of a representative spherical particle. It offers the advantage of a simple yet physically rooted model that reduces complex aggregate structures to a manageable amount of information. Due to the limited amount of parameters necessary, the structure can be easily solved alongside the population balance model applied to study the dynamics in aggregation processes. Furthermore, an essential influence of the particle morphology on the aggregation process beyond their increasing particle size is not expected, thus supporting the use of fractal geometries.

Chapter 3

Experimental techniques

Aggregation in colloidal systems can be probed by diverse experimental techniques with respect to a multitude of properties, which are usually used to elucidate the aggregate composition and its dynamic changes. Most of these techniques are based on optical methods that involve diffraction of either normal light or coherent laser light. Light, fluorescence, confocal laser scanning and scanning electron microscopy were used to characterise the aggregate and cell structure of random samples primarily for illustrative purposes only. Although a quantification of aggregation by these methods is in principle possible, it is rather cumbersome and difficult to realise, especially with techniques that only image one perspective of the aggregate. Tremendous efforts would be required to obtain statistically validated data that are free of external influences during measurement. With atomic force microscopy topographical images can be generated, but its use within this thesis mainly focuses on the experimental validation of theoretically predicted particle interaction potentials (section 2.2).

Further important experimental techniques are based on scattering of laser light, like dynamic and static light scattering as well as flow cytometry. These are more suitable for the measurement of aggregation dynamics inside statistically relevant particle ensembles. In this work, flow cytometry was extensively used and its convenient and powerful single-particle analysis was established to detect heteroaggregation in multi-species particle systems. Also, electrophoretic measurements of the ζ-potential contribute important information in the characterisation of the primary particles of each species as well as in detecting aggregation dynamics.

In the following, most experimental techniques are only briefly outlined, since a rigorous discussion would exceed the scope of this work and not yield new insight. Only atomic force microscopy and flow cytometry are explained in more detail since the experimental work of this thesis is mainly based on these methods.

3.1 Microscopic techniques

Qualitative insight into aggregate structure and dynamics in aggregation processes was gained by means of light, fluorescence and confocal scanning microscopy. Light and fluorescence microscopy were performed with a combined setup in an Axio Imager.A1 (Zeiss, Germany), that was equipped with a mercury arc lamp for fluorescence analyses. Both methods were also applied for a quantitative validation of the flow cytometric measurements, by manually determining the distribution of the aggregation state in a Thoma haemocytometer (Assistent, Germany). In this way a calibration was obtained that related the fluorescence intensities determined in the flow

cytometer to the absolute number of fluorescent particles. Experimental details and results are shown in Chapter 5.

Sample aggregates were also visualised by a confocal laser scanning microscope LSM-510 (Zeiss, Germany). By using different fluorescent dyes for the particle species, three dimensional images of the aggregate morphologies in a liquid environment were obtained. In order to provide images with improved resolution scanning electron microscopy (Ultra-High Resolution FE-SEM S-4800, Hitachi, Japan) was employed. Since in electron microscopy images are recorded in vacuum conditions, only solid samples can be examined. This excluded detailed analysis of biological samples and motivated a special preparation of the aggregate samples by sintering to ensure stable aggregate structure even after drying.

3.1.1 Atomic force microscopy

The interaction between two surfaces across a medium is a fundamental issue in colloid and surface science and has practical relevance when colloids are involved in technical processes. During the past decades several devices for measuring surface forces have been developed. The most prominent tools are the atomic force microscopy (AFM), dating back to the seminal work of Binnig et al.[7] of 1986, and the surface force apparatus (SFA)[71,146]. Others include the force balance, the osmotic stress method or the total internal reflectance microscope. Nowadays, AFM is one of the most important and versatile scanning microscopic tools that yields material information with an unsurpassed level of detail (ideally with subnanometre resolution) at reasonable signal-to-noise ratios. This includes structural details of biological samples such as proteins, nucleic acids, membranes, and cells in their native fluid environment[73].

The SFA contains two crossed atomically smooth mica cylinders of roughly 1 cm radius between which the interaction forces are measured. One mica cylinder is mounted to a piezoelectric translator, by which the separation distance can be adjusted. The other mica surface is mounted to a spring of known and adjustable spring constant and the separation between the two surfaces is measured with an optical technique. Knowing the position of one cylinder and the separation to the surface of the second cylinder, the deflection of the spring and the force can be calculated[14].

In contrast to SFA, in AFM the sample is scanned by a tip (probe), which is mounted to a cantilever spring. The primary modes of operation are dynamic mode and static (contact) mode. In the dynamic mode, the cantilever is excited to oscillate at or close to its resonance frequency. The oscillation amplitude, phase and resonance frequency are modified by tip-sample interaction forces. The changes in oscillation with respect to the external reference oscillation provide information about the sample's characteristics. Dynamic mode operation includes frequency or amplitude modulation. During the measurements, the cantilever can be moved in every spatial direction by means of very precise separate piezo elements. An improved control for the position regarding all three axes down to the nanometre range is guaranteed by feedback loops via a sensor with proportional and integral gains. In the x-y directions the exact lateral position can thus be maintained in closed loop mode, which considerably reduces drift during repetitive vertical scanning for force distance measurements. In z-direction the travelled piezo distance is also precisely know from the calibration.

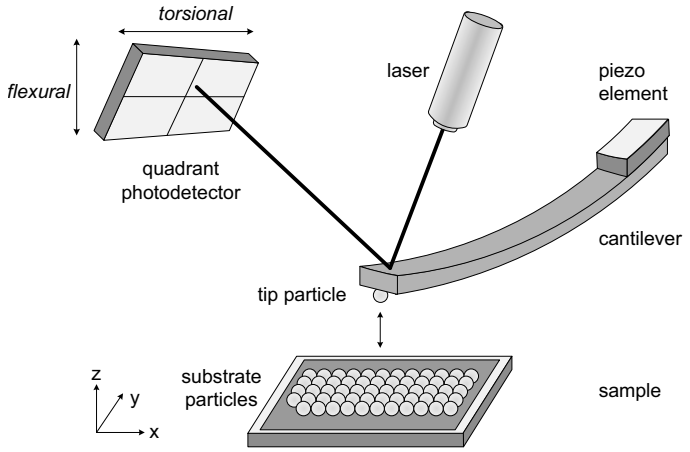

Figure 3.1: Schematic illustration of colloidal probe microscopy. Laser light is reflected from the backside of the cantilever and recorded in a quadrant detector to determine flexural and torsional forces. For force-distance measurements, the force between a particle glued to the cantilever tip and sintered substrate particles is measured in dependence of the separation distance z at constant x-y-position.

In contact mode a topographic image of the sample is obtained by plotting the deflection of the cantilever (or the height of the translation stage in constant force mode) versus the position on the sample. Image contrasts arise because the force between tip and sample is a function of their separation distance and the material properties[13]. In most applications the image contrast is obtained from the very short ranged Born repulsion, which occurs when the electron orbitals of tip and sample overlap[14]. However, further interactions between tip and sample, like van der Waals and electrostatic forces, can be investigated giving rise to techniques commonly referred to as force measurements between the cantilever probe and some substrate material. By fixing the tip at a constant lateral position on the sample and moving the cantilever in normal direction (scanning), the interaction forces can be measured as a function of separation distance of up to hundreds of nanometres (Figure 3.1).

One major step to measure surface forces independent of the cantilever tip quantitatively was the introduction of the colloidal probe technique[12,27]. In colloidal probe microscopy a spherical particle of typically 2 to 20 μm diameter is attached to the end of a tipless cantilever. Then the force between this microsphere and a substrate surface is measured. Since the radius of the microsphere can easily be determined, surface forces can be measured quantitatively for arbitrary geometries. For imaging, a microsphere is of course not suitable at the tip of the cantilever. A multitude of investigations followed to verify models for particle interactions, like DLVO interaction potentials[28,159] or the Derjaguin approximation[117].

The direct result of a force measurement is a relation between the photodetector current and the height of the piezoelectric translator $\Delta z_p = z_p - z_p^0$. To obtain a force-distance curve for hard materials with surface forces in terms of the cantilever deflection $\Delta z_c = z_c - z_c^0$, both data sets have to be converted. Essentially two parameters are necessary for this: the sensitivity and the zero distance. In atomic force

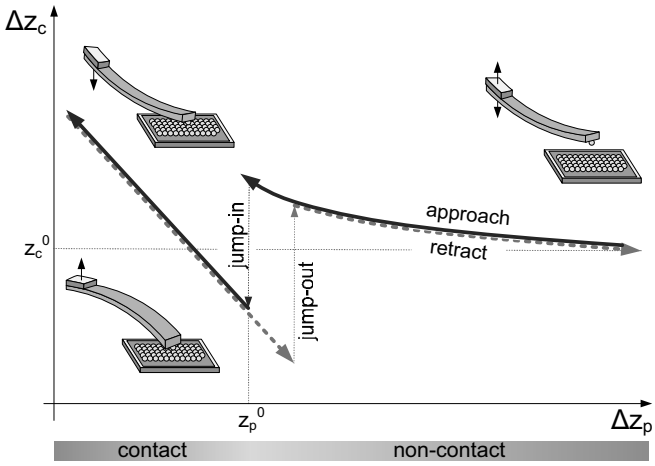

Figure 3.2: Schematic illustration of force distance curves as plot of cantilever deflection Δz_c against separation from substrate surface Δz_p. A cycle in force measurement begins at large tip-surface separation where interaction forces are negligible and the cantilever is not deflected. With decreasing separation upon piezo approach, forces begin to act. In the scheme repulsive forces were assumed, bending the cantilever upwards. Since tip and sample are not in contact, this region is often referred to as non-contact region. Once the gradient of the attractive forces exceeds the sum of spring constant and gradient of repulsive forces, the tip jumps onto the sample surface (jump-in). Decreasing the separation even further causes a deflection at the same scale as the piezo distance travelled. This linear part is called contact region. Finally, the cantilever is withdrawn to its original position. During retraction the tip often sticks to the surface due to adhesion.[13]

microscopy both parameters must be inferred from the measured curve itself and not through an independent method[14]. The curves can be divided into a contact and a non-contact part (Figure 3.2). In contact, the separation distance a between cantilever and piezo element is zero $a = \Delta z_p + \Delta z_c = 0$, so that $\Delta z_p = -\Delta z_c$. The slope in this linear part yields the sensitivity of the photodiode current with respect to the cantilever deflection Δz_c (deflection sensitivity), that can now be determined from the negative piezo distance $-\Delta z_p$. The zero deflection of the cantilever z_c^0 is found from the non-contact part of the measured curve at large distances where the surface forces are negligible[14]. The zero distance of the piezo element z_p^0 then follows from the intersection of the extrapolated linear regimes of contact and non-contact mode (Figure 3.2). The degree of extrapolation determines the error in zero distance. The weaker and shorter ranged the repulsive force is and the larger the two linear regimes of the curve are, the more accurate z_p^0 can be defined. From the cantilever deflection Δz_c, the force is obtained by the force law $F = K \cdot \Delta z_c$, where K represents the spring constant of the cantilever. The spring constant can in principle be calculated from the material properties and cantilever geometry. More details can be found in Butt et al.[14]. Close to the surface of the sample, attractive forces can be quite strong, causing the tip to snap-in to the surface at a certain point (jump-in). The jump-in into contact occurs when the gradient of attractive forces exceeds the spring constant plus the gradient of the repulsive forces[13]. During retraction the tip often sticks to the surface due to adhesion[13].

Currently AFM is evolving into a standard tool to characterise biological surfaces. It is able to image biological samples under physiological conditions at high resolution and probe molecular interactions of biomolecules[14]. In combination with the unique capability of AFM to acquire forces locally and with high sensitivity it is possible to obtain information about the interactions of single biological molecular pairs[14]. These kind of experiments are known as force spectroscopy. Two main fields of interest have emerged: molecule stretching and specific interactions between biological pairs[14]. With biofunctionalised tips, receptor-ligand binding potentials[73,155] and local receptor distributions on cellular surfaces[14,20] were mapped.

The main focus of AFM measurements within this thesis is to study surface forces between the aggregating particle species. To this end, an Agilent 5500 Scanning Probe Microscope (Agilent, USA) was used. The handling of the cantilevers under the microscope for the preparation of the colloidal probe was facilitated by a three axis water hydraulic micromanipulator (MHW-3, Narishige, Japan).

3.2 Light scattering techniques

A suspension of particles illuminated by a light beam causes some of the light to be scattered. In general, scattering by particles depends on their size, shape and refractive index, the wavelength of the incident light and the angle of observation. The scattering of light results from the electric field associated with the incident light. It induces periodic oscillations of the electron clouds in the atoms of the investigated material, which then act as secondary sources and radiate the scattered light[135]. A mathematical framework to describe light scattering is obtained from the formal solution of Maxwell's equations with the appropriate boundary conditions. For a homogeneous spherical particle the full solution was first formulated by Mie[97] in 1908 and became known as Mie theory. Some general restrictions were made[97,148]. For one, the scattered light is assumed to be of the same frequency as the incident light, excluding Raman or any quantum transitions effects. Furthermore, particles are considered as independent scatterers. Together with the first assumption we obtain that the intensities scattered by various particles can be added without regarding the phase, which is justified for most practical purposes. Early estimates fixed the distance between particles sufficiently large to ensure independent scattering at a mutual distance of three times the particle radius[148], which is met in many colloidal solutions. In 1912 Mie theory was extended to spheroidal particles by Gans[40]. Depending on size of the colloid particles, approximations of Mie theory can be adopted. For particles much smaller than the light wavelength (below about 10% of the wavelength) the scattered light is described by the Rayleigh expression for spherical and the Rayleigh-Gans-Debye expression for irregularly shaped particles[29]. For particle sizes much greater than the light wavelength, scattering can be treated by Fraunhofer diffraction as a problem of geometrical optics, where the scattering depends on wavelength and particle diameter, but not on particle properties[29]. Further detailed information on light scattering by particles can be found in the textbooks by van de Hulst[148] and Elimelech et al.[29] or a review by Sorensen[140].

A major motivation for understanding how aggregates scatter and absorb light is its importance for in situ scattering and absorption measurements of particle size, morphology and number density. Light scattering is noninvasive, remote, fast and is

usually superior to other more direct method for particle characterisation[140]. Measurements of extinction or turbidity exploit the reduction of light intensity as consequence of scattering during transmission through the suspension[29]. Next to this very simple method of deriving information on particle size or the state of aggregation in suspensions, more detailed information can be gained by measuring the angular distribution of scattered light. In static light scattering (SLS) the average of the scattered light intensities provides information over a wide range of particle sizes. Here, the intensity, polarisation and angular distribution of the light scattered from a colloidal system are subject to direct measurement by means of detecting photocells placed at different angles around the sample[135]. The particle size distribution is calculated from Mie theory and its approximations. In addition to the particle size distribution, information regarding aggregate morphology is obtained by SLS. In a double logarithmic plot of the structure factor against the scattering vector, the fractal dimension d_f, characterising the compactness of an aggregate (section 2.4), can be determined[29]. When the reciprocal value of the scattering vector exceeds the aggregate radius of gyration r_p^G or is smaller than the primary particle radius r_1, the structure factor is independent of the scattering vector. For intermediate values of the scattering vector, the slope equals $-1/d_f$. In this way, fractal dimensions characterising DLCA[88] and RLCA[87] regimes could be identified experimentally in accordance with the preceding simulation studies[94,95,154].

In dynamic light scattering (DLS), also referred to as photon correlation spectroscopy (PCS) or quasi-elastic light scattering (QELS), the diffusion coefficients of the particles inside the suspension are measured, from which the size information can be derived. Light scattered by a moving particle will experience a Doppler shift to slightly higher or lower frequency, depending on whether the particle is moving towards or away from the observer[135]. For an ensemble of particles moving at random due to Brownian motion, a Doppler frequency broadening will appear. Analysis of this effect involves autocorrelation of the scattered light intensity, measured as pulses from a photomultiplier.

The laser Doppler technique can also be used to determine the convective velocity of charged particles in a superimposed electric field. In this way charged particle surfaces can be studied. Fundamental to electrophoretic behaviour is the existence of a shear plane, which separates the fixed from the mobile parts of the electric double layer[135]. It is usually assumed that the shear plane lies outside but fairly close to the Stern plane, so that essentially all of the diffuse layer charge is mobile and the counterions in the Stern layer are fixed[29]. The electrical potential at the shear plane is referred to as the ζ-potential and it represents a measure of the particle surface charge. Due to its influence on the electrostatic interaction potential, manifested by Eq. (2.17), the ζ-potential is a very important quantity in the characterisation of colloidal suspensions. Colloidal particles are generally found to be stable if the ζ-potential exceeds a certain value and to aggregate at lower absolute values[29].

From the induced particle velocity in the electrolyte solution, the ζ-potential can be determined for conducting and non-conducting spheres by means of the approximative Henry equation[56] from electrokinetic theory. The Henry equation is based on the Debye-Hückel approximation for constant $\varepsilon_0\varepsilon_r$ and η and assumes the superposition of applied electric field and electric double layer. However, more detailed models were investigated, which couple the velocity field in the electrolyte to the distribution of ions and the electrostatic potential around a colloidal particle[100]. The use

of laser Doppler velocimetry is restricted to rather small particles (for size measurements $r_P < 1$ μm, for ζ-potential measurements $r_P < 5$ μm). Therefore, its use in aggregation studies is limited.

3.2.1 Flow cytometry

Flow cytometry took its origin in biomedical research. The need to characterise human blood and to discriminate between the individual cell types promoted the development of modern flow systems. Major advances in designing flow chambers for fluorescence analysis were achieved in the late 1960's, yielding flow chamber based microscopes to detect fluorescence intensity histogrammes[25] and first fluorescence detection cytometers[149]. But it was not until the 1980's that self-contained benchtop devices made flow cytometry accessible to a broader user group. With the recent advances in detecting and discriminating biological components by fluorescent labelling, flow cytometry has become a standard tool in biological and biomedical research.

In flow cytometry, particles are passed through a capillary of about 50 to 250 μm diameter by a stream of sheath fluid from a pressurised reservoir. Sheath fluids are usually composed of phosphate-buffered saline solutions and provide the supporting vehicle for directing the cells through a light source for scattering[44]. The sample suspension is injected into the centre of the sheath stream in a flow chamber (coaxial flow) and is hydrodynamically focused for its passage through a laser beam, usually an Argon laser with $\lambda_{Ar} = 488$ nm (Figure 3.3)[109,110]. The laser beam is itself optically modified from 1-2 mm in diameter to an elliptical spot of about 20 μm by 60 μm in size[44]. The ellipsoid geometry represents a compromise between lateral path tolerance inside the capillary and adequate temporal resolution. Particles passing through the laser beam generate scattering signals, that can be analysed with respect to several signals simultaneously. The scattered light is detected by photomultipliers at two principal angles, the forward scattering (FS) at a near-zero angle and the side scattering (SS) perpendicular to the incident light, which can only be reached by diffracted or emitted light. This provides information about the physical characteristics of the detected particle or cell, regarding size and granularity; granularity is related to the size, shape, surface texture and internal structure of the detected particle[44]. The side scattered light is passed through an optical bench for further analysis of sample fluorescence. Fluorescence originates from electrons that fall back from an excited state to their ground state orbitals. Due to dissipation effects, the emitted light always is of longer wavelength that the absorbed light (Stokes shift). In a flow cytometer the excitation is caused by the laser light and common detection wavelengths include $\lambda = 525, 575, 620, 675$ nm. All detected light signals are converted to electrical impulses by photodetectors. Since this requires input by the user, some extent of arbitrariness is introduced[44]. However, the important benefit of not fixing the photomultiplier settings is the influence over the measurement sensitivity. The electric current as response to detected light can be modified in two ways, either by changing the voltage applied to a photomultiplier or the signal amplification. The control over signal amplification offers variations in gain as well as in linear or logarithmic amplification. All data over a particle ensemble produced during a measurement is recorded electronically in a standardised file format called flow cytometry standard (FCS)[21]. More information on the complex hydrodynamic and optical experimental

set-up and applications of flow cytometry can be found in the textbooks of Shapiro[134] and Givan[44].

Optimal operating conditions imply restrictions with respect to the size and concentration of the colloidal particles in suspension. Particles larger than the hydrodynamic instrumentation will clog the system. Most commercial systems permit diameters of 50-100 μm[44]. In order to discriminate the particles from experimental noise, particle size also faces a lower limit, which lies somewhere below 1 μm[44]. In this thesis fluorescent particles of 350 nm could be detected well, albeit with elevated signal dispersion. However, if in mixture with larger particles, the stronger signals dominated and the small particles were hardly visible (section 5.2.2.1). In order to facilitate reasonably quick measurements, particle or cell concentrations of approximately $1 \cdot 10^6$ particles/ml are suggested at detection rates of 1000-2500 particles/s, depending on the device.

The signals of all photomultipliers (channels, parameters) are recorded for each detected event. They can be retrieved from the FCS files for post-processing and experimental analysis. By plotting the signal intensities of a single detector for all events of a measurement we obtain a number distribution histogramme (Figure 3.3), which can be characterised by standard statistical methods. Correlations between multiple signals are also frequently studied, giving rise to dot plot representations. However, such analyses are usually restricted to two-dimensional plots, like the one shown in Figure 3.4, due to the restrictions set by visualising plots of higher dimensionality. Thus from x detected signals, $(x-1)!$ dual-parameter plots can be generated, from which in most cases only a few contain relevant information. To analyse the data, cer-

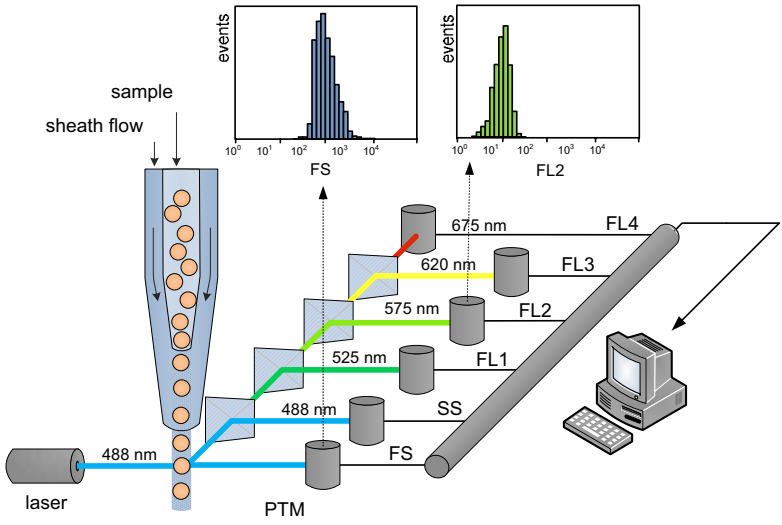

Figure 3.3: Schematic illustration of a flow cytometer. Sample particles are passed single-file through a laser beam. The scattering signal is processed by an optical bench and transformed into an electrical signal by photomultipliers (PTM). The data for each particle of an ensemble is collected electronically so that by further analysis histogrammes of intensity distributions are obtained.

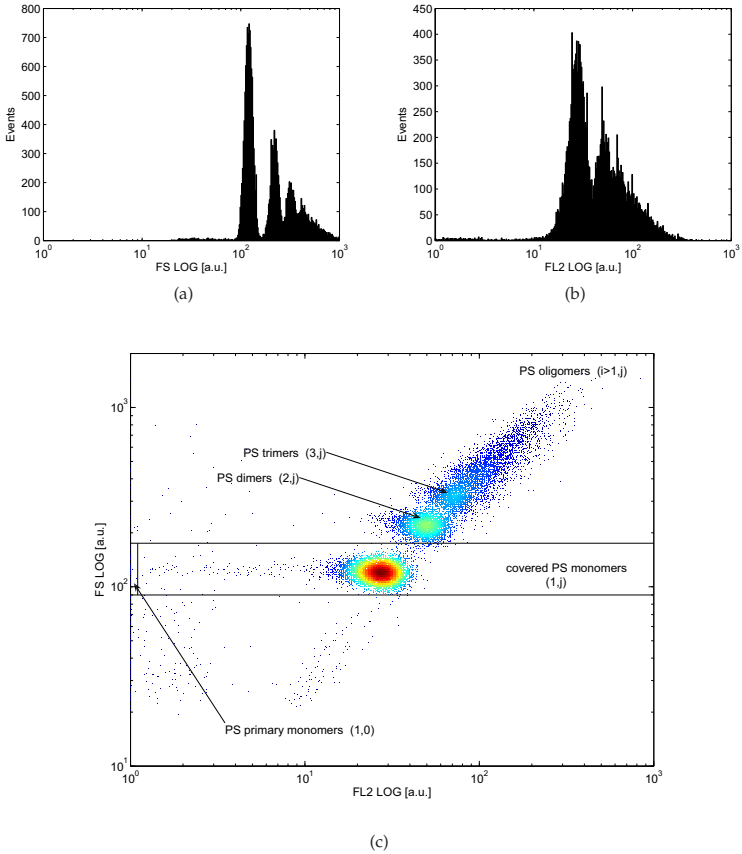

Figure 3.4: A two-dimensional dot plot (c) combines the information of two independent histogrammes (a) and (b). Colour coding represents the number density. Gates indicate user specified regions in the histogrammes or the dot plot.

tain subsets within the analysed event population are usually defined. These subsets are found by observing some specifying characteristic regarding one or more signals. As shown in Figure 3.4, subsets can be established as regions in histogrammes or dot plots. Because an automated definition of regions is not possible, finding the appropriate regions represents one of the most subjective aspects of flow cytometry. For some evaluations it is necessary to focus only on those events within a certain region or a boolean combination of regions. This process is called gating and the considered region(s) are referred to as gates[44].

Since fluorescence represents an average over many fluorophore molecules and excitation-emission cycles, emitted light is not ideally monochromatic but distributed with respect to the wavelength. The distribution is characteristic for the specific kind of fluorescent molecule and causes spectral overlap or cross-over. In multicolour flow cytometry spectral overlap may cause artifacts of the signal intensities, which have to

be compensated for electronically. Compensation networks measure the intensity of the signal on one photodetector and subtract a certain percentage of that signal from the signal on another photodetector[44]. The percentages are routinely determined empirically prior to the measurements.

For the analyses conducted in this thesis, an Epics XL flow cytometer (Beckman-Coulter, USA) was used. The device is equipped with an argon laser that yields an incident wavelength of $\lambda_{Ar} = 488$ nm and detectors for $\lambda = 525, 575, 620, 675$ nm.

3.2.2 Detecting heteroaggregation by light scattering

In this thesis static light scattering with a Master Sizer 2000 (Malvern Instruments, UK) and dynamics light scattering with a Zetasizer Nano ZS (Malvern Instruments, UK) were used to characterise the sizes of primary particles and cells. Additionally, the DLS device was used to determine the ζ-potentials of the primary particles and of the suspension during aggregation. To reduce possible effects of interference by particle fluorescence, the Zetasizer was equipped with a narrow band filter permeable only for the He-Ne laser at $\lambda_{HeNe} = 633$ nm. Structural analyses regarding the fractal dimension d_f for DLCA and RLCA regimes were not performed, instead the values were adopted from literature as discussed in section 2.4. Although it is common to determine also the size evolution during aggregation in form of cumulative mass distributions with SLS or DLS[90], they do not provide an optimal resolution of cluster composition in multi-species systems.

A technique enabling a higher resolution is multiangle simultaneous static and dynamic light scattering. It essentially represents a combination of SLS and DLS by which estimates of absolute heteroaggregation rates can be found[39,86]. However, since this technique probes a large particle ensemble - like SLS and DLS generally do - only rates are obtained that represent averages over the cluster composition. An alternative method yielding complementary information is single cluster light scattering (SCLS), which is also referred to as single particle optical sizing (SPOS)[35,109,110]. Much like a one parameter flow cytometer, clusters in SCLS can be differentiated according to their size (FS signal) by means of an automated single particle analysis. Although this allows the detection of monomeric and several multimeric aggregation states (under ideal conditions up to heptamers[110]), simultaneous homo- and heteroaggregation processes cannot be distinguished. It is only by using additional measurement information in a single particle analysis, that complex heteroaggregation processes can be determined in full. In a flow cytometer the additional information is provided by the measurement of aggregate fluorescence. This requires fluorescent labelling of all particle species, each species with a different fluorophore, so that an optimal discrimination is possible. Depending on the size of the primary particles, one species may be fully characterised by the FS signal, reducing the amount of fluorescent colours by one.

Flow cytometry was extensively used within this thesis to quantify the dynamic evolution of cluster composition in multi-species mixtures. Although the use of similar flow systems for the detection of aggregation processes was already investigated previously[9,10,109,110], it has not been applied in combination with fluorescence signals to investigate complex heteroaggregation phenomena in particle systems. All measurements were conducted by an Epics XL (Beckman-Coulter, USA) and aggregation rates were determined by comparison to simulation data.

Chapter 4

Population balance modelling of colloidal aggregation

Most discussions of aggregation processes take their origin in the classic work of von Smoluchowski[152], who laid the foundations for their kinetic description and the use of population balances in this field. In his work, a dispersion of initially identical particles (primary particles) was considered, which, after a period of aggregation, contained aggregates of various sizes and different concentrations. Aggregate size implies the number of primary particles comprising the aggregate. With the help of conservation equations which balance the amount of aggregates for each property state, von Smoluchowski first predicted the distribution of aggregate size and its dynamic evolution. A fundamental assumption still common today is that aggregation is a second-order rate process, in which the rate of collision is proportional to the product of concentrations of two colliding species[29]. Three-body collisions only become important at very high particle concentrations[29], and will therefore be ignored throughout this thesis. Although there are some theoretical difficulties, it is further assumed that the collision frequency is independent of colloid interactions and depends only on the particle transport. This can be justified on the basis of the short-range nature of interparticle forces. They operate over a range which is less than the particle size, so that particles are nearly in contact before these forces come into play[29]. The decoupling of transport and attachment steps greatly simplifies the analysis of aggregation kinetics. Nowadays, the use of population balance models to investigate aggregation processes is well established in academia and increasingly in industry. The basic concepts and some general implications on their use also within this thesis will be established in the following sections of this chapter.

4.1 General formulation of population balance equations

Generally, a disperse phase can be characterised quantitatively by a set of selected properties. Following the seminal works of Hulburt and Katz[63], these properties are categorised into internal $\vec{e}$ and external $\vec{x}$ coordinates summarised in

$$\vec{\mathcal{P}} = \begin{pmatrix} \vec{e} \\ \vec{x} \end{pmatrix} . \tag{4.1}$$

The external coordinates $\vec{x}$ describe the geometrical position of the disperse entity in space and are therefore limited to three dimensions. The internal coordinates $\vec{e}$ are usually referred to as property coordinates and represent particle properties which are considered important for the state of the disperse phase. For instance in particle heteroaggregation, this can be the number of constituent particles of each species. In theory, their number remains unlimited, in practice their number is constrained by the computational feasibility. One or more of either the internal and/or external coordinates may be discrete while the others may be continuous. There are several ways in which the internal coordinates may be discrete[116]. A simple example is that of particle size in a population of particles, initially all of uniform size, undergoing pure aggregation. In this case the particle size can only vary as integral multiples of the initial size. External coordinates are discrete if particles can occupy only discrete sites in a lattice. All property coordinates constitute a property state space $\mathcal{P}$[42,116], also referred to as property phase space[63] or simply as property space. At every time each entity can be represented as point in this phase space, exactly defining the momentary state of the entity regarding its position and properties. In this thesis the focus lies on discrete property coordinates, representing absolute particle numbers inside an aggregate. External coordinates are neglected due to the assumption of homogeneous mixing (section 4.4).

Fundamental to the formulation of a population balance equation is the assumption that there exists a number density of particles at every point in the particle state space[116]. The number density f describes the number of entities inside a certain state space volume

$$f = f\left(\vec{e}, \vec{x}, t\right) \tag{4.2}$$

and thus depends on the property coordinates $\vec{e}$, the spatial coordinates $\vec{x}$ and time t. The number of particles in any region of the state space is obtained by integrating the number density over the desired region:

$$N\left(t\right) = \int\limits_{V_x \subseteq \Omega_x} \int\limits_{V_e \subseteq \Omega_e} f\left(\vec{e}, \vec{x}, t\right)\, dV_e dV_x \,. \tag{4.3}$$

where Ω_x represents the domain of external coordinates and Ω_e that of the internal coordinates. In a discrete region the integration amounts to simply summing over the discrete states in the region. The population balance equation is formulated in terms of the number density f and basically represents a number balance on particles of a particular state[116]. The equation is often coupled with conservation equations for properties of the continuous (environmental) phase surrounding the particles. The number density function, along with the environmental phase variables, completely determines the evolution of all properties of the dispersed phase system[116].

A population balance accounts for various ways in which particles of a specific state can either form in or disappear from the system. Processes which cause the smooth variation of particle states with time must contribute to the rates of formation and disappearance of specific particle types. Such processes may be seen as convective processes since they result from convective motion in particle state space[116]. They cause no change in the total number of particles in the system except when particles depart from the boundaries of the system. Other ways in which the number of particles of a particular type can change is by processes that create new particles

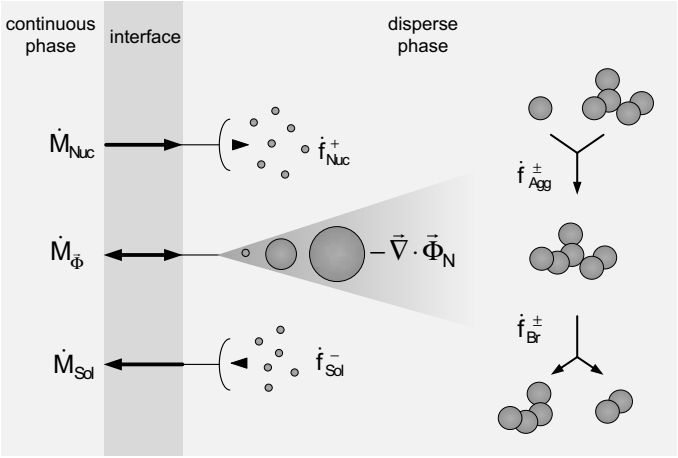

Figure 4.1: Schematic illustration of general population balance phenomena in a disperse system.

(birth processes) and destroy existing particles (death processes). The processes to which the disperse phase is subject to are schematically illustrated in Figure 4.1.

Birth of new particles can occur due to nucleation, aggregation or breakage processes. Breakage and aggregation processes also contribute to death processes, as does dissolution, since a particle that aggregates with another particle or breaks into other smaller particles no longer exists as such after the event. For a detailed elegant derivation of a the population balance equation the reader is referred to the textbook of Ramkrishna[116] and the PhD thesis of Gerstlauer[42]. Following their concept, we begin with the integral balance equation for the absolute number of particles $N\,(t)$ in an arbitrary control volume of state space $V_e \cup V_x$ according to the Reynolds transport theorem

$$\frac{dN}{dt} = \Gamma_N + \Sigma_N \tag{4.4}$$

with Γ_N as transport term across the boundaries of the control volume $V_e \cup V_x$ and Σ_N as source/sink term[42]. Considering Eq. (4.3) in combination with the volume integral for Σ_N, which introduces the source density σ_N, and a surface integral for Γ_N we obtain

$$\begin{aligned}
\frac{d}{dt}\int_{V_x}\int_{V_e} f\,(\vec{e},\vec{x},t)\,dV_e dV_x = & \quad -\int_{S_r}\int_{S_e} \vec{n}\cdot\vec{\phi}_N\,(\vec{e},\vec{x},t)\,dS_e dS_r + \int_{V_x}\int_{V_e}\sigma_N\,dV_e dV_x \\
\frac{d}{dt}\int_{V_x}\int_{V_e} f\,(\vec{e},\vec{x},t)\,dV_e dV_x = & \quad -\int_{V_x}\int_{V_e} \vec{\nabla}\cdot\vec{\phi}_N\,(\vec{e},\vec{x},t)\,dV_e dV_x + \int_{V_x}\int_{V_e}\sigma_N\,dV_e dV_x\,. \qquad (4.5)
\end{aligned}$$

The second equation follows from application of the Gaußtheorem to the transport term, obtaining the transport density $\vec{\nabla}\cdot\vec{\phi}_N\,(\vec{e},\vec{x},t)$ across the boundaries of the con-

trol volume. If we assume a control volume of fixed size, we can derive the following equation

$$\int_{V_x}\int_{V_e}\left(\frac{\partial f\left(\vec{e},\vec{x},t\right)}{\partial t}+\vec{\nabla}\cdot\vec{\phi}_N\left(\vec{e},\vec{x},t\right)-\sigma_N\left(\vec{e},\vec{x},t\right)\right)dV_e dV_x=0 \tag{4.6}$$

from which, since the choice of the control volume is arbitrary, the population balance equation follows in local formulation as

$$\frac{\partial f\left(\vec{e},\vec{x},t\right)}{\partial t}=-\vec{\nabla}_x\cdot\vec{\phi}_{N,x}\left(\vec{e},\vec{x},t\right)-\vec{\nabla}_e\cdot\vec{\phi}_{N,e}\left(\vec{e},\vec{x},t\right)+\sigma_N\left(\vec{e},\vec{x},t\right)\ . \tag{4.7}$$

In this equation the transport density was subdivided into its contributions from property associated $\vec{\phi}_{N,e}$ and from spatial $\vec{\phi}_{N,x}$ transport[42]. Both fluxes can be expressed by the sum of convective $\vec{w}\cdot f\left(\vec{e},\vec{x},t\right)$ and diffusive $\vec{\phi}_N^D$ contributions in analogy to balance equations for non-disperse systems[42]

$$\vec{\phi}_{N,x} = \vec{w}_x\cdot f\left(\vec{e},\vec{x},t\right)+\vec{\phi}_{N,x}^D \tag{4.8}$$

$$\vec{\phi}_{N,e} = \vec{w}_e\cdot f\left(\vec{e},\vec{x},t\right)+\vec{\phi}_{N,e}^D \tag{4.9}$$

where $\vec{w}$ represents the average convective velocity.

4.1.1 Source and sink terms in population balances

The source or sink term $\sigma_N\left(\vec{e},\vec{x},t\right)$ comprises all birth and death phenomena related to variations in the distribution of the number density function $f\left(\vec{e},\vec{x},t\right)$ within the control volume (Figure 4.1). These include nucleation $\dot{f}_{Nuc}^{+}$, solvation $\dot{f}_{Sol}^{-}$ as well as aggregation $\dot{f}_{Agg}^{\pm}$ and breakage $\dot{f}_{Br}^{\pm}$ phenomena

$$\sigma_N=\dot{f}_{Nuc}^{+}+\dot{f}_{Sol}^{-}+\dot{f}_{Agg}^{\pm}+\dot{f}_{Br}^{\pm}\ . \tag{4.10}$$

While nucleation and dissolution represent a particle source and a particle sink, respectively, aggregation and breakage each include a source and a sink term. In this context nucleation describes the formation of new particles, like the formation of new seed crystals observed in crystallisation processes. Usually nucleation is determined by means of a nucleation rate $\omega_{Nuc}\left(\vec{e},\vec{y}\left(\vec{x},t\right)\right)$ in dependence of the state of the continuous phase $\vec{y}$, such that[42]

$$\dot{f}_{Nuc}^{+}\left(\vec{e},\vec{x},\vec{y}\right)=\omega_{Nuc}\left(\vec{e},\vec{y}\left(\vec{x},t\right)\right)\cdot f_{Nuc}\left(\vec{e},\vec{x}\right)\ . \tag{4.11}$$

The distribution of the formed particles is captured by a normalised density function $f_{Nuc}\left(\vec{e},\vec{x}\right)$, with an integral value of unity since it represents a distribution probability[42]. If particles are lost in the control volume, for instance by dissolution in the continuous medium, their number is balanced by $\dot{f}_{Sol}^{-}$. The mathematical description is similar to that of nucleation processes with a dissolution rate $\omega_{Sol}\left(\vec{e},\vec{y}\left(\vec{x},t\right)\right)$ in[42]

$$\dot{f}_{Sol}^{-}\left(\vec{e},\vec{x},\vec{y}\right)=-\omega_{Sol}\left(\vec{e},\vec{y}\left(\vec{x},t\right)\right)\cdot f\left(\vec{e},\vec{x},t\right) \tag{4.12}$$

and is directly proportional to the number distribution of particles within the control volume $f\left(\vec{e},\vec{x},t\right)$. Because this term represents a particle sink, the sign is negative. For

both types of events, the fluxes between the continuous environment and the disperse phase have to be considered in order to conserve mass or energy, as illustrated in Figure 4.1.

In contrast, aggregation and breakage phenomena are processes which are confined to the disperse phase and do not have to be balanced with the continuous phase. Therefore they each feature a source and a sink term, to account for disappearing educt particles and appearing product particles. Aggregation includes phenomena like coagulation or coalescence, while breakage describes attrition effects of the disperse solid or liquid entities. It is common to model aggregation as a process where a number of educt particles form a new single product particle upon collision. As mentioned in the introductory part of this chapter we now apply the assumption that the probability of three or more particles aggregating in a single event is negligible compared to events limited to binary interactions[29,42].

For a mathematical description of aggregation we may balance the source and sink terms of an arbitrary particle $P(\vec{e},\vec{x})$ within the confined volume. For the source term we express the formation rate of a product particle $P(\vec{e},\vec{x})$ by any two educt particles $P'(\vec{e}',\vec{x})$ and $P''(\vec{e}'',\vec{x})$ (Figure 4.2) as $\omega^{+}_{Agg}(\vec{e}',\vec{e}'',\vec{y}(\vec{x},t))$, in which all positions are approximated by those of the product particle $\vec{x}' \approx \vec{x}'' \approx \vec{x}$. The aggregation rate must be symmetrical with respect to the choice of educt particles, so that $\omega^{+}_{Agg}(\vec{e}',\vec{e}'',\vec{y}(\vec{x},t)) = \omega^{+}_{Agg}(\vec{e}'',\vec{e}',\vec{y}(\vec{x},t))$. For the death term of particle $P(\vec{e},\vec{x})$ a similar rate is defined $\omega^{-}_{Agg}(\vec{e},\vec{e}',\vec{y}(\vec{x},t))$, in which the particle $P'(\vec{e}',\vec{x})$ represents any other particle which can aggregate with $P(\vec{e},\vec{x})$. The source and sink terms for aggregation processes are then given by the following expression[42,128]

$$\begin{aligned} \dot{f}^{\pm}_{Agg}(\vec{e},\vec{x},\vec{y}) &= \frac{1}{2}\int_{V_e^*} \omega^{+}_{Agg}\left(\vec{e}',\vec{e}'',\vec{y}(\vec{x},t)\right) f\left(\vec{e}',\vec{x},t\right) f\left(\vec{e}'',\vec{x},t\right)\, dV_e^* \\ &\quad - f(\vec{e},\vec{x},t)\int_{V_e} \omega^{-}_{Agg}\left(\vec{e},\vec{e}',\vec{y}(\vec{x},t)\right) f\left(\vec{e}',\vec{x},t\right)\, dV_e \end{aligned} \tag{4.13}$$

where the integration for the source term is carried out only over a region V_e^* of smaller aggregates within the property space, while in the sink term the particles $P'(\vec{e}',\vec{x})$ may belong to the whole property space. The prefactor to the source term of $1/2$ corrects double counting effects during integration over V_e^* for symmetric systems.

In breakage processes a single educt particle $P(\vec{e},\vec{x})$ may decompose into several differently sized product particles (Figure 4.2). The breakage rate of particle $P(\vec{e},\vec{x})$ depends on the particle properties as well as on the environmental conditions at its spatial position $\vec{x}$ in state space. It is given by $\omega_{Br}(\vec{e},\vec{y}(\vec{x},t))$. The number of formed product particles depends on the educt particle $P(\vec{e},\vec{x})$ as well as the ambient conditions and may be expressed by a function $v(\vec{e},\vec{y}(\vec{x},t))$. The distribution of the formed product particles throughout the property space is represented by a dimensionless probability density function $f_F(\vec{e},\vec{e}',\vec{y}(\vec{x},t))$ which is normalised to unity upon integration over V_e. The source for product particle $P(\vec{e},\vec{x})$ following breakage of a larger aggregate $P'(\vec{e}',\vec{x})$ is obtained by means of an integration weighted over all possible sinks. The integration is performed over the subspace V_e^* that comprises all bigger

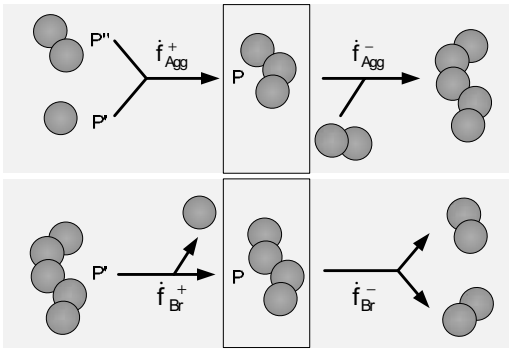

Figure 4.2: Schematic illustration of sources and sinks in aggregation and breakage of particulate entity P.

aggregates which can form the product particle by breaking apart. Considering this, the contribution of breakage events to σ_N is given by[42]

$$\dot{f}^{\pm}_{Br}\left(\vec{e},\vec{x},\vec{y}\right) = \int\limits_{V_e^*} v\left(\vec{e}',\vec{y}\left(\vec{x},t\right)\right) f_F\left(\vec{e},\vec{e}',\vec{y}\left(\vec{x},t\right)\right) \omega^{+}_{Br}\left(\vec{e}',\vec{y}\left(\vec{x},t\right)\right) f\left(\vec{e}',\vec{x},t\right)\, dV_e^* - \omega^{-}_{Br}\left(\vec{e},\vec{y}\left(\vec{x},t\right)\right) f\left(\vec{e},\vec{x},t\right) \,. \tag{4.14}$$

In addition to the normalising condition for f_F, mass conservation yields an additional condition[42]

$$v\left(\vec{e}',\vec{y}\left(\vec{x},t\right)\right) \int\limits_{V_e} m\left(\vec{e}\right) f_F\left(\vec{e},\vec{e}',\vec{y}\left(\vec{x},t\right)\right)\, dV_e = m\left(\vec{e}'\right) \tag{4.15}$$

with $m\left(\vec{e}'\right)$ as mass of the educt particle $P'\left(\vec{e}',\vec{x}\right)$.

As just shown, the population balance approach uses particle density distributions for problem formulation and, under consideration of initial, boundary and conservation conditions, might yield complex partial-integro-differential-algebraic equation systems. These are rarely accessible by analytical solutions. In order to facilitate a numerical solution, in most disperse systems the system size has to be constrained to only a handful or less property coordinates. And even for these few coordinates the total size of the property space $\mathcal{P}$ might have to be reduced further. This implies that only the most important system characteristics can be mapped and reduction methods are necessary for a quick numerical calculation. A huge number of different numerical methods has been developed over the previous decades, many of them even exhibiting different variants. A brief overview on the main classes of solution techniques is given in the following section.

4.2 Methods for numerical solution

With increasing system size population balance models tend to yield large, highly linked systems of differential equations. Excluding analytical and stochastic techniques, the solution of population balance equations depends on numerical approaches. However, quick numerical solutions are often impeded by the system complexity, which motivates model reduction strategies. From literature several methods to reduce the complexity and especially the system size are known beyond limiting the number of property coordinates. These basically all aim for a suitable discretisation, either of the population balance equation itself or of its solution[11]. By means of discretisation, population balance equations can be transferred into a set of discrete ODE's that can be numerically solved by a computer. Usually most model reduction methods are accompanied with a certain loss of system information, so that optimal numerical conditions are only found by a trade-off between computational cost and solution detail. A comprehensive overview of numerical techniques for solving population balance equations was recently provided by Briesen[11].

Common methods to approximate the population balance equation without any assumptions on the solution include finite difference and finite volume methods as well as discretised formulations of the original equation. Here, the primary handle on the computational cost is represented by the discretisation length scale of the grid on which the equation is solved. A very fine grid results in a high number of differential equations, yielding very detailed numerical solutions, while coarse grids reduce the number of equations but only achieve approximated information on the omitted grid points. Discretised expressions for continuously formulated population balance equations can be achieved by approximating the size spectrum of the state space with a set of size classes or sections[150]. The approximation is achieved by lumping an interval on state space or several discrete states into a single representative coordinate, referred to as nodes or pivots, which for instance represent the size of an aggregate in a particular domain[11]. Mechanisms, like nucleation, growth, aggregation and breakage are formulated for these nodes. In essence this represents a finite volume method, since the sets or sections are based on the integration of the population balance over a certain size domain. In the literature these approaches are often referred to as sectional methods or methods of classes, without explicitly drawing the connection to finite volume methods. By introducing correction factors, it is assured that the physically desired conservation of volume or mass and number is guaranteed[62]. Kumar and Ramkrishna[77] have developed such a fixed pivot approach that can adopt arbitrary grids and allows the conservation of two arbitrarily chosen moments of the distribution. Since this method assumes that the population of particles is distributed on grid points, only particles with masses $m_1, m_2, \ldots, m_{max}$ exist. If, due to a breakage or aggregation event, a particle is formed with mass m between m_i and m_{i+1}, such a particle is split by assigning fractions $a(m)$ and $b(m)$ to the populations at m_i and m_{i+1}, respectively, in such a way as to ensure conservation of the two chosen moments[150]. The internal distribution is lost by this approach but the solvable systems size is considerably expanded. Regarding the internal distribution within a section, we can distinguish between zero-order and higher-order methods[150]. In zero-order methods, all particles belonging to a section are supposed to be of the same size and thus the distribution is approximated by a histogramme. In contrast, higher order methods approximate the size distribution within each section with a specified functional form, usually a low order polynomial, through cubic splines or orthogonal

collocation. Of course higher order methods are more accurate, but they may suffer from stability problems or dispersion effects when dealing with very narrow initial distributions[150]. For systems which can originally be defined in a discrete manner, this method can also prove relevant in order to reduce system size by defining the population balance equation on a coarser grid of state space.

Fundamentally different strategies to solve partial differential equations are provided by the concept of weighted residuals. For the solution of population balance equations the method of weighted residuals has been first employed by Singh and Ramkrishna[138]. In contrast to the techniques presented above, these methods do not begin with the equation to be solved, but instead a trial solution is formulated which comprises a linear combination of a set of basis functions[11]. The linear coefficients of this expansion need to be determined to obtain an approximate solution. To specify a particular method, basis and test functions need to be chosen which determine the classification of the method. A major classification is with respect to the character of the basis functions allowing the distinction of local (finite element methods), global and hierarchical basis functions. For more information, the reader is again referred to the works of Ramkrishna[116] or Briesen[11].

A special branch of weighted residuals with global basis functions are moment methods. Moment methods have been suggested along with the first formulation of population balance equations by Hulburt and Katz[63] and can be viewed from different angles, which prevents the strict classification as a method of weighted residuals[11]. In rare cases the integration of the population balance equation weighted by global monomials of the particle size can be performed quasi-analytically. Then no assumptions on the size distribution are necessary and the method of moments is a transformation technique rather than a method of weighted residuals. However, in most cases the integration of the population balance equation weighted by several monomials leads to an unclosed system of equations and/or introduces fractional moments. To close the system of equations additional assumptions on the shape of the distribution can be made or interpolation techniques need to be employed. Alternatively, the closure problem can be solved by the quadrature method of moments[93] enabling a very efficient approximate solution of population balance equations. The comparatively low computational costs of this approach becomes especially important when dealing with multivariate population balance equations[124,125,156].

4.3 Other simulation approaches

Apart from deterministic population balance equations, aggregation processes can be simulated by other methods. The most prominent are Monte Carlo[108,114] and Brownian dynamics simulations[16,75]. Both use discrete representations of reasonably large sets of individual particles (ensemble) to approximate the behaviour of the generally unaccessible huge number of actually present particles. In Monte Carlo methods the behaviour of a discrete particle set is then directly rendered by stochastic events followed by ensemble averaging. Brownian dynamics approaches essentially represent an approximation of deterministic molecular dynamics simulations. The approximation concerns the extremely large differences in time scales and particle motions. In colloidal systems interactions of the particles with molecules of the environmental phase is usually replaced by stochastic effects.

The Monte Carlo method[74,96,141] aims at generating a trajectory in phase space by sampling from a given ensemble so that the ensemble average can be evaluated[29]. Although there is no single Monte Carlo method all approaches tend to follow a particular pattern of defining a domain of possible inputs, generating random inputs from the domain using certain specified probability distributions, then performing a deterministic computation using the inputs and finally combining the results of the individual runs into an overall result. Monte Carlo methods are often chosen because of three principal advantages: simplicity of implementation, capability of dealing with high-dimensional problems and ease of representing complex behaviour[11]. On the other hand Monte Carlo methods are often computationally expensive. As shown in the previous section, the dimensional limitations of deterministic population balance modelling are a major obstacle for mechanistic modelling of particulate processes. Hence, the use of Monte Carlo methods seems to be a logical consequence. They were already successfully applied to evaluate aggregate morphologies, as discussed in section 2.4 and disperse phase aggregation processes[108,114].

In molecular dynamics a set of coupled equations of motion, usually ordinary differential equations, for many-body systems, is solved using finite difference techniques[29]. The method has been widely applied to homogeneous systems such as monoatomic liquids to produce the correct time ordering of the generated configurations. However, for mixtures like colloidal dispersions where hydrodynamic and stochastic forces must be correctly included as well as the usual interparticle interactions, this method is hardly practical at present because of the complexity and computational cost involved[29]. In mixtures containing different particulate species such as dispersions of macromolecules or colloids, the timescale characterising the motion of each species can differ by several orders of magnitude[29]. To simulate such systems using the standard molecular dynamics methods would require extremely short time intervals to handle the fast motion of some species and exceedingly long runs to allow the slow evolution of the others. Thus, where the fast motions are not of great interest molecular dynamics methods are simply too demanding with respect to computing resources to be practical. Fortunately, approximate approaches such as Brownian dynamics can be used in such cases. In Brownian dynamics, the fast motion of solvent particles are omitted from the simulation and their impact on the solute is represented by a combination of random and frictional force terms[29]. The Newtonian equations of motion are replaced by Langevin-type equations of motion. Brownian dynamics type simulations are frequently used to solve the system evolution in disperse phase systems, for instance to investigate internal cluster structure and dynamics in heteroaggregation processes between different species[16,75]. One of the advantages of molecular dynamics over Monte Carlo is its ability to provide dynamic or time-dependent properties. Although these properties can be calculated with alternative methods in statistical mechanics, non-equilibrium molecular dynamics offer improved efficiency and enhanced versatility[29].

For completeness it should be briefly mentioned at this point that some studies use a combination of different simulation techniques, like sectional approaches on small scales with Monte Carlo simulations on large scales[82], in order to obtain models that are only as detailed as necessary.

4.4 Application context

In order to investigate the dynamics of directed self-assembly processes for the targeted delivery of drugs to cells, this thesis focuses on heteroaggregation phenomena between different particulate species. The aggregation is simulated by means of multivariate population balance models. Although multivariate population balance equations provide a convenient method for describing aggregation in multiple species systems, most models in the literature concerning aggregation remain restricted to homoaggregation[79,128,133]. Recently, an overview of multivariate population balance formulations for other than crystallisation applications was published by Briesen[11]. The physical complexity of heteroaggregation processes in multi-species systems results in a lack of exact kernels which efficiently couple the aggregation rate to the aggregate composition distributed over property state space. The development of appropriate kernels is an area of ongoing research[30,98,101,102,103]. Exact expressions and further details concerning the establishment of property state space, the population balance equation and the aggregation rates will be discussed later in sections 6.1 and 8.1. At this point only a succinct classification of the model according to the outlined criteria is intended. In addition, some assumptions and specifications of general impact to the work of this thesis are made beyond the restriction to binary particle interaction and the decoupling of particle transport and attachment, which were mentioned in the introductory comment of this chapter.

4.4.1 Derivation of a population balance equation for particle aggregation

One very important assumption is that all investigated particle suspensions are considered as homogeneously mixed so that $\vec{x}$ can be neglected and $\vec{P} = \vec{e}$. The hydrodynamic conditions within the suspension are therefore approximated by a step-like behaviour, ensuring complete mixing of all particle species by turbulence before, but purely diffusive (perikinetic) regimes after the experiment begins. Experimentally this is realised by gentle shaking directly following the addition of particle all particle species. As expected some particle aggregation was observed during the initial mixing phase. In order to consider this in the simulation, the beginning of each experiment was defined as the time when the first sample had been analysed in the flow cytometer. The measured initial distribution of aggregate composition could then be used as initial condition for solving the population balance equation and the hydrodynamic turbulences are assumed to have decayed, yielding a perikinetic regime. Although the time scale for a total decay of convective motion is probably longer, the assumption of a step like mixing behaviour represents a good compromise between model complexity and physical reality and is supported by the very good reproducibility, demonstrated in Chapter 5.

Furthermore, the liquid suspension is considered as a closed system. Due to homogeneous mixing any influence of the extracted sample volume on the aggregation dynamics is not expected. With the complete lack of any spatial dependence, no convective and diffusive spatial transport terms across the boundaries of the control volume exist, i.e. $\vec{\nabla}_x \cdot \vec{\phi}_{N,x}(\vec{e}, \vec{x}, t) = 0$. If we further assume that property related convective and diffusive transport, like crystal growth, may remain unconsidered in

aggregating colloidal systems with $\vec{w}_e = 0$ and $\vec{\phi}^D_{N,e} = 0$, the population balance equation (4.7) simplifies to

$$\frac{\mathrm{d}f(\vec{e},t)}{\mathrm{d}t} = \sigma_N(\vec{e},t) = \dot{f}^{\pm}_{Agg} \,. \tag{4.16}$$

In Eq. (4.16) we already considered that in the systems of interest, the source/sink term only contains the aggregation contribution. Nucleation and dissolution remain unconsidered and in perikinetic regimes, where hydrodynamic shear forces are negligible, aggregate breakage is also negligible. The neglect of breakage events corresponds to simulating the aggregation process with net-rates.

Since in our investigations the population balance equation accounts for the distribution of particles or particulate entities throughout the state space, the properties $\vec{e}$ that span open the property state space $\mathcal{P}$ are intuitively constructed from all possible discrete particle numbers for each species. The population balance equation then has to be recast in a discrete manner. In the system of interest, the particle species are electrostatically stabilised against homoaggregation. Due to the differences in particle properties between the species, mixed clusters will form due to heteroaggregation. The heteroaggregation comprises two distinct contributions: the attachment of monomeric primary particles to the clusters and the aggregation of clusters themselves. Throughout this thesis, the first contribution will be termed *primary heteroaggregation* and *secondary* or *cluster-cluster aggregation*, respectively. The attachment of monomeric particles from the environment to clusters is identical to aggregation along a single property dimension. For the unconstrained secondary aggregation term, the summation has to be performed over all dimensions of state space. In binary particle heteroaggregation this is expressed by the separate summation over both properties $\vec{e} = (i\ j)^T$, which represent discrete particle numbers constituting the aggregate and span open state space. The conservation of particle numbers $\vec{e}'' = \vec{e} - \vec{e}'$ can be expressed as $i'' = i - i'$ and $j = j - j'$ in the source and sink terms for a binary system. Both effects are included as separate terms in the following expression:

$$\begin{aligned}\dot{f}^{\pm}_{Agg} = &\underbrace{\left[\omega\left(\vec{e}',\vec{e}'',\vec{y}(t)\right)\cdot f\left(\vec{e}',t\right) - \omega\left(\vec{e},\vec{e}'',\vec{y}(t)\right)\cdot f(\vec{e},t)\right]\cdot f\left(\vec{e}'',t\right)}_{\text{primary heteroaggregation}} \\ &+\underbrace{\frac{1}{2}\sum_{i'^*}\sum_{j'^*}\omega\left(\vec{e}',\vec{e}'',\vec{y}(t)\right) f\left(\vec{e}',t\right) f\left(\vec{e}'',t\right) - f(\vec{e},t)\sum_{i'}\sum_{j'}\omega\left(\vec{e},\vec{e}',\vec{y}(t)\right) f\left(\vec{e}',t\right)}_{\text{secondary heteroaggregation}}\end{aligned} \tag{4.17}$$

in which i'^* and j'^* represent regions within property space. Primary aggregation is given by $P(\vec{e}',t) + P(\vec{e}'',t) \rightarrow P(\vec{e},t)$. with $P(\vec{e}'')$ representing the monomer educt particle.

For discrete systems, where the property space is spanned open by particle numbers, the number density function $f(\vec{e},t)$ is equivalent to the number concentration $c(\vec{e},t)$ of particles within a certain spatial volume. This follows from the formal unit of the number density function $[f] = \Pi_k^K [e_k]^{-1} \cdot m^{-3}$, in which $[e_1] = [e_2] = 1$ for particle numbers[42]. In the following, the number density functions are replaced by the particle number concentrations $c(\vec{e},t)$.

4.4.2 Solution method

As shown in section 4.4.1, the heteroaggregation processes in the investigated multi-species systems can be described by simple, yet highly coupled, systems of ordinary differential equations. From physical considerations, these are defined in a fully discrete manner with respect to the property coordinates. Therefore no artificial discretisation has to be established in order to solve them numerically on a computer. However, the computational costs of solving systems with fully occupied state spaces might impede a numerical solution. System size can efficiently be reduced by focusing on regions in property space with high aggregate concentration. To this end a zero-order sectional approach with varying interval spacing is applied, which creates regions of property space with heterogeneous resolution levels. The interval spacing can be determined on a heuristic basis and may be adaptively refined according to the drift of the aggregate distribution within the property space.

In the investigated particle and cellular systems, the aggregation process over the respective analysed time spans yields aggregates of limited configurations only. Therefore, it is possible to choose the absolute particle numbers of each species as finest discretisation in areas of high particle concentrations, i.e. the property coordinates are directly used as nodes around which population balances are set up. Also, it seems convenient to lump all aggregates outside of this highly resolved region into very few representative coordinates with averaged properties and thus restrict the analysis to two resolution levels. To regulate the extent of the fine region a scaling parameter ξ is introduced, which determines a cut-off criterion as percentage of the particle fraction contained in a certain property node. For very large regions of fine discretisation this factor is selected small, for small ones it is chosen greater.

In the binary particle system discussed in Chapter 5, a combination of fixed and adaptive grids is applied to resolve the evolution of the distribution on each property axis, while for the biological system an independent adaptive grid is used for each species in Chapter 7. Numerical solutions were generated with MATLAB on a conventional desktop computer.

There a two striking advantages of applying this method. For one, in the areas of high aggregate concentration with maximum resolution essentially no system information is lost by global approximation rules. Therefore, most approximations on the boundaries of the discretised elements are avoided. Some minor inaccuracies are generated on the boundaries to the regions of low resolution, but these are of negligible influence. This is why very low numerical diffusion was achieved over the simulated time span.

Part II

Heteroaggregation in multi-dimensional particle systems

When studying colloidal dispersions, many different physiochemical factors have to be understood in order to optimise their use in industrial processes[66]. Important technical use of colloids is made in separation processes, like filtration and flotation[48], or in the production of emulsions and foams[65]. In addition to their traditional use, promising new fields are opening up with investigations of self-assembly and biomedical applications of nanotechnology. For instance, specific colloid aggregation could prove essential for biological separation processes, like affinity precipitation[59], or for cell targeting and drug delivery issues as discussed in this thesis.

As was shown in Chapter 2 of the previous theoretical part, colloidal stability depends on the interactions that occur between the dispersed particles and also between the particles and the solvent. When particles are suspended within a medium, random particle collisions are inevitable. These can be the result of intrinsic Brownian motion, or of external forces, such as shear from agitation and flow or gravitational forces in case of sedimentation. As a consequence aggregation may occur and, depending on the particle properties, may result in permanent contact referred to as coagulation, or temporary contact which is known as flocculation[66].

When a system contains only one type of particles, the kind of interactions that predominate will differ from situations where more than one particle species co-exist within the same medium[66]. The particles may differ in a variety of ways, for example in composition, shape, size, surface potential and charge. Aggregation in single species systems is called homoaggregation, while the instability of multi-species colloidal dispersions is referred to as heteroaggregation[29,66,90]. Although homoaggregation is the more widely studied field, it is nevertheless inadequate in explaining many heteroaggregation phenomena, due to the complexities which result from the mixing of different particulates[66]. One important feature of heteroaggregation is that particles which are colloidally stable, for instance by electrostatic repulsion, may readily adsorb to a surface of a different particle type, with which there is no repulsion. Given a large difference in particle size, smaller particles then adsorb onto the surface of the larger species. When the whole surface is covered, the surface properties of the larger coated particle become similar to those of the small particles, which may cause restabilising effects[66].

As aggregation processes become ever more complex in their applications, heteroaggregation gains in importance. A review on experimental and simulation aspects of heteroaggregation was recently published by Lopez-Lopez *et al.*[90]. In contrast to homoaggregation, where aggregates can be adequately described by cluster size and structure, heteroaggregation demands a multidimensional aggregate analysis to determine the cluster composition, for instance by means of flow cytometry. In this second part of the thesis, the dynamic evolution of the cluster composition in mixed particle systems is studied experimentally and by simulation. In Chapter 5, flow cytometric measurements are presented, which enable a detailed analysis of the heteroaggregation dynamics. To validate model predictions from colloidal science, the particle interaction potentials were characterised by colloidal probe microscopy. On the basis of theoretical interaction potentials a rate model for heteroaggregation in perikinetic systems is developed in Chapter 6. The rates are used in a population balance equation to describe the predominant electrostatic effects during aggregation. The investigations provide the methodological tools for a rigorous approach to targeting processes in biological systems discussed in Part III and were published/are submitted in four journal contributions[119,120,121,122].

Chapter 5

Experimental aggregation dynamics

The dynamics of heteroaggregation processes in multi-species particle systems were investigated by flow cytometry. The high level of detail, with which simultaneous homo- and heteroaggregation processes can be resolved by tracking the cluster composition, is used to enhance the physical insight into the consecutive interplay of distinct electrostatic effects. To this end particle species differing in size and surface properties were selected. The employed materials and experimental methods for all three are summarised in sections 5.1 and 5.2 with a special emphasis on the acquisition and analysis of flow cytometric data. In total three experimental aspects are discussed in this chapter. Starting off with investigations of binary particle systems in section 5.3, the principal electrostatic aggregation phenomena are discussed. This is followed by section 5.3.3 which highlights the influence of microscale differences in particle interactions on macroscale aggregation behaviour by employing colloidal probe microscopy. It prepares the stage for the population balance simulations in Chapter 6. Finally, the methods established for binary systems are successfully applied to ternary particle systems and dosage experiments in section 5.4.

5.1 Materials

In all investigations, purchased monodisperse particle suspensions of polystyrene (PS) and melamine-formaldehyde (MF) latices with spherical geometry were used. Depending on the investigated aspect, the particle size, its fluorescent label and the manufacturer vary. All particle suspensions were used as delivered and their characteristics are shown in Table 5.1. In most experiments the particle species were diluted in deionised MilliQ water (Millipore, USA). For some experiments, the ionic strength was increased to 2 M by addition of NaCl (99.5% purity, Roth, Germany).

In the preliminary investigations of binary mixtures, 2 μm sized negatively charged PS particles and 366 nm sized positively charged MF particles were obtained from microParticles GmbH (Berlin, Germany). The MF particles were fluorescently labelled with Rhodamine B, which features an excitation maximum at $\lambda_{ex} = 560$ nm and an emission maximum at $\lambda_{em} = 584$ nm. For confocal imaging by laser scanning microscopy, the non-fluorescent PS particles were exchanged with green fluorescent PS particles (PS-Fluo) from the same manufacturer. The excitation and emission maxima of this fluorophore are similar to fluorescein isothiocyanate (FITC) with $\lambda_{ex} = 506$ nm and $\lambda_{em} = 529$ nm, but show less sensitivity to photobleaching.

Investigations in binary systems were extended by exchanging the PS particle suspension with that of a different manufacturer. Instead of PS latices from microPar-

ticles, 2 μm PS particles of Duke Scientific (Thermo, USA) with more negative surface potential were used. Together with pronounced deviations in the aggregation dynamics this indicates different surface functionalisation between the two particle suspensions.

Finally, the investigations of ternary mixtures are based on 2 μm sized negatively charged PS particles from Duke Scientific (Thermo, USA). The other two species were positively charged MF latices from microParticles, one with a diameter of 530 nm and FITC as fluorescent label, the other of 2 μm in diameter and fluorescently marked with Rhodamine B.

Table 5.1: Characterisation of the particle systems used in the aggregation studies. The following abbreviations were used: polystyrene (PS), melamine-formaldehyde (MF), Rhodamine B (RhB), fluorescein isothiocyanate (FITC).

Particles	Manufacturer	c^M [w/v %]	d [μm] [a]	ζ [mV] [b]	Fluorophore	Sections
PS	microParticles	2.0	1.998	-48	-	5.3.1-
MF-RhB	microParticles	2.5	0.366	+43	RhB [c]	5.3.2
PS	Duke Scientific	0.4	1.998	-82	-	5.3.3
MF-RhB	microParticles	2.5	0.366	+43	RhB [c]	
PS	Duke Scientific	0.4	1.998	-82	-	
MF-RhB	microParticles	2.5	2.0	+25	RhB [c]	5.4
MF-FITC	microParticles	2.5	0.530	+43	FITC [d]	

[a] nominal diameter determined by the manufacturer
[b] ζ-potential determined with a Zetasizer Nano ZS, Malvern, UK
[c] $\lambda_{ex} = 560$ nm, $\lambda_{em} = 584$ nm
[d] $\lambda_{ex} = 506$ nm, $\lambda_{em} = 529$ nm

5.2 Methods

5.2.1 Experimental procedures

The experiments were carried out in 50 ml polypropylene centrifuge tubes (Sarstedt, Germany) which were thoroughly rinsed with deionised water before use. In all experiments non-fluorescent PS particles were diluted to $c_{PS} = 1.14 \cdot 10^4$ particles/μl in 30 ml MilliQ water (Millipore, USA). This concentration was empirically adjusted to the optimal operating conditions of the flow cytometer at detection rates of 1500 to 2000 events/s. At the same time sufficient aggregate concentration is guaranteed for experiments at $c_{PS}/2$ in section 5.3.1, which becomes especially important towards the end when the particle concentration is depleted due to aggregation. To achieve elevated electrolyte concentration in section 5.3.2, the PS particles were diluted in 2 M NaCl (99.5% purity, Roth, Germany) solution instead of deionised water.

The experiments were initiated by adding the other particle species in appropriate quantities to achieve a desired mixing ratios within the total liquid volume. To this end, small volumes of the other particle suspensions were prediluted with 200 μl MilliQ water of which about 150 μl were added to the total volume of 30 ml. In the binary mixtures, the particle concentration ratio was varied from $c_{MF-RhB}/c_{PS} = 1{:}1$ over 20:1 to 100:1. Experiments with intermediate ratios of 5:1, 10:1 and 50:1 were

also conducted, but do not contain any additional information. In the ternary mixtures both MF particle species were added simultaneously at the beginning of each experiment in ratios of $c_{PS}/c_{MF-FITC}/c_{MF-RhB} = 1{:}20{:}1$ or 1:1:1. The total solid volume fraction always remained below $5 \cdot 10^{-3}$ %.

Directly after addition of all species, a homogeneous distribution of the particles throughout the liquid volume was established for perikinetic investigations by gently tipping the tube over once. This led to an accelerated formation of heteroaggregates prior to the first measurement taken immediately after mixing. To verify the reproducibility of the initial condition, several repetitions of selected experiments were made in the binary systems of section 5.2.2. In Figure 5.2, the initial flow cytometric measurement shows maximum standard deviations between the experiments of 1.6 % for monomers, 8.3 % for dimers and 10.6 % for trimers. Because these three aggregate structures initially account for > 98 % of all particles, reproducibility is confirmed. If not specified otherwise, perikinetic conditions were maintained throughout the remaining experiment. To obtain the cluster composition, samples of 200 μl volume were taken at various times and analysed in the flow cytometer.

To demonstrate the sensitivity of flow cytometric analyses against orthokinetic hydrodynamics regimes and further particle dosage, variations of experimental parameters were made. In section 5.3.1, orthokinetic conditions were generated by continuously agitating the liquid volume with a magnetic stir bar at constant speeds of 250 or 500 rpm inside a cylindrical liquid volume of 30 ml. Initial mixing by tipping the tube over once was omitted here. In section 5.4 two experiments with intermittent dosage of additional PS particles are shown. At $t = 30$ min or 1 h, the concentration of PS primary particles was instantaneously raised by an additional $c_{PS}^{add} = 0.57 \cdot 10^4$ particles/μl, half the initial concentration.

Generally all experiments were conducted at a room temperature of approximately $T = 298$ K. Additional experiments were carried out to study binary aggregation dynamics at an elevated temperature of $T = 310$ K as reported in section 5.3.1. For the particle species volumetric forces are considered to be small compared to the force causing Brownian motion. This is ensured by the small density difference between PS particles and water, and the small size for MF particles being of higher density. Sedimentation effects could therefore be neglected for experiments of approximately 6 h duration.

5.2.2 Flow cytometric analysis of aggregation

The Epics XL flow cytometer was used to measure the multi-dimensional cluster distributions. In binary systems two-dimensional distributions of the forward scatter intensity (FS) and the fluorescence intensity at $\lambda = 575$ nm ($FL2$) were studied. The $FL2$ channel coincides with the emission peak of Rhodamine B, which labels the MF particles. A three-dimensional analysis was made in order to characterise cluster compositions in ternary mixtures. Similar to binary systems, the large particle species were detected by the forward scatter intensity. Aggregate fluorescence was detected on the $FL1 = 525$ nm channel for the MF-FITC particles and the $FL2 = 575$ nm channel for the MF-RhB particles.

Prior to experiments, the scatter and fluorescence detector voltages were optimised, to ensure that the whole aggregation process would not exceed the signal ranges. The

settings were established with unmixed particle suspensions and stored in standard operating procedures (protocols). For reasons of reproducibility all measurements were conducted with the same respective protocols. Detector voltages were adjusted to show the PS monomers at about $FS = 10^2$ a.u. and the mean fluorescence intensities of the labelled monomers at $FLx = 10^1$ a.u., both with logarithmic scaling. The SS intensity was measured on a linear scale detecting the PS particles at low intensities. Any effects due to differences in the refractive indices of PS and MF particles, i.e. 1.59 and 1.68 relative to water, on the scatter signal during heteroaggregation are neglected. In ternary systems, the fluorescence intensity of the MF-FITC particles was low compared to that of the MF-RhB particles due to the large difference in size. The sensitivities of both fluorescence channels were adapted accordingly: high sensitivity in $FL1$ and low sensitivity in $FL2$. This had the positive side effect, that the signal cross-talk between the $FL1$ and $FL2$ channels did not have to be compensated. The spill-over of FITC into $FL2$ was negligible due to the different sensitivities, and Rhodamine B did not have influence on the $FL1$ intensity.

In each measurement 20000 events were evaluated. However, with proceeding aggregation both aggregate concentration and count rate decrease. To avoid exceedingly long measurement times and increased sample volumes, a maximum measuring time of 100 s was set. Once the flow cytometer reached either of the abort criteria (20000 particles or 100 s), the measurement was terminated. The sample volume for each measurement was less than 200 μl.

After the cluster composition was measured by the flow cytometer, the data was analysed in multiple post-processing steps of varying complexity. The raw data can be represented in two-dimensional dot plots as explained in section 3.2.2. Dot plots represent snapshots of the aggregation status at sampling time t. By analysing the particle distribution inside specific regions, a series of snapshots can be transformed into time-dependent aggregation dynamics. In the analysed particle systems, different resolutions were obtained on the scattering and fluorescence intensity axes. For the primary particles in the micrometre range (PS and large MF-RhB), different aggregation states are directly indicated by a discrete signal distribution. For submicron particle species (small MF-RhB and MF-FITC) the fluorescence intensities changed gradually, so that exact particle numbers could only be obtained by correlations as explained in section 5.2.2.4.

5.2.2.1 Analysis of binary systems

In the binary system, gating was performed with respect to the discretised FS intensity. Figure 5.1 shows a sample dot plot. In total three manually adjusted regions are indicated characterising PS primary particles, MF-RhB covered PS monomers and complex oligomers of mixed composition. Faced with several more clearly visible discrete aggregation states which would allow a much more detailed analysis, the artificial restriction to only three regions may seem a little crude. However, clarity is considerably improved by lumping all PS oligomers into a single region and for a detailed understanding of the aggregation process these three regions suffice. The cluster composition of each region is indicated by a two element vector (i, j) related to the number of PS and MF-RhB particles, respectively. Monomeric MF-RhB particles could not be detected very well in the flow cytometer when mixed with PS particles. This is because PS aggregates dominate both the FS and $FL2$ signals due to their size, which causes high scattering intensities and high fluorescence when cov-

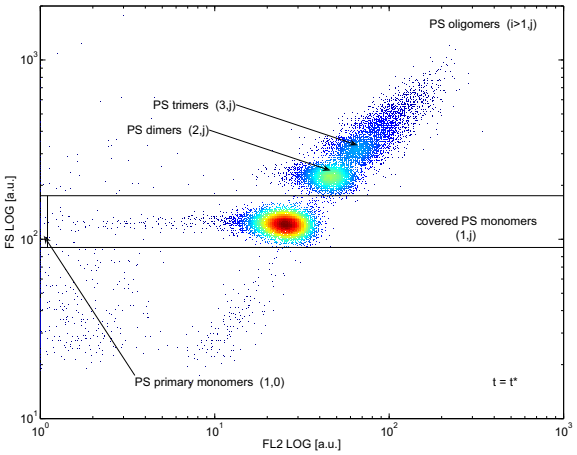

Figure 5.1: The two-dimensional dot plot coloured by event density shows the distribution of cluster composition in a binary mixture of 2 μm PS and 366 nm MF-RhB particles.

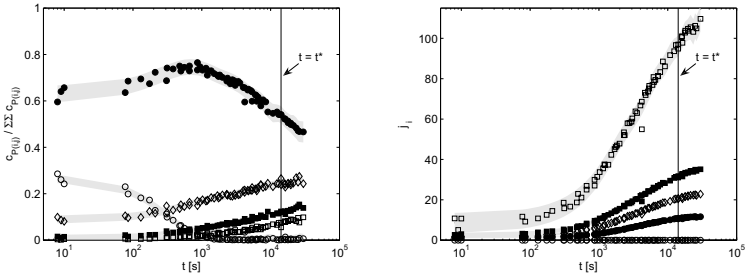

(a) PS aggregate fractions.

(b) MF-RhB coverage of PS aggregates.

Figure 5.2: Reproducibility and experimental error of flow cytometric measurements of aggregation dynamics in binary particle mixtures. The information of three repetitions is presented along with the 95% confidence interval that is indicated as shaded area. The values at $t^* \approx 4$ h indicated by vertical lines were obtained from the dot plot in Figure 5.1. The plots show a representative perikinetic experiment with $c_{PS} = 1.14 \cdot 10^4$ particles/μl and a ratio of $c_{MF-RhB} : c_{PS} = 20{:}1$ at $T = 298$ K and $c_M^{NaCl} = 0$ M. PS primary monomers (○), covered PS monomers (•), PS dimers (◇), PS trimers (■), PS oligomers (□).

ered by MF-RhB. Some monomeric MF-RhB particles appear below the gates around $FL2 = 10^1$ a.u. in the dot plot. In all experiments identical regions were applied, except at elevated electrolyte concentration, where they had to be corrected slightly. This minor deviation of the FS signal at increased ionic strength is likely to be caused by the changing refractive index of the medium.

Inside each region, the particle fraction and mean fluorescence intensity were recorded. By plotting these values for each measurement in a single experiment against the experimental time t, the aggregation dynamics are obtained. For a representative ex-

periment, these are shown in Figure 5.2, together with two repetitions. The included 95% confidence interval around all experiments is very narrow over the complete aggregation experiment. This shows the excellent reproducibility of the initial condition (section 5.2) and the experiment on a whole.

5.2.2.2 Analysis of ternary systems

In ternary systems, the complete distribution information has to be represented in a three-dimensional distribution plot, like the ones shown in Figure 5.3. As before, increasing signal intensities indicate aggregates growing in size and complexity. The analysis of aggregation dynamics in three-dimensional plots is, however, more difficult. That is why, two-dimensional projections of the original dot plot are preferred for the analysis of the cluster composition and for the definition of regions. In Figure 5.4 two projections of the FS signal against both fluorescence signals $FL1$ and $FL2$ are shown.

Several regions of distinct cluster composition are indicated by the three element vector (i, j, k) representing PS, MF-FITC and MF-RhB particle species respectively.

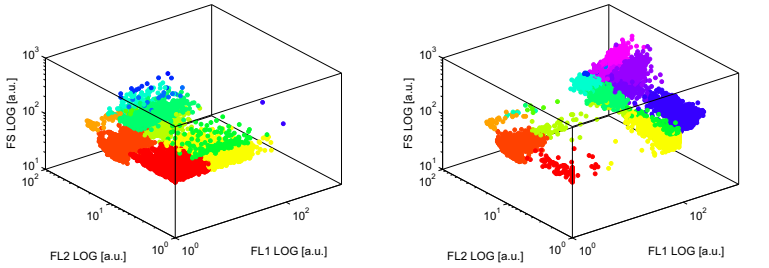

(a) Initial distribution directly after mixing of all particle species.

(b) Distribution after 10.5 h of perikinetic aggregation.

Figure 5.3: Three-dimensional distribution plots of ternary cluster composition. Colour coding performed according to the gates indicated in Figure 5.4.

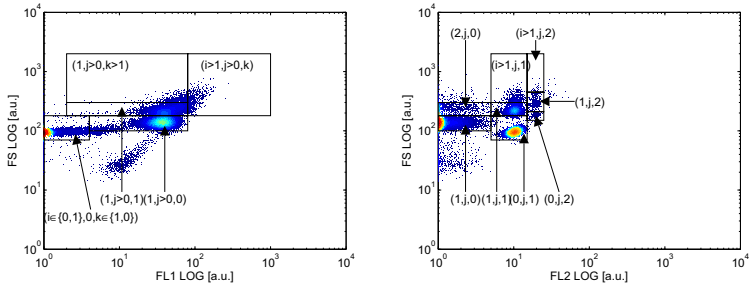

Figure 5.4: Two-dimensional dot plot projections of the cluster distribution in a ternary particle system. PS particles are detected on the FS, MF-FITC on the $FL1$ and MF-RhB on the $FL2$ channel. Several distinct cluster compositions are indicated by composition vectors (i, j, k). Colour coding according to number density.

Unspecified particle numbers are indicated by the general index, as in $(1, j, 0)$ for PS monomers covered with several MF-FITC particles. Because PS and MF-RhB primary particles are equally sized, both species show up in the same gate of the FS vs. $FL1$ plot with composition vector ($i \in \{0, 1\}, 0, k \in \{1, 0\}$). A distinction can only be made by additionally considering the $FL2$ signal. As done previously for the binary system, the gates are analysed with respect to particle fraction and average fluorescence intensities.

5.2.2.3 Validation of cluster concentration and composition

All considered particle concentrations were gained by theoretical calculations. They are based on manufacturer information that characterises the original suspensions. To validate, that all particles are detected by the flow cytometer and that the measurements are reliable, theoretical concentrations were confirmed by validation studies. The validation of particle concentration focuses on the initial PS concentration of $c_{PS} = 1.14 \cdot 10^4$ particles/μl, from which all other concentrations are calculated by the applied ratios and which therefore is of central importance. The particle concentration can be derived from each measurement by the following relation

$$c_{PS}^{exp} = \frac{N_{PS}}{t^{exp}\,\dot{V}^{exp}} \tag{5.1}$$

with N_{PS} as absolute number of PS particles detected in a flow cytometric measurement, t^{exp} as measurement duration and $\dot{V}^{exp}$ as flow rate during measurement. The amount of PS particles, N_{PS}, is usually less than the limit of 20000 events set by the abort criterion (see Section 5.2.2), since a small amount of MF-RhB particles and contaminating particles add to the total count. These have to be excluded by appropriate gating. The total particle number was therefore determined by the sum of all particles within any of the region indicated in Figure 5.1. The lower bounds of the PS primary and oligomer particle gates were chosen as $FL2 = 0$ a.u.. The duration of each measurement t^{exp} is automatically recorded by the flow cytometer software in full seconds. To calibrate the flow rate, experiments with bead suspensions of exactly known concentration (Flow Count Fluorospheres, Beckman-Coulter, USA) were conducted. Transient deviations at the beginning of a measurement were neglected. Thus, a mean flow rate of $\dot{V}^{exp} \approx 9.8 \pm 0.25$ μl/min could be determined. Given the flow rate, the deviation of theoretical to experimental PS monomer concentration for each initial measurement can be calculated. The errors $(c_{PS}^{exp} - c_{PS})/c_{PS}^{exp}$ of all experiments shown in this contribution range from a minimum value of -15 % to a maximum value of 41 % and scatter around a mean of 13 % with a standard deviation of 16 %. Since the error is sensitive to parameter inaccuracies, deviations of 13 % can be considered as reasonably accurate. For example, a flow rate deviation of ± 1 μl/min, results in error differences of $\approx \mp 9$ %.

Apart from the verification of matching theoretical and experimental particle concentrations, the distribution of PS particles between different cluster compositions was determined by light microscopy. For selected measurements the numbers of PS monomers, dimers, trimers and oligomers were manually counted in a Thoma haemocytometer (Assistent, Germany). The results are plotted in Figure 5.5 and agree well with those of flow cytometric measurements. This essentially confirms that the cluster composition is not influenced by the measurement and that the detected distributions are reliable. Hydrodynamic shear forces acting on the aggregates

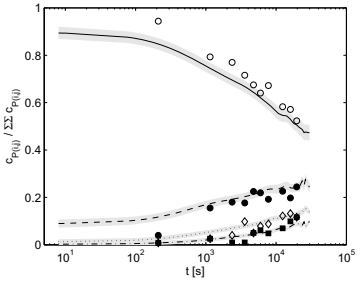

Figure 5.5: Validation of PS aggregate distribution by light microscopy (scattered data). Flow cytometric data is copied from Figure 5.2(a) and represented by lines. PS monomers (○, ——), PS dimers (•, – –), PS trimers (◇, · · ·), PS oligomers (■, –·–·–).

are not strong enough to cause breakage, as was already shown for similar systems by Plessers et al.[110] in contrast to the previous findings of Bowen et al.[9]. The introduction of a sheath stream surrounding a thin sample stream considerably reduces hydrodynamic shear acting within the sample, so that flow cytometers also guarantee the survival of shear sensitive cells after measurement.

5.2.2.4 Quantification of cluster composition

There are essentially two possibilities of relating the signal intensities with the absolute particle number causing it. The easiest way is that the signal itself shows discretised areas which directly indicate the number of constituent particles. Depending on the electronic resolution of the flow cytometer and the protocol settings, aggregates of micrometre sized particles usually produce discrete distributions. This applies for the *FS* signal of PS aggregates as well as for the *FL*2 signal of the 2 μm MF-RhB particles. Smaller particle species like the 366 nm MF-RhB or the 530 nm MF-FITC particles, however, generate gradually changing continuous distributions only. Because the fluorescence intensity is subject to nonlinearities, the absolute particle number in these cases can only be determined by means of a correlation. A common method to conduct quantitative flow cytometry is the calibration with mean equivalents of soluble fluorochrome (MESF)[44]. By comparing the detected fluorescence intensity of the sample with that of purchased calibration particles with known amount of bound fluorophore, estimates of the fluorophore amount in the sample aggregates are gained[44]. Due to possible specific fluorophore interactions, it is strongly advised that sample and MESF fluorophore be identical. If this method is applied to identify an absolute particle number, it is required that each particle contains comparable amounts of fluorophore. Another possibility to correlate fluorescence intensities with particle numbers is given when fluorescent particles of different sizes with equal fluorophore concentration profiles throughout the particle volume are available. Then a constant volume specific fluorescence intensity can be determined that correlates the detected fluorescence intensity to a total particle volume. However, since neither MESF calibration beads for Rhodamine B nor particles with guaranteed equal volume specific fluorophore concentration could be obtained, an alternative method for converting the fluorescence intensities into absolute particle numbers was applied. The most direct approach to relate fluorescence intensities with particle numbers is by way of mi-

croscopy. Similar to the validation studies mentioned in paragraph 5.2.2.3, the number of small MF-RhB particles bound to PS monomers can be manually counted in a Thoma haemocytometer (Assistent, Germany) and related to the fluorescence intensity observed in a parallel flow cytometric measurement. Due to restricted visibility, the calibration is based only on samples with low MF-RhB coverage (one to four particles) taken in the early phase of selected measurements. The specific fluorescence intensity per unit particle volume $fl2$ is calculated from the following formula

$$fl2 = \frac{FL2}{j\,V_{MF-RhB}} \tag{5.2}$$

with $FL2$ as fluorescence intensity, j as counted number of MF-RhB particles and V_{MF-RhB} as MF-RhB particle volume. By assuming a constant volume specific intensity $fl2$, this relation also serves to extrapolate j for any measured $FL2$ intensity. Microscopic counting of MF-RhB coverage on monomeric PS particles was performed in 39 cases, each comprising the information over approximately 90 ± 35 PS particles. After excluding six values that exceeded the standard deviation interval around the arithmetic mean value and could thus be considered as outliers, the average volume specific fluorescence intensity was determined as $\overline{fl2} = 1.05 \cdot 10^{20}$ [a.u./m^3] with a standard deviation of $\Delta fl2 = 4.77 \cdot 10^{19}$ [a.u./m^3] ($\approx 45\%$). Apart from the relatively high standard deviation, this calibration method retains uncertainty when extrapolating the data to higher fluorescence values.

5.3 Aggregation dynamics in binary particle systems

Numerous studies have been published recently, in which systems of binary particle mixtures with differences in size[16,147] or in other surface properties[35,41,75,86,113] were investigated. In this thesis PS and MF latices were used as binary particle system. The different particle characteristics are summarised in Table 5.1. The choice of particles with opposite surface charge promotes interesting electrostatic effects that dominate the aggregation behaviour.

Selected distribution plots of a representative experiment are displayed in Figure 5.6. The perikinetic experiment was conducted in deionised water at a PS concentration of $c_{PS} = 1.14 \cdot 10^4$ particles/μl and a particle ratio of $c_{PS}/c_{MF-RhB} = 20{:}1$ at room temperature. In each single-species suspension, homoaggregation is prevented by repulsive electrostatic interparticle forces at low ionic strength. Figure 5.6(a) shows the initial distribution of PS and MF-RhB particles directly after mixing them together in 30 ml deionised water. At this early stage already some dimers and fewer trimers are visible. Measurements of the pure PS particle standard indicate that dimers are already contained in the original suspension, probably caused by an improper stabilisation. The fluorescence of the PS monomers quickly increases as can be seen in Figure 5.6(b). This is due to the small MF-RhB particles covering the surface of the larger PS particles. The formation of such 'raspberry' type heteroaggregates[66] is considered as primary heteroaggregation step. Depending on the extent of surface coverage, the heteroaggregates may now form a stable suspension or more complex aggregates consisting of multiple PS particles in a secondary aggregation step (cluster-cluster aggregation). Stable suspensions are obtained at very low coverages, where destabilisation by bridging is negligible, and for very high coverages, where the covered

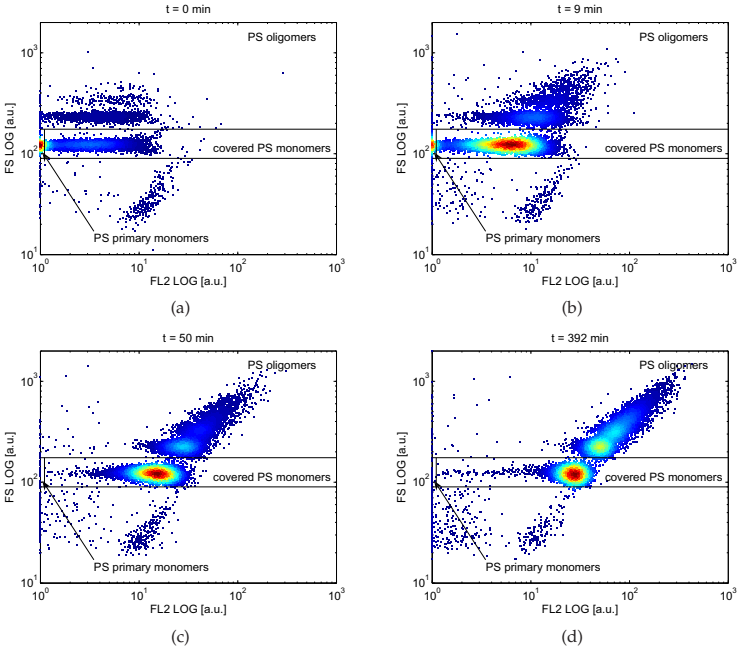

Figure 5.6: Time series of two-dimensional distributions of cluster composition in the binary particle mixture. The plots belong to the same experiment that was shown in Figure 5.1. The transition of primary into secondary heteroaggregation is clearly visible.

PS surface adopts similar properties of the MF-RhB particles and is essentially restabilised. Only at intermediate coverages, destabilisation occurs meditated by bridging between the heterogeneities of the cluster surfaces. The extent of surface coverage can be controlled by the macroscopic mixing ratio. At the considered particle ratio of 20:1, the coverage is high enough to facilitate cluster-cluster aggregation. The onset of cluster-cluster aggregation is indicated by the increase of PS oligomers with complex composition in Figure 5.6(c) and (d). The distinct 'islands' originate from the discretised resolution of PS particle number within an aggregate. High resolution FE-SEM micrographs of heteroaggregates are shown in Figure 5.7 and a laser scanning microscopic image using two fluorescent colours is shown in Figure 5.8. The two-step aggregation process is schematically represented in Figure 5.9.

The complete aggregation dynamics of the discussed 20:1 experiment were already plotted in Figure 5.2 in terms of fractions and mean fluorescence intensities reached inside the respective gates. Due to the increasing MF-RhB coverage of PS particles, the fraction of uncovered PS monomers decreases rapidly with a simultaneous increase in covered PS monomers. With the subsequent onset of secondary aggregation at sufficient coverage, monomeric heteroaggregates coagulate into oligomeric clusters. This generates a peak of covered PS monomers at around 1000 s. From the fluorescence signal at this time, the minimum surface coverage that facilitates secondary heteroaggregation can be estimated. The onset of secondary heteroaggregation occurs gradually, so that there is no explicit transition region. It is accompanied

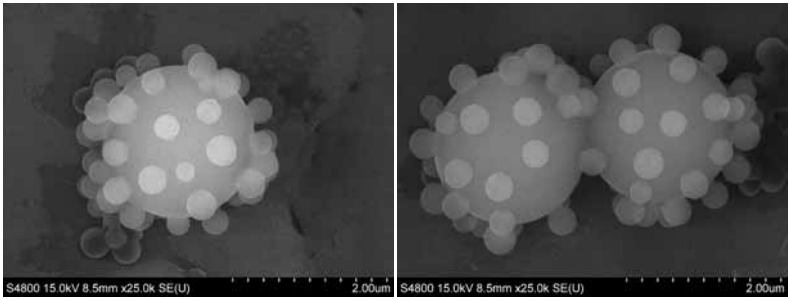

Figure 5.7: Electron micrographs of binary heteroaggregates of large PS and small MF-RhB particles. To arrest the morphology of the clusters for vacuum conditions, the aggregates were autoclaved at the glass temperature of polystyrene. This did not have direct influence on the aggregate morphology as was validated by means of fluorescence and laser scanning microscopy (data not shown).

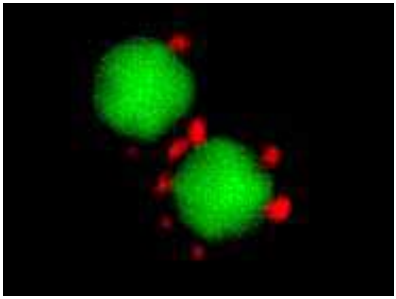

Figure 5.8: Laser scanning image of an heteroaggregate in deionised water. A dimer of PS-Fluo particles (green) form a clomplex cluster with MF-RhB particles (red).

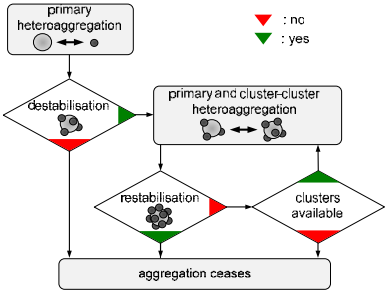

Figure 5.9: Schematic illustration of heteroaggregation phenomena in binary particle mixtures. Particle species are differently sized and oppositely charged. Primary heteroaggregation may be followed by secondary heteroaggregation depending on the surface coverage.

by primary heteroaggregation until either no more unbound MF-RhB particles are available or the PS clusters are restabilised, as illustrated in Figure 5.9.

The extent of surface coverage and hence the aggregation process on the whole can be controlled by modifying either the frequency of particle encounters or the collision efficiency. These two factors are considered to be uncoupled. Particle transport and colloid interaction can then be treated independently by encounter frequency and collision efficiency, as already mentioned in the introductory comment to Chapter 4. They represent the central constituents that determine the aggregation rates in the population balance simulations of section 6.1. Following the argumentation of Odriozola et al.[101] or Endres and Wingreen[30] for maximum likelihoods of time series, each encounter may comprise multiple collision events. Their frequency can be influenced by temperature, hydrodynamics and also by absolute and relative particle concentrations. The relative particle concentration is equivalent to the macroscopic mixing ratio of the particle species. The collision efficiency considers that only a fraction of

encounters is successful in establishing stable aggregates and is usually expressed by the reciprocal of the stability ratio W. With the introduced dependence on interaction energies, the collision efficiency is subject to versatile variations depending on material and medium properties, like the electrolyte concentration that plays a decisive role in electrostatically stabilised systems.

In the following, several experiments focusing on variations of encounter frequency and collision efficiency demonstrate the performance of flow cytometry as a measurement technique to investigate the dynamics of colloidal aggregation. Apart from particle concentrations, number ratios, temperatures and mixing modes which change the encounter frequency (section 5.3.1), the collision efficiency was modified by addition of NaCl to the continuous medium, affecting the charge screening by the electric double layer (section 5.3.2).

5.3.1 Variation of encounter frequency

The number of particle encounters inside a suspension is determined by several factors, which can all be attributed to the mean free path length travelled by the particles between two consecutive encounters. This path length can be manipulated by the particle concentration and particle ratio, or by changing the travelling speed of the particles, for instance by temperature variations or by imposing different hydrodynamic regimes. These factors were investigated for the binary particle systems by flow cytometry. The variations of particle concentration, temperature and mixing mode are presented in section 5.3.1.1 and meet expectations, thus demonstrating the reliability of flow cytometric quantification.

5.3.1.1 Variation of concentration, temperature and hydrodynamics

The experimental results for different particle concentrations ($c_{PS} = 1.14 \cdot 10^4$ particles/ μl and $c_{PS} = 0.57 \cdot 10^4$ particles/μl), temperatures ($T = 298$ K and $T = 310$ K) and mixing modes (perikinetic and orthokinetic with stirrer speeds of 250 rpm and 500 rpm) are summarised in Figure 5.10. All experiments were conducted at an intermediate particle ratio of 20:1 to facilitate cluster-cluster aggregation. The results confirm well-known behaviour at enhanced encounter frequencies.

All experiments show a similar dynamic behaviour: a sigmoidal decrease of PS primary particles (Figure 5.10(a)), a peak in covered PS particle concentration (Figure 5.10(b)), monotonically increasing oligomer concentration (Figure 5.10(c)) and sigmoidally increasing MF-RhB coverage of PS monomers (Figure 5.10(d)). Differences between the experiments are expressed by shifts in time scale. Also in the orthokinetic experiments PS monomers with low MF-RhB coverage reappear towards the end of the experiment. This phenomenon was not investigated further, but it is likely to be caused by grinding effects when particles get caught between the stirring bar and the tube wall.

Figures 5.10(a) and (d) show that primary heteroaggregation is accelerated with increasing concentration, temperature and shear forces. This results in earlier destabilisation and accelerates the onset of secondary heteroaggregation with PS oligomer formation, as seen in Figures 5.10(b) and (c). The hold-up of insufficiently covered PS monomers generates a peak in Figure 5.10(b), which changes in amplitude and

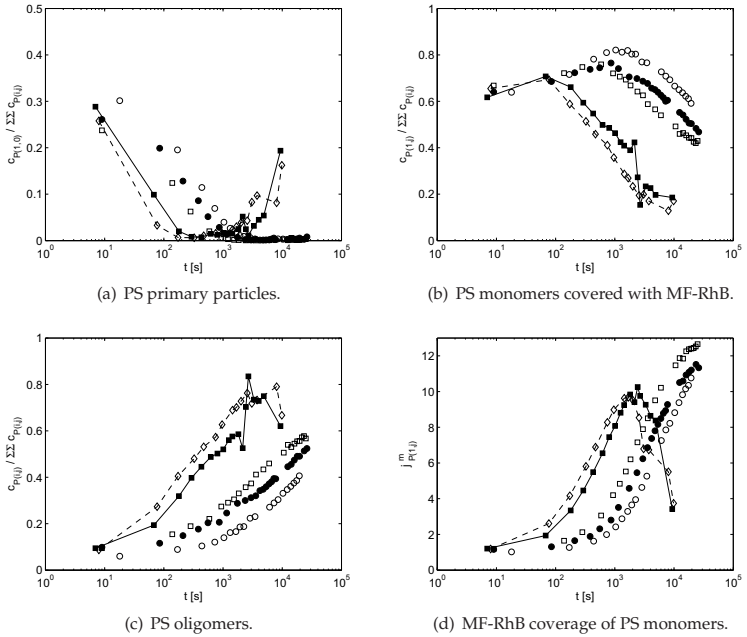

(a) PS primary particles.

(b) PS monomers covered with MF-RhB.

(c) PS oligomers.

(d) MF-RhB coverage of PS monomers.

Figure 5.10: Influence of PS concentration, temperature and shear force on aggregation dynamics. Standard experimental conditions imply a PS particle concentration of $c_{PS} = 1.14 \cdot 10^4$ particles/μl, a mixing ratio of $c_{MF-RhB}/c_{PS} = 20{:}1$ and $c_M^{NaCl} = 0$ M at $T = 298$ K in perikinetic regimes. Results are shown for standard conditions (•, from Figure 5.2), $c_{PS} = 0.57 \cdot 10^4$ particles/μl (○), $T = 310$ K (□), orthokinetic at 250 rpm (■, ——), orthokinetic at 500 rpm (◇, – –).

time for the individual experiments. With decreasing encounter frequency the amplitude grows and is postponed, indicating an extended destabilisation phase in which more covered PS monomers can accumulate before aggregating with other PS particles. Under the influence of stirring, particle encounter frequencies are increased by several orders of magnitude. This increases the aggregation dynamics tremendously compared to perikinetic experiments. Finally, a steady-state for a particle number ratio of 20:1 could not be reached in any of the experiments within 10^5 s. Longer measuring times would only be possible if the aggregates were not subject to sedimentation.

5.3.1.2 Variation of particle ratio

With increasing particle ratio at a fixed PS concentration, encounters between MF-RhB particles and PS aggregates become more probable and primary heteroaggregation occurs faster. The changing quality of the PS surface affects the aggregation efficiency and produces different aggregation dynamics. The aggregation dynamics for three different ratios, each representing a distinct electrostatic effect, are plotted in Figure 5.11. Substantial variations of the initial distributions resulting from the turbulent mixing are observed. These differences are inevitable in systems where

aggregation is allowed during the generation of homogeneously mixed particle suspensions.

In contrast to the aggregation dynamics for a 20:1 mixing ratio that were discussed as standard experiment above, no significant aggregation could be detected for a ratio of 1:1. The binding of a single MF-RhB particle occurs so fast, that most of the PS monomers already have a MF-RhB particle bound when the first measurement is performed. As is expected for this ratio, the average amount of surface MF-RhB particles remains steady at a single MF-RhB particle for the rest of the experiment as can be seen from Figure 5.11(d). Due to the low surface coverage, the probability of bridging between two clusters is rather low and the particles are not destabilised. The lack of destabilisation is expressed by the absence of PS oligomer formation in Figure 5.11(c).

As ratios increase beyond 50:1 very fast primary with almost no secondary heteroaggregation is observed and a near steady-state is reached towards the end of the experiment. Rapid primary heteroaggregation yields densely covered PS monomers as shown in Figure 5.11(d). This results in a gradual change of the cluster's surface property, which impedes further aggregation.

As illustrated in the process scheme in Figure 5.9, aggregation may cease either due to the lack of suitable clusters or due to restabilisation. While for the 1:1 and 20:1 ratios the first reason seems likely, the 100:1 mixing ratio is limited by restabilisation.

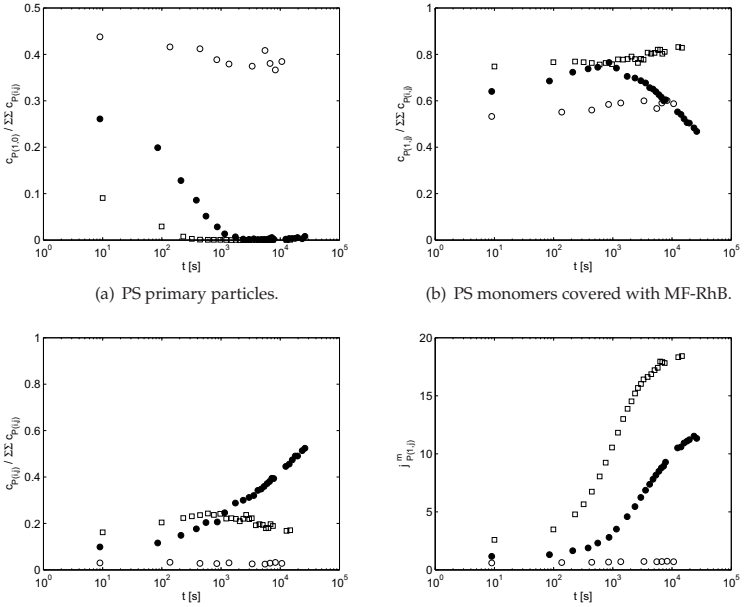

(a) PS primary particles.

(b) PS monomers covered with MF-RhB.

(c) PS oligomers.

(d) MF-RhB coverage of PS monomers.

Figure 5.11: Experimental aggregation dynamics for different bulk particle number ratios c_{MF-RhB}/c_{PS} = 1:1 (○), 20:1 (•, from Figure 5.2), 100:1 (□). The experiments were conducted at $c_{PS} = 1.14 \cdot 10^4$ particles/μl, $T = 298$ K, $c_M^{NaCl} = 0$ M, perikinetic.

In this thesis two alternative concepts are presented that cause for restabilisation. One approach is based on an average surface potential of the clusters obtained from a charge balance, the other considers geometric surface heterogeneities induced by MF-RhB particles on the PS surface (surface patches). Both approaches are explained in more detail in Chapter 6. Common to both is the introduction of a maximum MF-RhB capacity on PS particle surfaces, which might underscore a theoretical coverage implied by the macroscopic mixing ratio. For the 100:1 ratio, the final coverage does not exceed 20 MF-RhB particles per PS monomer (Figure 5.11(d)), from which we can conclude that aggregation is impeded by restabilisation and not by lacking of further MF-RhB particles. Unbound MF-RhB particles thus have to remain stable in solution. The rapid evolution of a restabilising MF-RhB shell for the 100:1 experiment is favoured by the high excess concentration of MF-RhB particles, kinetically outmatching cluster-cluster aggregation.

The observed onset of secondary heteroaggregation is not sharp, neither with time nor with process parameters, like the concentration ratio. Recalling that the probability of aggregation changes gradually when the sum of the interparticle energy becomes comparable to the thermal energy, no exact measure for the transition can be obtained. Furthermore, imperfect mixing may cause local non-uniformities that could result in deviations from the mean aggregate coverage and create some additional uncertainty.

5.3.1.3 Evolution of aggregate ζ-potentials

The electrostatic destabilisation and induced charge reversal of monomeric heteroaggregates was validated by ζ-potential measurements. All ζ-potentials were measured as intensity distributions. Similar to the flow cytometric analysis, unbound MF-RhB particles are dominated by signals from larger PS monomers or clusters, so that they are only detected as a second, smaller peak at high particle ratios $\geq$ 50:1 (data not shown).

Representative distributions throughout an experiment with a particle ratio of 20:1 are shown in Figure 5.12. Already from the beginning the distribution is bimodal, each peak representing different PS heteroaggregates. Towards the end of the experiment, the distribution narrows down to a single peak.

The evolution of average ζ-potentials with proceeding aggregation is shown in Figure 5.13 and supports the previous observations: for low particle ratios the ζ-potential changes only slightly and destabilisation of PS primary particles is not achieved, at elevated particle ratios aggregate charge monotonically increases with proceeding aggregation and even charge reversal is detected for the ratios 20:1 and 100:1. Following charge reversal, the aggregation process is continuously decelerated until eventually complete restabilisation is observed for the 100:1 ratio. The final ζ-potential is reached asymptotically and nearly matches the ζ-potential of the MF-RhB primary particles.

The differences in initial ζ-potential averages given in Figure 5.13 cannot be accounted for by different initial conditions of the suspensions after mixing alone. They seem to be subject to the concentration of MF-RhB particles: at high MF-RhB concentrations, the ζ-potential average is more positive than expected. This effect might represent an artifact of the measurement technique. Since the measurements are conducted in bulk sample, an influence of the particle majority by numbers on the particle minority seems likely. Such influences could result from cooperative scattering

effects or from hydrodynamic effects due to electrophoretic particle drifts into opposite directions.

5.3.2 Variation of encounter efficiency

The potential energies between the cluster surfaces play a decisive role in determining the aggregation behaviour within the mixture. This is clearly expressed by the two-step primary and secondary heteroaggregation processes. Interaction potential energies include van der Waals and electrostatic interactions as well as additional non-DLVO energies, as described in Chapter 2. Because the aggregation process in binary particle mixtures is predominantly mediated by electrostatic interactions, it is subject to the influence of the ionic strength of the continuous phase. With increasing electrolyte concentration, the additional ions shield the particle surface potential from its surrounding and the spatial extent of the double layer surrounding a cluster, represented by the Debye length $1/\kappa$, decreases. The influence of the electrostatic interaction is reduced and influence of thermal particle motion on aggregation becomes more dominant. The consecutive dependence of primary and secondary heteroaggregation is disrupted, and PS oligomer formation is possible without preceding destabilisation. This behaviour was confirmed by experiments at elevated ionic strength in 2 M NaCl solutions, shown in Figure 5.14. To improve the comparability of experiments with deviating initial conditions, relative values are used in this section. By normalising the particle fractions with their initial values, relative concentrations are generated that express deviation from the initial measurement as multiplying factors

In Figure 5.14(a) the aggregation dynamics at an elevated electrolyte concentration of $c_M^{NaCl} = 2$ M are compared to those in deionised water for mixing ratios of 1:1. While in deionised water particles almost remain stable, aggregation of PS particles is detected at elevated electrolyte concentration. The number of bound MF-RhB particles per PS particle, plotted as inset of Figure 5.14(a), slightly increases over the amount observed at low electrolyte concentration but remains too low to cause the

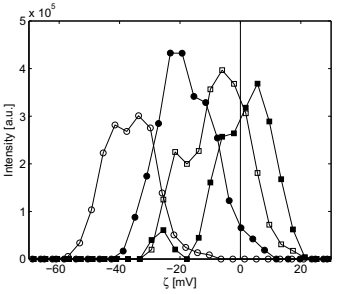

Figure 5.12: Measured ζ-potential distributions during aggregation at 2 min (○), 18 min (•), 58 min (□), 6 h (■) for constant $c_{PS} = 1.14 \cdot 10^4$ particles/μl, $c_{MF-RhB}/c_{PS} = 20:1$, $T = 298$ K, $c_M^{NaCl} = 0$ M, perikinetic.

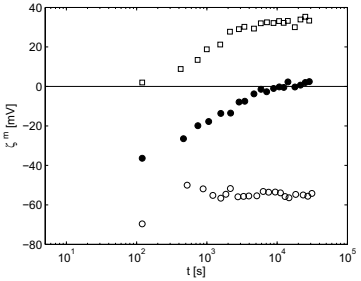

Figure 5.13: Evolution of average ζ-potential during aggregation showing destabilisation and charge reversal. Experimental conditions: MF-RhB to PS particle ratios of 1:1 (○), 20:1 (•) and 100:1 (□), $c_{PS} = 1.14 \cdot 10^4$ particles/μl, $T = 298$ K, $c_M^{NaCl} = 0$ M, perikinetic.

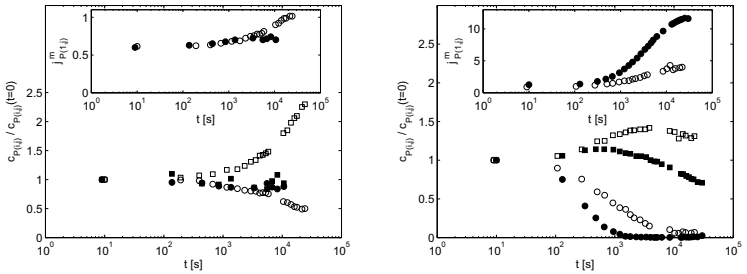

(a) Particle mixing ratio of 1:1. (b) Particle mixing ratio of 20:1.

Figure 5.14: Experimental particle heteroaggregation for different mixing ratios and ionic strengths: $c_M^{NaCl} = 0$ M (filled symbols, from Figure 5.2), 2 M (open symbols). PS primary particles (○), covered PS monomers (□), MF-RhB coverage of PS monomers (inset). $c_{PS} = 1.14 \cdot 10^4$ particles/μl, $T = 298$ K, perikinetic.

evident PS particle destabilisation. Thus, destabilisation at high electrolyte concentrations is achieved by a more effective shielding of surface charge electrolyte ions in the double layer and not by coverage with oppositely charged particles. This confirms expectations gained from theoretical aspects and previous experiments[113].

For an improved comparison of the destabilisation dynamics, the experiment was repeated at an intermediate mixing ratio of 20:1. At this mixing ratio, aggregation dynamics are greatly enhanced. The result is plotted in Figure 5.14(b) in comparison to that of deionised water shown before. At increased ionic strength, both primary and secondary heteroaggregation slow down. From the considerations in Chapter 2, we can expect a decreased stability between PS particles. However, this does not apply for the binding of MF-RhB particles to PS surfaces. As observed in the inset of Figure 5.14(b), primary heteroaggregation actually decelerates at elevated ionic strength. From this we can conclude, that the reduced electrostatic interaction increases the stability between MF-RhB and PS particles and more collisions during an encounter are necessary for the MF-RhB particle to adsorb onto the surface of a PS particle. This contrasts the usual findings in single species system and represents an unique effect in heteroaggregation. As a consequence, the onset of aggregation between clusters is postponed and the hold-up of covered PS monomers increases.

All in all, species independent aggregation under conditions of weak electrostatic interaction can be slower than species dependent heteroaggregation with a strong influence of electrostatic interaction energy if the stability between the different species is increased (instead of decreased) by elevated electrolyte concentration.

5.3.3 Variation of particle species

If the polystyrene particles from the company microParticles are exchanged by equally sized ones from Duke Scientific, different heteroaggregation behaviour can be detected. The aggregation dynamics for both binary particle mixtures are summarised in Figure 5.15. As can clearly be seen from the initial measurement, PS particles from microParticles show less uncovered and more covered PS monomers as well as a con-

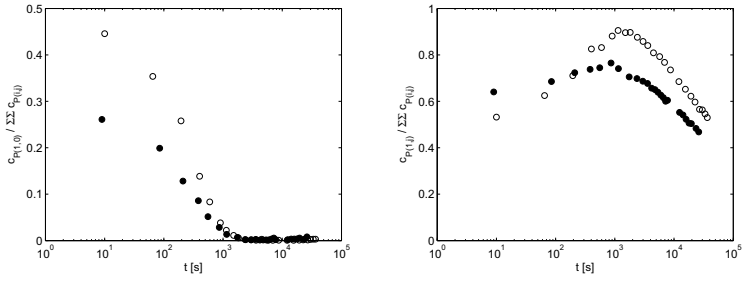

(a) PS primary particles.

(b) PS monomers covered with MF-RhB.

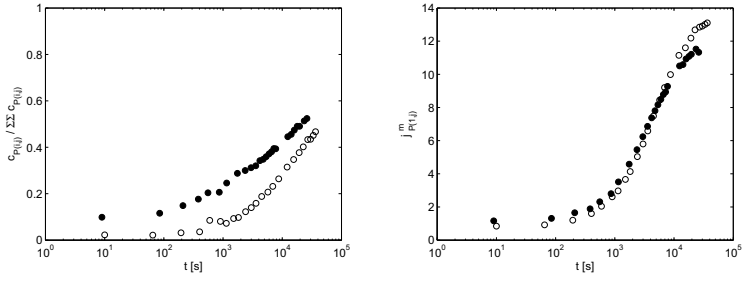

(c) PS oligomers.

(d) MF-RhB coverage of PS monomers.

Figure 5.15: Comparison of the experimental heteroaggregation dynamics of PS particles from microParticles (•, from Figure 5.2) and PS particles from Duke Scientific (○) with MF-RhB particles. Experiments were conducted at 20:1 mixing ratio, $T = 298$ K and $c_M^{NaCl} = 0$ M.

siderable extent of PS oligomers. Together with the lower ζ-potential value of Table 5.1 this indicates a lower stability against heteroaggregation.

The cause of deviating aggregation dynamics may be attributed to differences in the surface functionalisation applied by the two manufacturers to stabilise their particle standards against aggregation. This is already indicated by the different ζ-potentials and motivates further investigations by colloidal probe microscopy, which enables the measurement of interactions between two colloid particles as force-distance curves within arbitrary aqueous environments. Detailed insight into single particle interactions can help to explain different aggregation dynamics on the macroscopic population level. The measurement principle was already discussed in section 3.1.1 and although atomic force microscopy is well recognised in various scientific disciplines[73,111,155] colloidal probe measurements remain very challenging. Next to the preparation of the cantilever with monomer particles, the method development and sample handling during measurement including calibration issues of piezo elements and sensors represent intricate and cumbersome obstacles. This is why only preliminary conceptual findings that retain some level of incompleteness, rather than perfectly reliable and reproducible results, can be presented within the scope of this thesis.

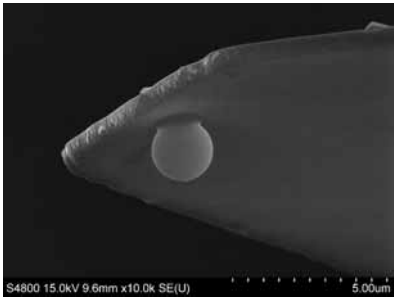

Figure 5.16: Electron micrograph of a tipless silicon nitride cantilever with a 2 μm PS particle attached as prepared for colloidal probe microscopy (Ultra-High resolution FE-SEM S-4800, Hitachi, Japan).

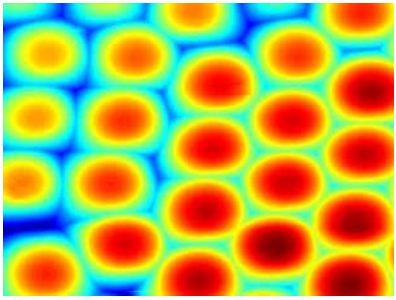

Figure 5.17: Topographic image of sintered PS substrate particles scanned in contact mode by a silicon nitride cantilever with tip for higher resolution.

5.3.3.1 Analysis of colloidal pair interactions

Single-particle interactions were studied with an Agilent 5500 Scanning Probe Microscope. Colloidal probe investigations require a careful preparation of cantilever and substrate. As illustrated in Figure 3.1, cantilever and substrate represent the anchor points for the two studied particles. Generally it would be feasible to measure the interaction of a cantilever particle against a flat substrate polymer layer and convert it into the desired geometry using Derjaguin's approximation of Eq. 2.14. However, the exact same surface characteristics of the commercial particle suspensions would hardly be achieved. Therefore, monolayers of substrate particles of each PS particle species were prepared on a clean glass slide. Before use in the AFM, they were sintered above the material glass temperature of roughly 100°C for 10 minutes until bridges between the particles formed. The particle bridges are necessary to increase the mechanical stability of the substrate layer against cantilever manipulation in contact mode.

Single PS particles were fixed to tipless cantilevers by a solvent-free polymer glue that dries in humid environments (Flex+bond, Weicon GmbH, Germany). A SEM image of a prepared cantilever is shown in Figure 5.16. The three axis water hydraulic micromanipulator enabled the handling of the cantilevers under a microscope. For all measurements, silicon nitride tipless cantilevers (NP-O, Veeco, USA) with a nominal spring constant of 0.58 N/m (range: 0.09-1.2 N/m) at a resonance frequency of 57 kHz (range: 40-75 kHz) were used. Since the spring constant is essential to convert the measured deflection into a force, it was determined for each cantilever with higher precision by a frequency resonance calibration in the course of every AFM measurement.

Colloidal probe microscopy was performed in a liquid cell with deionised water (MilliQ, Millipore, USA) as dielectric medium in correspondence with the continuous phase in the macroscopic aggregation experiments. Prior to the determination of the apex-to-apex interactions, a topographic image was obtained for orientational purposes. A representative topography of a sintered PS particle layer is shown in Figure 5.17. Since imaging might affect the particle surface characteristics, the topography was obtained at very low contact pressures. With special cantilevers the topographic

imaging can also be performed in tapping mode, reducing the full contact between the particle surfaces to multiple soft contacts. This might further reduce the effects of material friction on the particle surface characteristics[111].

Once an apex of a substrate particle is localised, force-distance curves are obtained in the closed-loop mode. The closed-loop mode ensures that during repetitive measurements the exact same lateral position is maintained by a feedback control. Force-distance curves are obtained from an average of 20 automatically executed scans at the same position. After completing the scans, the cantilever was retracted from the surface and the spring constant was determined using an automated procedure provided by the AFM software. Finally the cantilever was demounted and visualised under the microscope to asses the condition of the colloid particle regarding contamination and slip. Many cantilever particles showed crystalline contaminations or additional particles from the substrate. Slip or even the complete loss of the glued on particle was also detected. These measurements were not considered for analysis.

In total three interactions were investigated: PS particles from Duke Scientific and from microParticles against sintered layers of identical substrate particles or of MF-RhB particles. Figures 5.18(a)-5.18(c) show representative results of a single scan for PS particles from Duke Scientific. The raw approach signal of the photodetector against the height of the vertical piezo translator in Figure 5.18(a) is transformed into the force distance curve shown in Figure 5.18(b) by the procedure explained in section 3.1.1. From this the interaction potential is obtained by integration in Figure 5.18(c). The integration is terminated at the jump-in point. Figure 5.18(d) finally compares the interactions between different materials averaged over the repetitive scans with DLVO predictions.

From the average curves in Figure 5.18(d) we observe that the measured interactions considerably exceed the thermal energy $k_B T$ over the whole scan. For the strong repulsive interactions from DLVO theory between PS particles in deionised water, a smaller separation distance for the jump-in would be expected. This can be achieved by choosing softer cantilevers in terms of spring constant. However, for attractive interactions they might cause an even earlier jump-in. The interactions between all three materials raise some ambiguities. While the interactions for PS particles from Duke Scientific clearly dominate over those between PS monomers from microParticles, confirming expectations from the ζ-potentials and the aggregation dynamics, the interactions between PS and MF-RhB particles range in between. Instead of an attractive interaction of oppositely charged particles, a repulsive interaction exceeding that between PS monomers of microParticle is observed. The comparison to theoretical predictions from DLVO theory in Figure 5.18(d) reveals further mismatches. Experimental interactions tend to be much stronger than the predicted ones. To some extent the deviations can be attributed to an overestimation of the cantilever spring constant that essentially scales the calculated force. The determination of the spring-constant is subject to experimental error that cannot easily be quantified. Any error in spring constant would severely affect the integrated potential but could hardly explain all inconsistencies. The strong deviations suggest that the measurements do not portray the colloidal interactions that exist in the original suspensions. The primary cause of the deviation could however not be ascertained within the scope of this thesis. Considering that colloidal probe microscopy was successfully applied previously to quantify single particle interactions[12,27,111], it presents a suitable platform for follow-up investigations.

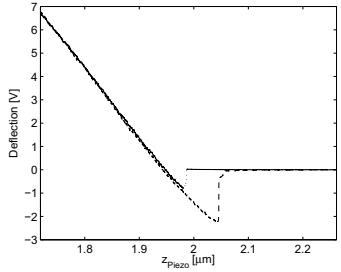

(a) Raw data of cantilever approach (−) and retraction (−−) with zero deflection as baseline. The slope of the linear contact part expresses the deflection sensitivity.

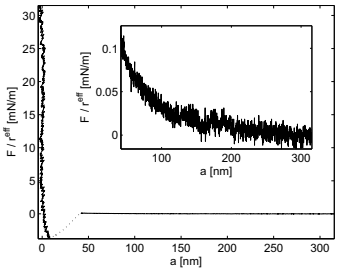

(b) Relative force distance curve of cantilever approach with $r^{eff} = r_{p\prime} r_{p\prime\prime} / (r_{p\prime} + r_{p\prime\prime})$.

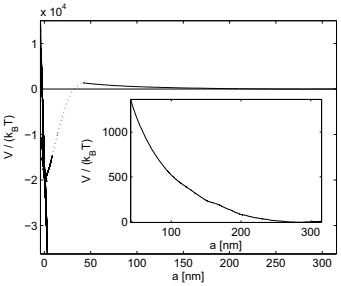

(c) Interaction potential of cantilever approach. All values following the jump-in are of inferior physical relevance.

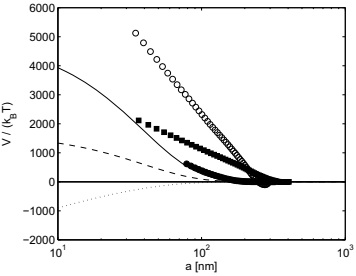

(d) Comparison of measured interaction potentials to DLVO predictions.

Figure 5.18: Colloidal interaction potentials from force distance measurement by colloidal probe microscopy. Figures (a)-(c) show the results for a single representative closed loop scan between PS particles from microParticles. Dotted lines indicate the jump-in interval and the insets in Figures (b) and (c) zoom the data prior to jump-in. Figure 5.18(d) shows a comparison of measured interaction potentials to DLVO predictions (lines) between PS particles from Duke Scientific (○, ——), from microParticles (●, – –) and between PS and MF-RhB particles from microParticles (■, · · ·). Each measurement is averaged over 20 scans.

Some fundamental concerns regarding the conservation of the surface functionalisation are raised by the preparation of the cantilever and substrate particles. Especially the drying and sintering steps probably exert a considerable influence on the chemical stability of the polymer latices. Additional uncertainties might be introduced by the mechanical stability of the approaching particles against increasing surface interactions. This would include any deformation of the glue during the repetitive switching between contact and non-contact. Indeed, processing effects on the surface functionalisation with influences on colloidal stability have been reported before and were harnessed to prepare stacks of colloidal monolayers[118]. The problem could be tackled by similar measurements with particles obtained from dry powders. However, this might then hamper the macroscopic aggregation experiments through inexact particle concentrations. In consequence, a unique relation of deviating macroscale aggregation dynamics to microscale colloidal interactions is not guaranteed either. A realistic measure to reduce the material friction during contact is

posed by the use of tapping mode for the topographic imaging. This would require different cantilevers. Finally, comparison to results by different measurement techniques, like holographic methods that arrest colloidal particles in optical traps[49,50,76], might present a further route to identify sources of error in future.

5.4 Aggregation dynamics in ternary particle systems

Aggregation dynamics in ternary particle mixtures are subject to the same modes of influence that apply for binary systems. Apart from the encounter frequency and the sticking efficiency, the rate at which heteroaggregates are formed depends on the particle concentrations. With increasing particle concentration, successful collision events become more probable.

Experiments in ternary systems of 2 μm PS and MF-RhB particles with 530 nm MF-FITC particles were conducted to show that flow cytometry enables a multiscale analysis of the cluster composition and to establish an experimental method to detect preferential aggregation in particle systems. In the ternary systems preferential aggregation is facilitated by specific particle interactions. Apart from differences in size, the particles also vary with respect to their surface potentials, which gives rise to similar electrostatic effects as encountered in the previous section. The particle properties are summarised in Table 5.1. Because both MF particle species are positively charged their aggregation is not likely. In contrast, aggregation with PS particles is favoured, and MF-FITC and MF-RhB particles competitively bind to the PS surfaces. Since the diffusive motion of larger MF-RhB particles is slower than that of small MF-FITC particles, PS surfaces are preferentially covered by MF-FITC rather than MF-RhB particles. This effect is intensified by choosing elevated MF-FITC concentrations, as shown below. In this system, mixed aggregates of all three species could be detected. Electron micrographs of ternary heteroaggregates are shown in Figure 5.19.

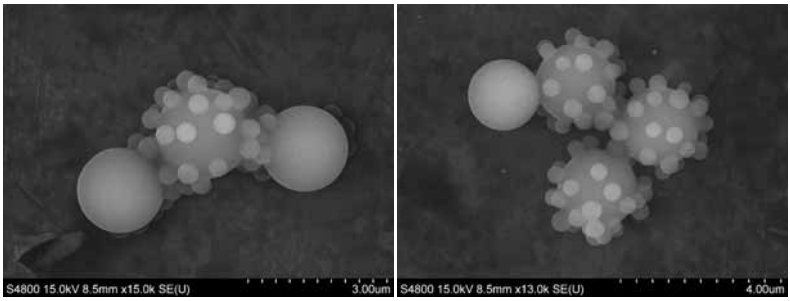

Figure 5.19: Electron micrographs of complex ternary heteroaggregates composed of large PS particles, which are covered with many small MF-FITC particles, and uncovered large MF-RhB particles. To arrest the morphology of the cluster for vacuum conditions, the aggregates were autoclaved at the glass temperature of polystyrene. This did not have direct influence on the aggregate morphology as was validated by means of fluorescence and laser scanning microscopy (data not shown).

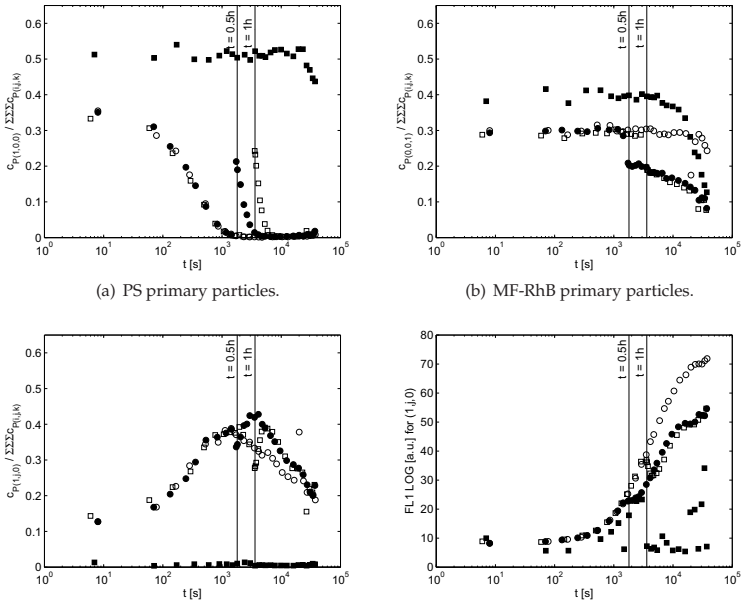

(a) PS primary particles.

(b) MF-RhB primary particles.

(c) MF-FITC covered PS monomers.

(d) $FL1$ intensity by MF-FITC coverage on PS monomers.

Figure 5.20: Experimental heteroaggregation dynamics in a ternary particle system for $c_{PS}/c_{MF-FITC}/c_{MF-RhB}$ = 1:1:1 (■) and 1:20:1 (○) without particle addition as well as 1:20:1 with PS primary particle dosage at t = 30 min (•) and 1 h (□) expressed by particle concentration fractions and fluorescence intensity.

To demonstrate the effect of different concentration ratios in ternary systems, the aggregation dynamics of systems with $c_{PS}/c_{MF-FITC}/c_{MF-RhB}$ = 1:20:1 and 1:1:1 ratios were studied. Results for selected aggregate populations are illustrated in Figure 5.20. For both ratios, the aggregation dynamics differ. In the 1:1:1 system the fractions of PS primary particles (1,0,0) in Figure 5.20(a) and MF-RhB primary particles (0,0,1) in Figure 5.20(b) remain constant within the first hour of the experiment. During this time, the number of MF-FITC particles covering the surface of a nearly constant PS monomer fraction (1,j,0) first increases, as expressed by the $FL1$ signal in Figure 5.20(d). After approximately 1 h it suddenly drops back to the initial autofluorescence values. The sudden decrease of MF-FITC coverage correlates with the formation of mixed heteroaggregates (1,j,1) (data not shown) and only few PS particles of lower surface coverage remain in the (1,j,0) region. This is also responsible for the higher $FL1$ signal variabilities observed towards the end of the experiment.

While in the 1:1:1 system noticeable effects only occur towards the end of the experiment, the 1:20:1 system features faster, more complex aggregation behaviour. Similar to the aggregation dynamics in binary particle systems, the fraction of PS primary particles sigmoidally decreases in Figure 5.20(a), while that of MF-RhB particles remains essentially unchanged in Figure 5.20(b). This coincides with the increase of covered PS monomers (1,j,0) (Figure 5.20(c)). At this mixing ratio, collisions of PS

particles with MF-FITC particles become more probable than collisions with MF-RhB particles, and PS surfaces are covered with several smaller MF-FITC particles rather than with competing MF-RhB particles. This is expressed by rising fluorescence intensities in Figure 5.20(d) at constant MF-RhB fractions of Figure 5.20(b).

The formation of more complex clusters by bridging of oppositely charged surface patches, that was already observed for binary systems, is indicated by the decreasing fraction of covered PS monomers (1,*j*,0). Hence, in Figure 5.3(b) clusters appear in regions like (2,*j*,0), (i>1,*j*,1), (1,*j*,2), etc..

5.4.1 Dosage experiments

For a possible application of flow cytometry to guide technical processes, the sensitivity against intermittent particle dosage was studied. Two experiments representatively focus on the addition of PS particles after 30 min and 1 h after start. The results of both dosage experiments in a 1:20:1 system are included in Figure 5.20. The sudden increase of PS primary particles following dosage is clearly visible in Figure 5.20(a). Due to the change in total particle number effects are also visible in Figures 5.20(b)-(d). Generally, in all plots the particle fractions show similar trends as the reference system without additional dosage. Clusters containing PS particles asymptotically approach the reference towards the end of the experiment, while in all aggregates without PS particles the step deviations from the reference system persist. This is caused by an increase of $\sum\sum\sum c_{P(i,j,k)}$ upon addition of PS monomers.

From Figures 5.20(c) and (d) we can deduce that the additional PS particles are quickly covered by the remaining MF-FITC particles. Similar to the aggregation dynamics in the 20:1 binary particle system, a deceleration of the aggregation dynamics is observed in Figure 5.20(d). This figure also shows that the average MF-FITC coverage remains below the reference experiment without dosage, since a constant number of MF-FITC particles is distributed among an increased number of PS particles. Aggregation is thus limited by depletion of free MF-FITC particles before the maximum coverage of all PS particles was reached.

5.5 Summary

In the presented studies central heteroaggregation phenomena in binary and ternary particle mixtures in well defined environments were investigated. The dynamic evolution of the multi-dimensional cluster composition was successfully tracked with flow cytometry. The particle species within an aggregate were identified either by size or by distinct fluorescent markers. Due to different size and material properties of the particle populations, complex clusters were formed in a two-step heteroaggregation process. By primary heteroaggregation the surfaces of large particles were covered by oppositely charged small particles of different species. Thereby surface heterogeneities are generated which induce bridging effects enabling the onset of cluster-cluster heteroaggregation (secondary heteroaggregation). The influences of important process parameters on particle encounter frequency and efficiency were studied. Expected results were confirmed for variations in concentration, temperature and hydrodynamics conditions. Further investigations focused on the predominant

electrostatic de- and restabilisation phenomena which are strongly affected by the particle mixing ratio and the ionic strength of the dispersion medium. It was shown that different aggregation regimes can be attained by the macroscopic particle mixing ratio and that elevated electrolyte concentrations can actually increase the stability between oppositely charged particle species. In addition, colloidal probe microscopy was tested as a tool for assessing the pairwise potential interaction energies. Experiments in ternary particle systems pave the way towards a higher dimensional analysis of multi-species aggregation. Furthermore, dosage experiments demonstrated the high sensitivity of flow cytometric measurements emphasising their versatile applicability.

Although flow cytometry allows a very detailed detection of aggregation processes in multi-dimensional particle systems unmatched by other techniques, the precise distinction of cluster composition at high signal intensities and the calibration of fluorescence intensity signals remain challenging. Furthermore, the aggregate morphology resolving the local distribution of the constituent particles within the cluster eluded flow cytometric detection. Structural analysis has only recently been addressed in flow cytometers that are equipped with a high speed camera that generates snapshots of the passing particles.

Chapter 6

Population balance simulation of binary heteroaggregation

In this chapter the experimental data for binary particle systems are theoretically reconstructed in order to simulate the predominant electrostatic effects. A population balance model is set up to simulate the dynamic evolution of the cluster composition. The employed aggregation rates (kernels) are based on classical models incorporating foundations of colloid science. The basic structure of these deterministic models date back to the seminal works of von Smoluchowski[152] and Fuchs[37]. The aggregation rates used as kernels in the population balance model are developed in section 6.1 under consideration of the foundations presented in Chapter 2. This is followed by defining and reducing a population balance equation on a bivariate discrete property state space in section 6.2 referring to theoretical foundations of Chapter 4. The numerical solution of the model equations and a comparison to the experimental data of Chapter 5 are presented in section 6.3.

6.1 Aggregation kernel

The aggregation rate of two particles P' and P'' forming a product particle P is represented by $\omega_{P',P''}$. As already mentioned in the previous chapter, it depends on two central factors of influence. The aggregation rate represents a transfer frequency between the different aggregation states, thus accounting for the the number of particle encounters and the associated probability of successful aggregation. Therefore it follows from the product of encounter frequency $\omega^F_{P',P''}$ and its efficiency $\omega^E_{P',P''}$[128]:

$$\omega_{P',P''} = \omega^F_{P',P''} \cdot \omega^E_{P',P''} \,. \tag{6.1}$$

Whether a bond between two particles or clusters is successfully established during an encounter depends on particle geometry, direction of approach, number of collisions per encounter as well as on the stability ratio W. The stability ratio introduces the influence of interaction pair potentials. If the potential interaction is purely attractive, a diffusion limited cluster aggregation (DLCA) regime is present with $W = 1$, if the potential contains an intermediate repulsive barrier as in Figure 2.3 aggregation is reaction limited (RLCA) with $W \gg 1$.

While the encounter frequency in perikinetic systems is generally agreed upon in literature, a multitude of modelling approaches were published for the encounter efficiency, usually referred to as sticking efficiency, over the past years[4,32,37,60,98,101,102,103].

In the following sections 6.1.1 and 6.1.2 suitable literature models for the calculation of encounter frequencies and efficiencies are introduced. Cases where modifications had to be made in order to represent the dependency of aggregation rates from multi-species cluster composition are explicitly mentioned. Additionally, a new approximate kernel concept based on a charge balance is presented.

6.1.1 Encounter frequency

The kernel describing the frequency of particle encounters in perikinetic (i.e. diffusive) systems accounts for stochastic Brownian particle motion. It was first formulated by von Smoluchowski[152] in 1917. From a mass balance around a totally absorbing particle P' the flux of another particle P'' through a surrounding sphere with collision radius $R_{P',P''} = r_{P'} + r_{P''}$ can be derived. This approach was later applied in a similar fashion by Fuchs[37]. He included a superimposed force field into the balance equation to consider additional particle drift beyond diffusion and thus derived the stability ratio W. The solution of the mass balance without superimposed force fields at conditions of $t \gg R^2/D$ yields an aggregation rate of $4\pi D_{P',P''} R_{P',P''}$ with $D_{P',P''} = D_{P'} + D_{P''}$ as combined diffusion coefficient of the two particles towards each other[152]. Following the argumentation of von Smoluchowski[152], we assume spherical morphologies for all multimeric clusters and apply the concept of fractal geometries (section 2.4). We then obtain

$$\omega^F_{P',P''} = 4\pi \left(D_{P'} + D_{P''}\right) \left(r^G_{P'} + r^G_{P''}\right) , \tag{6.2}$$

which is until today a generally accepted expression to describe diffusion limited aggregation[131]. The diffusion coefficient of a sphere can be replaced by the Stokes-Einstein relation $D_P = k_B T / \left(6\pi\eta r^G_P\right)$ with $k_B T$ as thermal energy and η as dynamic solvent viscosity[131], yielding

$$\omega^F_{P',P''} = \frac{2k_B T}{3\eta} \cdot \left(\frac{1}{r^G_{P'}} + \frac{1}{r^G_{P''}}\right) \left(r^G_{P'} + r^G_{P''}\right) . \tag{6.3}$$

From section 2.4 we can now also substitute the radii of gyration by Eq. (2.28) with $d_f = [1, \ldots, 3] \in \mathbb{R}$ as fractal dimension, ν_P as dimensionless aggregate volume and $k_f \approx 1$. The aggregation kernel then follows as

$$\omega^F_{P',P''} = \frac{8k_B T}{3\eta} \cdot \frac{1}{4} \left(\nu_{P'}^{-\frac{1}{d_f}} + \nu_{P''}^{-\frac{1}{d_f}}\right) \left(\nu_{P'}^{\frac{1}{d_f}} + \nu_{P''}^{\frac{1}{d_f}}\right) . \tag{6.4}$$

In this equation, the first fraction is sometimes referred to as Smoluchowski kernel for Brownian motion ω^B, while the rest represents a size correction kernel $\omega^r_{P',P''}$. The prefactor of $1/4$ is explicitly maintained, since it guarantees unity of $\omega^r_{P',P''}$ for the case of equally sized spheres. Although only small aggregates of up to $i = 5$ PS particles could be clearly distinguished in the experiments[119] and therefore justify a certain skepticism in the application of the fractal geometries, this concept provides a convenient method to describe aggregate geometry in a compact manner.

While the aggregation of MF-RhB and PS monomers in primary heteroaggregation is considered to be diffusion limited with $d_f = 1.8$, secondary heteroaggregation between heteroaggregate clusters is generally reaction limited with $d_f = 2.1$. How-

ever, a parameter study concerning the influence of the fractal dimension d_f on the aggregation dynamics in section 6.3 clearly shows that the influence of the fractal dimension is not very pronounced.

6.1.2 Sticking efficiency

The second factor contributing to the aggregation kernel is the probability that two particles form a stable bond during an encounter. In the DLCA regime, colliding particles aggregate spontaneously upon contact. Under the assumption that the particle motion cannot be enhanced by attractive interaction potentials, this regime represents the maximum aggregation frequency. In contrast, not every collision results in the formation of a new aggregate in RLCA and the encounter frequency is retarded by an efficiency factor $\omega^E_{P',P''}$. For single species systems von Smoluchowski[152] introduced an efficiency factor to limit the number of successful encounters in slow or rate limited coagulation processes. A consistent model for the efficiency was found by Fuchs[37] and presents an important basis of most kernel models today. His stability ratio W describes the influence of superimposed force fields on particle homoaggregation dynamics. As we recall from section 2.3.1, it is defined as the ratio of a flux for purely diffusive particle motion at infinite dilution to the diffusion with additional particle drift. The reciprocal of the stability ratio presents a very useful measure for the sticking efficiency, since repulsive interaction potentials raise the stability ratio beyond unity.

In his original publication, Fuchs[37] used $a_{min} = 0$ and $a_{max} = \infty$ as analytically exact integration boundaries. For a numerical solution of the integral these boundaries were replaced by $a_{min} = 4$ Å and $a_{max} = 1$ μm. The lower boundary now considers a layer of ions or water molecules bound to each particle surface, preventing further approach[68]. The upper boundary is determined under consideration of the superimposed force field; when using values beyond 1 μm the stability ratio does not change considerably. The superimposed force field is expressed as an interaction potential energy $V_{P',P''}(a)$. According to classical DLVO theory[23,151] van der Waals $V^{vdW}_{P',P''}$ and electrostatic $V^{el}_{P',P''}$ energies represent the main contributions at greater separation distances in particle systems (Figure 2.1). To account for atomic repulsion at very small separation distances, the Born potential is considered as well. The parameters used in the interaction potentials are summarised in Table 6.1.

Table 6.1: Parameters used in calculations of potential interaction energies. The same parameter set was used for both kernel concepts.

Potential energy	Parameter	Value	Unit	Reference
$V^{Born}_{P',P''}(a)$	b	12	-	Feke et al.[33]
	r_σ	4	Å	Feke et al.[33]
$V^{vdW}_{P',P''}(a)$	A_{PS-H_2O-PS}	$1.0 \cdot 10^{-20}$	J	Israelachvili[68]
	A_{PS-H_2O-MF}	$2.2 \cdot 10^{-20}$	J	[a]
$V^{el}_{P',P''}(a)$	ε_r	80	-	Israelachvili[68]
	ζ_i	$[-48, +43]$	mV	[b]

[a] calculated from Lifschitz theory Eq. (2.16)
[b] determined with Zetasizer Nano ZS (Malvern, UK)

An early approach to model colloidal stability in multi-species suspensions was published by Hogg et al.[60] in 1966. For aggregation between particles of population A and B an overall sticking efficiency was defined as the geometrical sum over all three types of possible interactions (A-A, A-B and B-B) weighted by their respective number fractions. In this thesis, binary heteroaggregation was simulated using two different kernel concepts in comparison. A first simple model directly applies the stability ratio to predict the efficiency of particle encounters. Here, the stability ratio varies with changing cluster composition and thus couples the aggregation rates to the state space of the population balance equation. Considering all parameters displayed in Eq. (2.24), it may be assumed that in electrostatically dominated aggregation the most important parameter variation occurs for the cluster surface potential. Hence, an average potential for each cluster composition was determined by a mean field type charge balance, as discussed in section 6.1.2.1. In a second approach, the model of Moncho-Jordá et al.[98] was used to describe inhomogeneous cluster surfaces (section 6.1.2.2). Similar to the approach by Hogg et al.[60], the interactions between two clusters are determined from interactions of the pure substances, weighted with their respective fraction of surface coverage. In a binary system the cluster surface is thus divided into two characteristic surface patches, and the kernel depends on changing surface fractions rather than changing interaction potentials. In contrast to the rather crude charge-balance approach, which predominantly depends on a single parameter, the patchy-particle model captures compositional cluster variations by two (coupled) cluster properties. Both kernel concepts are schematically illustrated in Figure 6.1.

6.1.2.1 Pseudo-homogeneous surface model

In the charge-balance kernel each encounter comprises a single collision event with an efficiency given by the stability ratio $W_{P',P''}$ between two clusters $P'\,(i',j')$ and $P''\,(i'',j'')$:

$$\omega^{E}_{P',P''} = \frac{1}{W_{P',P''}}\,. \tag{6.5}$$

The dependency of cluster composition is introduced by the radius of gyration, the hydrodynamic correction term $B_{P',P''}$ of section 2.3.1.1 as well as by parameters of the interaction potential $V_{P',P''}$, such as the Hamaker constant $A_{P',P''}$ and the surface potentials $\Psi^{0}_{P'}$ and $\Psi^{0}_{P''}$ of each cluster. In the investigated particle mixture the strong variation over cluster composition is primarily caused by the changing cluster surface potentials which define the electrostatic interaction. While the surface potentials of the monomeric particles are approximated by their ζ-potentials, the surface potential of complex clusters can be determined from a spherical substitute particle constructed such that it corresponds in size and charge (Figure 6.1). An analytical expression for the cluster surface potential is gained from the solution of Poisson's equation for spherical clusters of radius r^{G}_{P} surrounded by an isotropic dielectric medium. With the boundary conditions of $\Psi(r \to \infty) = 0$ and a charge density of $\rho^{C}_{P} = 3Q_P / \left(4\pi \left(r^{G}_{P}\right)^3\right)$ we obtain the surface potential as

$$\Psi_{el}(r = r^{G}_{P}) = \frac{Q_P}{4\pi\varepsilon_o\varepsilon_r r^{G}_{P}} = \frac{Q_P}{C_P} \tag{6.6}$$

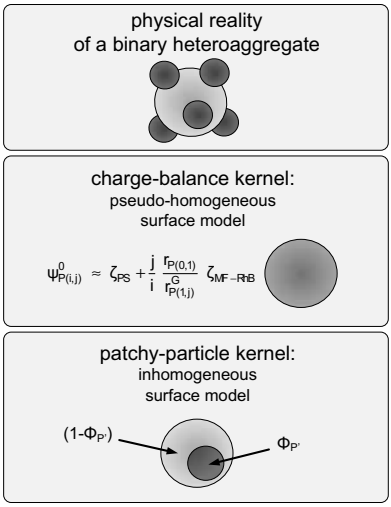

Figure 6.1: Schematic illustration of the charge-balance and patchy-particle kernel concepts.

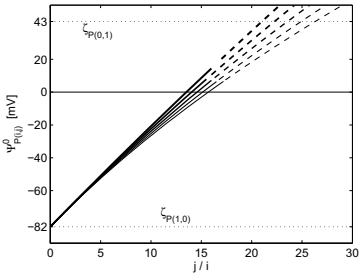

Figure 6.2: Surface potential $\Psi^0_{P(i,j)}$ dependence on the average MF-RhB coverage j/i. Line thickness decreases with increasing number of aggregate PS particles ($i = 1,\ldots,5 \in \mathbb{N}$). With increasing coverage the surface potential increases until restabilisation is reached. The extrapolated surface potential for already restabilised particles is indicated by dashed lines.

in which Q_P represents the cluster charge and C_P the capacitance. For two approaching clusters each comprising several PS particles, the aggregation behaviour predominantly depends on the interactions at the point of closest approach. Therefore, the charge of an aggregate can be replaced by the charge of the closest pair of PS particles each with an average coverage of j/i. Any other interactions between other particles of each cluster are neglected. The average charge of the PS particle with closest approach is given by

$$Q_{P(i,j)} = Q_{P(1,0)} + \frac{j}{i}\, Q_{P(0,1)} \tag{6.7}$$

with $Q_{P(1,0)}$ and $Q_{P(0,1)}$ as charge of the monomer particles. From Eqs. 6.6 and 6.7 we obtain the following surface potential

$$\begin{aligned} \Psi^0_{P(i,j)} &= \Psi^0_{P(1,0)} + \frac{j}{i}\frac{r_{P(0,1)}}{r^G_{P(1,j)}}\Psi^0_{P(0,1)} \\ &\approx \zeta_{PS} + \frac{j}{i}\frac{r_{P(0,1)}}{r^G_{P(1,j)}}\zeta_{MF-RhB} \end{aligned} \tag{6.8}$$

in which the particle surface potentials were replaced by the respective ζ-potentials. The variation of the surface potential as function of the average specific MF-RhB particle coverage j/i is shown in Figure 6.2. Although the amount of MF-RhB particles is not limited by definition, unphysically high average charge is kinetically prevented by restabilisation.

An attempt was made to introduce a fitting parameter into Eq. 6.8 to enable an adaptation to flow cytometric data if applicable. One possibility is presented by the implementation of a constant $\mathcal{C}$ into the surface potential approximation:

$$\Psi^0_{P(i,j)} \approx \zeta_{PS} + \mathcal{C}\frac{j}{i}\frac{r_{P(0,1)}}{r^G_{P(1,j)}}\zeta_{MF-RhB}\,. \tag{6.9}$$

For $\mathcal{C} > 1$ an overproportional charge neutralisation effect by MF-RhB adsorption is achieved. This decreases the maximum number of MF-RhB particles that can adsorb to PS particles. For $\mathcal{C} < 1$ the opposite is expected, resulting in a delayed onset of secondary heteroaggregation.

All in all, the charge-balance model only provides a crude approach to determine the electrostatic effects that are responsible for primary and secondary heteroaggregation. Anyhow, simulation results agree surprisingly well with experimental data as shown in section 6.3. More exact predictions can be obtained by applying different solution methods that consider the aggregate geometry in detail, like Brownian dynamics methods (section 4.3), or by introducing surface heterogeneity into a kernel for population balance equations. In the following section the literature model for patchy-particles is briefly summarised.

6.1.2.2 Inhomogeneous surface model

A different model approach for the sticking efficiency was presented by Moncho-Jordá et al.[98] in 2003 based on earlier work concerning time series probabilities[101]. It discriminates between surface inhomogeneities and lumps all parts of the cluster surface which constitute similar aggregation behaviour into representative surface patches. The surface fraction of each patch is then used as weighting factor in the calculation of a total sticking efficiency from the interactions of the pure materials. This method provides a convenient description of bridging coagulation and is thus well suited to describe heteroaggregation in binary particle systems. The sticking efficiency is given by[98]

$$\omega^E_{P',P''} = \frac{P_{P',P''}(\phi)}{1-\left[1-P_{P',P''}(\phi)\right]\ P^c_{P',P''}} \tag{6.10}$$

and accounts for two physical effects: first, the probability $P_{P',P''}(\phi)$ with which two surface patches come into contact during a collision, i.e. PS-PS, PS-MF, MF-MF, and second, the probability $P^c_{P',P''}$ of multiple collisions per encounter. The probabilities are given in Eq. (6.11) and (6.12) adapted to the case of binary heteroaggregation, with $\phi_{P(i,j)}$ as surface fraction, N_{11} as average number of collisions per successful encounter and α as scaling factor. From the original publication we obtain $N_{11} = 6.1$ and $\alpha = 0.35$[98].

$$\begin{aligned} P_{P',P''}(\phi) &= \frac{(1-\phi_{P'})(1-\phi_{P''})}{W_{P(1,0),P(1,0)}} + \frac{\phi_{P'}(1-\phi_{P''}) + (1-\phi_{P'})\phi_{P''}}{W_{P(1,0),P(0,1)}} + \frac{\phi_{P'}\phi_{P''}}{W_{P(0,1),P(0,1)}} \\ &\approx \phi_{P'}(1-\phi_{P''}) + (1-\phi_{P'})\phi_{P''} \end{aligned} \tag{6.11}$$

$$P^c_{P',P''} = 1 - \frac{1}{N_{11}\left(\nu_{P'}\nu_{P''}\right)^{\alpha}} \tag{6.12}$$

At very low ionic strength, particles with equal charge remain stable, yielding stability ratios of $W_{P(1,0),P(1,0)} \approx W_{P(0,1),P(0,1)} \to \infty$. Furthermore, since the particle species are oppositely charged, heteroaggregation is diffusion limited with $W_{P(1,0),P(0,1)} = 1$. Under these circumstances, $P_{P',P''}$ reduces to the approximate expression shown in Eq. (6.11) and the aggregation rate merely depends on the surface fractions $\phi_{P'}$ and $(1 - \phi_{P'})$ as well as $\phi_{P''}$ and $(1 - \phi_{P'})$ of the colliding particles. They are limited to $0 \leq \phi \leq 1$.

The surface fraction $\phi_{P(i,j)}$ for the single representative MF-RhB patch on the PS surface is determined from the ratio of the total cross-sectional area of the mean adsorbed number of MF-RhB particles j/i to the surface area of a single spherical PS monomer

$$\phi_{P(i,j)} = \min\left\{1, \frac{\frac{j}{i}\pi r_{eff}^2}{4\pi R^2}\right\} = \min\left\{1, \frac{j}{4i}\frac{\gamma^2}{\left(\frac{r_{1,0}}{r_{0,1}}\right)^2 + 2\frac{r_{1,0}}{r_{0,1}}}\right\} \tag{6.13}$$

where $R = r_{1,0}^2 + 2r_{1,0}r_{0,1}$ is gained from geometric considerations as the radius from the centre of the PS particle to the point of intersection between the adsorbed MF-RhB particles. In order to fit experimental data, the maximum number of adsorbed particles has to be reduced by means of an effective radius $r_{eff} = \gamma r_{0,1}$ with $\gamma \geq 1$. This introduces an excluded surface area, which could be caused for instance by an electrostatic repulsion between neighbouring MF-RhB particles adsorbed on the PS surface.

Kernel modifications due to reorientation effects caused by multiple contacts during each encounter are neglected here and aggregation dynamics are thus prone to a slight overestimation[98]. A lower bound can easily be generated with $P^c_{P',P''} = 0$. In the original publication, the kernel is limited in use to the dimer formation rate and does not consider rotation of the clusters and shielding effects, as investigated in Olsen et al.[102,103]. The presented kernel model is not restricted in use to the PS dimer formation rate, for which the single patch model would be exact. But since PS dimer formation is the most dominant mechanism in PS oligomer formation within the investigated time span, any error induced by this extension is assumed to be negligible.

6.2 Population balance model

Both kernel concepts are introduced into a population balance model. The simulation framework is based on the theoretical considerations of Chapter 4. In order to formulate a population balance equation, the constituting property state space is developed in section 6.2.1 and reduced from its full extent by by neglecting physically irrelevant aggregation states in section 6.2.2. On this basis the population balance equation is defined in section 6.2.3 with respect to two internal coordinates describing the cluster composition. In our approach any differences regarding morphological issues are neglected, so that for instance aggregates like  or  or  are assumed to act identically and can therefore be lumped into a single representative state space coordinate.

6.2.1 Definition of state space

Since the orientation of the particles in each aggregate is arbitrary, the complete property space $\mathcal{P}$ is spanned by the absolute particle numbers which constitute the cluster. For the binary particle mixtures investigated in Chapter 5, a two-dimensional property space is spanned by i and j, which denote the number of PS and MF-RhB particles per aggregate, respectively. Since these numbers are physically discrete, property space and the population balance equation are both formulated discrete with respect to the internal coordinates. The aggregate number concentrations $c_{i,j}$ for each property state are stored in a matrix $\underline{c}$. It is shown in Eq. (6.14) and illustrates the full state space with $i \in [0, \ldots, i^{max}]$ and $j \in [0, \ldots, j^{max}]$.

$$\underline{c} = \begin{pmatrix} & \text{j} & & & & & \\ \text{i} & c_{0,1} & c_{0,2} & c_{0,3} & \cdots & c_{0,j^{max}} \\ c_{1,0} & c_{1,1} & c_{1,2} & c_{1,3} & \cdots & c_{1,j^{max}} \\ c_{2,0} & c_{2,1} & c_{2,2} & c_{2,3} & \cdots & c_{2,j^{max}} \\ c_{3,0} & c_{3,1} & c_{3,2} & c_{3,3} & \cdots & c_{3,j^{max}} \\ \vdots & \vdots & \vdots & \vdots & \ddots & \vdots \\ c_{i^{max},0} & c_{i^{max},1} & c_{i^{max},2} & c_{i^{max},3} & \cdots & c_{i^{max},j^{max}} \end{pmatrix} \tag{6.14}$$

The maximum number of PS particles per aggregate is denoted by i^{max}, the maximum amount of MF-RhB particles by j^{max}. For an unreduced system, i^{max} and j^{max} correspond to the total amount of particles within the liquid volume and can reach very high numbers. However, most of the resulting property coordinates are physically irrelevant and can be neglected. This motivates model reduction strategies to accelerate numerical solutions, as explained in section 6.2.2.

For improved mathematical handling, the matrix $\underline{c}$ over all of property space is transformed into a concentration vector $\vec{c}$ by concatenating the rows. The concentration vector is shown in Eq. (6.15), along with the composition vectors $\vec{i}$ and $\vec{j}$, which contain the amount of PS and MF-RhB particles per aggregate for each property state.

$$\begin{aligned} \vec{c} &= \left(c_{P(0,0)} \ldots c_{P(0,j^{max})} \; c_{P(1,0)} \ldots c_{P(1,j^{max})} \ldots c_{P(i,j)} \ldots c_{P(i^{max},j^{max})} \right) \in \mathbb{R}^{P^{max}} \\ \vec{i} &= \left(0 \ \ldots \ 0 \quad 1 \ \ldots \ 1 \ \ldots \ i \ \ldots \ i^{max} \right) \in \mathbb{N}_0^{P^{max}} \\ \vec{j} &= \left(0 \ \ldots \ j^{max} \quad 0 \ \ldots \ j^{max} \ \ldots \ j \ \ldots \ j^{max} \right) \in \mathbb{N}_0^{P^{max}} \end{aligned} \tag{6.15}$$

The index pair i and j of the matrix then reduce to a single index $P(i,j) = j + 1 + \sum_{i'=0}^{i-1} \left(j_{i'}^{max} + 1 \right) \in \mathbb{N}$ ranging over i and j as defined above and P^{max} as total length of the vector. With these three vectors the property space is fully characterised. Please bear in mind that the coordinate transformation only changes the appearance, but not the content of the property space.

6.2.2 Model reduction

The full property space $\mathcal{P}$ as represented in Eq. (6.14) quickly exceeds computational feasibility. In real colloidal suspensions very high particle numbers i^{max} and j^{max} yield an abundance of theoretically possible aggregate configurations. The state space then contains millions of coordinates - each balanced by a differential equation - of which only a fraction is physically relevant. In order to facilitate a numerical solution of the population balance equation, the model has to be considerably reduced. Some common numerical methods were already discussed in section 4.2, and the concept of the method applied in this thesis was already roughly outlined in section 4.4.2. It yields a property space $\mathcal{P}^R$ that is as concise as possible but still contains the relevant physical information at maximum resolution. The reduction algorithm is based on omitting physically irrelevant aggregate compositions in order to considerably reduce the set of differential equations. Mathematically this corresponds to eliminating zero or near-zero elements by a simple sectional approach. The focus on regions within property space with high cluster concentrations is expressed by an interval spacing that varies regionally and with simulated time. The adaptive grid is established under consideration of heuristics gained from predicted aggregation rates. In contrast to sectional approaches with constant resolution and weighted residuals, the presented approach does not reduce system information and proves to be stable against numerical diffusion effects.

In the binary particle mixture, the two dimensions of property space can be subject to different reduction rules. Since restabilisation restricts the coverage with MF-RhB particles to a certain amount, a fixed grid could be established in j direction. Its extent is defined on the basis of heuristic estimations. In contrast, adaptivity is established along the i property vector. Complete rows in the concentration matrix are lumped into single representative coordinates. Once the concentration collected within these states exceeds a threshold value, a fixed region in j direction is opened up. In one adaptation step several neighbouring rows were opened at once to enhance efficiency. The reduced system $\underline{c}^R$ is illustrated in Eq. (6.16) with lumped coordinates shown as shaded areas. Still the upper limits i^{max} and j^{max} have to be chosen much smaller than the total number of particles inside the suspension. In accordance with experimental observations, the maximum number of PS particles in an aggregate is estimated as $i^{max} \approx 10$, and j^{max} corresponds to the highest j_i^{max} as defined in Eq. (6.18).

$$\underline{c}^R = \begin{pmatrix} c_{1,\langle 0,\ldots,j_1^{min}-1\rangle} & c_{1,j_1^{min}} & \cdots & c_{1,j_1^{max}-1} & c_{1,\langle j_1^{max},\ldots,j^{max}\rangle} \\ c_{2,\langle 0,\ldots,j_2^{min}-1\rangle} & c_{2,j_2^{min}} & \cdots & c_{2,j_2^{max}-1} & c_{2,\langle j_2^{max},\ldots,j^{max}\rangle} \\ & & \vdots & & \\ c_{l,\langle 0,\ldots,j_l^{min}-1\rangle} & c_{l,j_l^{min}} & \cdots & c_{l,j_l^{max}-1} & c_{l,\langle j_l^{max},\ldots,j^{max}\rangle} \\ & & c_{l+1,\langle 0,\ldots,j^{max}\rangle} & & \\ & & \vdots & & \\ & & c_{i^{max},\langle 0,\ldots,j^{max}\rangle} & & \end{pmatrix} \tag{6.16}$$

The heuristic definition of important regions in j direction involves two aspects. First, it is assumed that small MF-RhB particles only exist as monomers. Hence, primary heteroaggregation can be modelled by a simplified expression that only com-

prises transfer rates between adjacent property coordinates, as explained in section 4.4.1. Then it is possible to remove the entire first row of property space $\mathcal{P}$ illustrated in Eq. (6.14) and instead store the amount of free MF-RhB monomers in the vector element $c_{P(0,1)}(t) = c_{P(0,1)}(0) - \vec{j}\vec{c}^{T}_{P(i,j)}(t)$ for every time step t. The index $P(i,j)$ now ranges over $i \in [1,\ldots,i^{max}]$. It has to be emphasised at this point, that the assumption is only valid at low ionic strength where any homoaggregation of the MF-RhB particles remains negligible. This approach is not copied for the first column of PS homoaggregates, since such aggregates (dimers and trimers) have been detected in the original suspensions. They might be caused by insufficient stabilisation due to aging effects or by incomplete redispersion before the experiments and are considered in the initial condition of the simulations.

Secondly, property coordinates with zero or near-zero particle concentrations are eliminated from each row. For instance, it is physically irrelevant to consider a PS monomer with all MF-RhB particles in the system bound to its surface or an aggregate of five PS particles without any MF-RhB particle bound to it. A more concise representation of state space can be established by creating an interval within each row $i \in [1,\ldots,l]$, where the system is fully discretised and by lumping all border coordinates into single representative coordinates. The lower and upper boundaries for high resolution areas are determined from the following equations:

$$j_i^{min} = \begin{cases} \max\left\{1, \min_j\left\{ j \middle| c_{P(1,j)} > \xi \cdot \max\left[\vec{c}\right]\right\}\right\} & \text{for } i = 1 \\ \max\left\{j_1^{min}, j_{i-1}^{min}\right\} & \text{for } 1 < i \leq l \\ 1 & \text{for } l < i \end{cases} \tag{6.17}$$

$$j_i^{max} = \begin{cases} \min_j\left\{ j \middle| \frac{\omega_{P'(1,j),P''(0,1)}}{\max_j\left\{\omega_{P'(1,j),P''(0,1)}\right\}} < \xi \right\} + \Delta & \text{for } i = 1 \\ \text{round}\left\{j_i^{min} + j_1^{min} \cdot 2^{g(i)}\right\} & \text{for } 1 < i \leq l \\ j_i^{min} & \text{for } l < i \end{cases} \tag{6.18}$$

with ξ as threshold value and Δ as additional border coordinates for detailed resolution. The upper limit of the first row j_1^{max} is estimated from the primary aggregation rate $\omega_{P'(1,j),P''(0,1)}$ along j. As discussed in section 6.3.1, it suddenly drops due to a sharp increase of the stability ratio $W_{P',P''}$ at the point of restabilisation. As tolerance in Eq. (6.18) $\xi = 1 \cdot 10^{-6}$ is chosen as an arbitrary small number. Having identified j_1^{max}, the remaining property space is restricted to $j_i^{min} + j_1^{min} \cdot 2^{g(i)}$. Choosing $g(i) = i - 1$, property space includes the aggregation of two clusters with maximum coverage. Heuristics from simulations in unreduced systems allow further reduction setting $g(i) = i^{0.4} - 1$ and extending j_1^{max} by $\Delta = 30$.

Regarding i, the extent of the property space was adaptively refined during the simulation. All rows in $\underline{c}^R$ with $i \in [1,\ldots,l]$ are opened in j direction; all elements in the rows exceeding l are lumped into a single representative coordinate. Because property space increases dramatically with i, this is a very efficient way of reducing the system size. In the beginning of a simulation l is chosen according to the initial particle distribution. After the simulation is started, l is adapted and the size of the fully discretised property space extends. The adaptation of property space is performed, once the last fully discretised row l exceeds a threshold aggregate concentration. The threshold ξ is determined as fraction from the highest concentration at time t, i.e. $\xi \cdot \max(\vec{c}(t))$, and was chosen as $1 \cdot 10^{-6}$ in this contribution. This value represents a compromise between system size and loss of information by lumping.

Once the threshold is reached in row $l+1$, the integration is terminated and the result is transformed back into the full system, equally distributing any particles in lumped property coordinates over all coordinates of the full system. Subsequently a new property space grid is defined and the integration is resumed. If i^{max} is limited in accordance with experimental observations, simulations have shown that usually just a single adaptation step is sufficient. The reduced system is shown in Eq. (6.19) with abbreviated vector notation for rows l and $l+1$:

$$\begin{aligned}
\vec{c}^{\,R} &= (\ \ldots \quad c^R_{P(l,j^*)} \quad c^R_{P(l,j^*)} \cdots c^R_{P(l,j^*)} \quad c^R_{P(l,j^*)} \quad c^R_{P(l+1,j^*)} \quad \ldots\ ) \in \mathbb{R}^{P^{max}} \\
\vec{\imath}^{\,R} &= (\ \ldots \quad l \quad l \quad \ldots \quad l \quad l \quad l+1 \quad \ldots\ ) \in \mathbb{N}^{P^{max}} \\
\vec{\jmath}^{\,R} &= (\ \ldots \langle 0, \ldots, j_l^{min}-1 \rangle \ j_l^{min} \ \ldots j_l^{max}-1 \langle j_l^{max}, \ldots, j^{max} \rangle \langle 0, \ldots, j^{max} \rangle \ldots\ ) \in \mathbb{R}^{P^{max}}
\end{aligned} \tag{6.19}$$

where the domain of $\vec{\jmath}^{\,R}$ has changed from $\mathbb{N}^{P^{max}}$ to $\mathbb{R}^{P^{max}}$ due to the arithmetic averaging performed over MF-RhB particle coverage $\langle j \rangle = \sum_j j \cdot c_{P(i,j)} / \sum_j c_{P(i,j)} \in \mathbb{R}$. The concentrations $c^R_{P(i,j^*)}$ are defined as

$$c^R_{P(i,j^*)} := \begin{cases}
c^R_{P(i,1)} & = \sum_j c_{P(i,j)} & \text{for } 1 \le i \le l\,, \quad 0 \le j < j_i^{min} \\
c^R_{P(i,j-j_i^{min}+2)} & = c_{P(i,j)} & \text{for } 1 \le i \le l\,, \ j_i^{min} \le j < j_i^{max} \\
c^R_{P(i,j_i^{max}-j_i^{min}+2)} & = \sum_j c_{P(i,j)} & \text{for } 1 \le i \le l\,, \ j_i^{max} \le j \le j^{max} \\
c^R_{P(i,i-l)} & = \sum_j c_{P(i,j)} & \text{for } l < i \quad , \quad 0 \le j \le j^{max}
\end{cases} \tag{6.20}$$

with the vector index $P(i,j^*) = j^* + \sum_{i'=1}^{i-1} \left[j_{i'}^{max} - j_{i'}^{min} + 2 \right]$. It is important to note that any a priori restrictions of i and j, like i^{max} and j_i^{max}, in order to decrease system size have to be performed with great care to avoid any effects on the solution. Particle concentrations in lumped property coordinates, which basically represent accumulating 'overflow' states, must remain negligible for all times.

6.2.3 Bivariate discrete population balance equation

In the binary colloidal system under investigation, positively charged MF-RhB particles irreversibly aggregate with PS monomers or more complex aggregates (primary heteroaggregation). At moderate coverages this results in electrostatic destabilisation of PS particles and complex heterogeneous aggregates form by secondary heteroaggregation. Hence, the aggregation behaviour depends on the cluster composition which motivates the application of population balance models. As already discussed in section 4.4.1, primary heteroaggregation represents a single-step movement along the j coordinate in each row i of property space according to $P'(i',j') + P''(0,1) \rightarrow P(i',j'+1)$. In contrast, secondary heteroaggregation describes jump throughout property space according to $P'(i',j') + P''(i-i',j-j') \rightarrow P(i,j)$ and is therefore represented by the classic expression for aggregation. The property-discrete population balance can then be formulated as

$$\begin{aligned}
\frac{d}{dt} c_{P(i,j)} \ = \ & \left[\omega_{P',P''} c_{P'(i,j-1)} \ - \ \omega_{P,P''} c_{P(i,j)} \right] \ c_{P''(0,1)} \\
& + \frac{1}{2} \sum_{i'=1}^{i-1} \sum_{j'=0}^{j} \omega_{P',P''} c_{P'(i',j')} c_{P''(i-i',j-j')} \ - \ c_{P(i,j)} \sum_{i'=1}^{\infty} \sum_{j=0}^{\infty} \omega_{P,P'} c_{P'(i',j')}
\end{aligned} \tag{6.21}$$

with $i \in [1,\ldots,i^{max}]$ and $j \in [0,\ldots,j^{max}]$ on reduced property space. Each coordinate of property space is balanced with respect to incoming and outgoing particles. Because in aggregation incoming particles can originate from any two source particles, a double sum considers all possible source combinations. Likewise, all particles leaving the considered property coordinate are summed up in the sink term. The population balance equation is written in a general form and certain aggregation phenomena have to be excluded by definition in order to guarantee mass conservation. Thus, the following aggregation rates are set to zero:

$$\begin{aligned}
\omega_{P'(i,j-1<0),P''(0,1)} &= 0 \\
\omega_{P(i,j>j_i^{max}),P''(0,1)} &= 0 \\
\omega_{P'(i',j'),P''(1-i',0-j')} &= 0 \\
\omega_{P'(i',j'),P''(i''>i^{max}-i',j-j')} &= 0 \\
\omega_{P'(i',j'),P''(i-i',j''>j_i^{max}-j')} &= 0 \quad . \qquad (6.22)
\end{aligned}$$

All restrictions involving i^{max} or j_i^{max} are caused by introducing restrictions into property space. The artificial exclusion of certain aggregation phenomena due to model reduction only has negligible effects on the simulation results because only very low aggregate concentrations are affected. This was validated by simulations with varying i^{max} values and for $i^{max} > 8$ no effects could be observed over the complete simulated time span. Furthermore, the amount of particles collected in boundary property space coordinates remained negligible over the whole simulation, as demanded in section 6.2.2.

6.3 Simulated aggregation dynamics

The population balance model was implemented in MATLAB in its vectorised form. All simulations were performed on a standard personal computer (2.66 GHz, 2 GB RAM) within several minutes. For the two kernel concepts introduced in the previous sections, different simulation results were achieved.

Some simulation parameters were acquired from the reference experiments performed with PS and MF-RhB particles in Chapter 5. The PS particle concentration was chosen as $c_{PS} = 1.14 \cdot 10^4$ particles/μm and MF-RhB particles were added to yield concentration ratios of $c_{P(0,1)}/c_{P(1,0)} = c_{MF-RhB}/c_{PS} =$ 1:1, 20:1, 100:1. Throughout this contribution, the temperature was kept constant at $T = 298$ K. Unless defined otherwise, simulations were performed at an ionic strength of $I_M = 0.1$ mM for pure water. For parameter studies, a totally disaggregated particle system was assumed as initial condition, while simulations intended for comparison with experimental data begin with an aggregate distribution similar to the first measurement. Over the simulated time span of $t_{tot} = 1 \cdot 10^5$ s ($\approx$ 27 h) no significant amount of aggregates comprising more than 10 PS particles were formed. Therefore i^{max} could be limited to 10 for both kernels, considerably reducing the model size. The parameter j_1^{max} was determined as $\approx 13 + \Delta$ and for the charge-balance kernel and as $\approx 20 + \Delta$ for the patchy-particle aggregation kernel from the PS monomer coverage rates $\omega_{P',P''(0,1)}$. With $\Delta = 30$ the condition of negligible concentrations in the border coordinates was met, as required in section 6.2.2.

6.3.1 Kernel evaluation

The distribution of aggregation rates over property space for primary $\omega_{P',P''(0,1)}$ and secondary $\omega_{P',P''}$ heteroaggregation were calculated for three different kernel models: the charge-balance kernel (Eq. (6.5)), the patchy-particle kernel (Eq. (6.10)) and the patchy-particle kernel with $P^c_{P',P''} = 0$. The kernel results are shown in Figure 6.3(a)-(d) for $i^{max} = 5$. The Smoluchowski kernel ω^B generates perikinetic aggregation rates of order $1 \cdot 10^{-17}$ m^3/s, which may be reduced by the stability ratio $W > 1$ in the RLCA regime. The displayed rates compare well to literature data, which cover a range from $1 \cdot 10^{-18}$ to $1 \cdot 10^{-17}$ m^3/s as average rates in binary heteroaggregation[39,86,113]. As can be observed in Figure 6.3, aggregation is confined to certain aggregate property states. Outside these, aggregation is prevented by the restrictions set by the respective kernel concept, i.e. either by a completely cluster covered surface or by sufficiently high repulsive forces between the approaching particles. For the coverage process as well as for cluster-cluster aggregation, the rates of

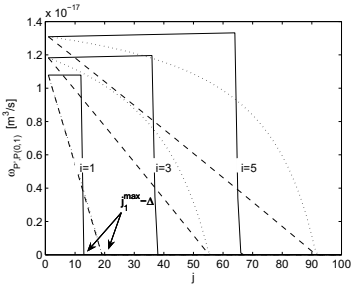

(a) Primary heteroaggregation rates for $i \in 1, 3, 5$.

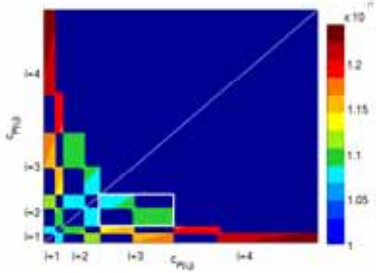

(b) Secondary heteroaggregation rate matrix calculated by the charge-balance kernel with $\mathcal{C} = 1$, Eq. (6.5).

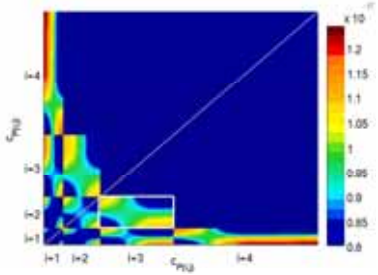

(c) Secondary heteroaggregation rate matrix calculated by the patchy-particle kernel, Eq. (6.10).

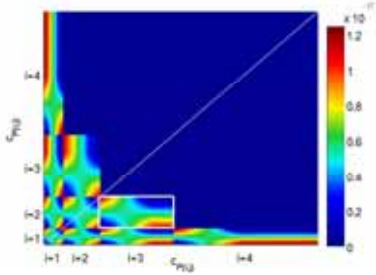

(d) Secondary heteroaggregation rate matrix of the patchy-particle kernel with $P^c_{P',P''} = 0$.

Figure 6.3: Simulated primary and secondary aggregation rates as predicted by different kernels. (——): Charge-balance kernel (Eq. (6.5)), (– –): Patchy-particle kernel (Eq. (6.10)), $(\cdots)$: Patchy-particle kernel with $P^c_{P',P''} = 0$. Large regions with zero rates are caused by the restriction to $i^{max} = 5$. For illustrative purposes a white box marks all aggregation rates between $P'(3, [0, \ldots, j_3^{max}])$ and $P''(2, [0, \ldots, j_2^{max}])$. The symmetry axis is indicated by a white diagonal line. The colour coding represents the aggregation rate $\omega_{P',P''}$ in [m^3/s] with zero and near-zero rates shown in a dark blue colour.

the different kernels show systematic differences. The charge-balance kernel shows abrupt changes of the aggregation rates. It indicates the transition from DLCA to RLCA regime and is caused by the the sudden increase of the stability ratio W at a critical surface coverage. For the charge-balance kernel, the maximum coverage is defined by the charge balance: when a certain critical number of MF-RhB particles is adsorbed, the reversed heteroaggregate charge prevents any further coverage. For both $P^c_{P',P''} = 0$ and $P^c_{P',P''} > 0$ in the patchy-particle kernel, the initial rate as well as the maximum coverage coincide as fixed by the surface coverage expression. In between, the rate linearly drops to zero at maximum coverage with $P^c_{P',P''} = 0$. For nonzero probability of multiple collisions $P^c_{P',P''} > 0$ the rates are higher and no longer linear. The nonlinearity is more pronounced for higher dimensional clusters. The maximum coverage for the patchy-particle kernels was fitted by choosing $\gamma = 3$ in Eq. (6.13) to achieve agreement on the time evolution of the aggregation kinetics shown in section 6.3.3.

6.3.2 Variations of the charge-balance kernel

After the kernels have been evaluated for the considered property space, the population balance equation can be solved. As an example, Figure 6.4 shows a detailed cluster distribution on two-dimensional property space calculated on the basis of the unfitted charge-balance kernel with $\mathcal{C} = 1$. For systems in which the maximum coverage is restricted as specified by the charge balance in Eq. (6.9), bimodal distributions along the j coordinate are possible. They originate if the leading tail of the particle distribution is collected in the property coordinate $P(i, j_i^{max})$ with maximum coverage, from which the clusters can only drain by means of secondary aggregation. For a concise and transparent comparison of the time evolution, selected results are presented in the following graphs. These include the concentration fractions of uncovered and covered PS monomers, PS oligomers as well as the MF-RhB coverage on PS monomers. For a standard simulation at $c_{PS} = 1.14 \cdot 10^4$ particles/μl and a mixing ratio of 20:1 in deionised water with $I_M = 0.1$ M and $T = 298$ K, simulations were validated on an extended property space. The extension was realised by choosing $i^{max} = 7$, $g(i) = 0.8$, $\Delta = 30$ as parameters. A comparison between the reduced and extended system shows identical results to simulations at $i^{max} = 10$, $g(i) = 0.4$, $\Delta = 30$ that are henceforth adopted as standard simulation parameters. The simulations with the charge-balance kernel shown in this section were not fitted, i.e. the parameter $\mathcal{C}$ was chosen as unity.

The influence of the aggregate morphology and compactness was investigated by varying the fractal dimension for the rate limited cluster-cluster aggregation from $d_f = 1$ to 3. The aggregation kinetics remain essentially the same over the complete interval with deviations becoming evident for high times of $t > 4 \cdot 10^4$ s only. Even for simulations with a constant aggregate radius of $r_{P(1,0)}$ throughout the whole property space, aggregation kinetics barely change. According to Eq. (2.28) a constant radius is achieved in the limit of $d_f \to \infty$. The results for $d_f = 1$ and 1000 along with $d_f = 2.1$ are plotted in Figure 6.5. The low sensitivity of aggregation kinetics on the fractal dimension is caused by the moderate change of aggregate size during the destabilisation phase, where practically all PS heteroaggregates remain monomeric. Only after destabilisation at advanced times, the average aggregate size increases

due to cluster-cluster aggregation and d_f gains impact. With increasing aggregate size, Brownian motion slows down and aggregation is decelerated.

Sensitivity regarding the van der Waals force $V^{vdW}_{P',P''}$ was assessed by variations of the Hamaker constant $A_{P',P''}$ (data not shown). For moderate increases of the Hamaker constant $A_{P'(i',j'),P''(i'',j'')}$ simulations only show insignificant differences. Simulations with $A_{P'(i',j'),P''(0,1)} = 1 \cdot 10^{-20}$ J matched those with $A_{P'(i',j'),P''(0,1)} = 2.2 \cdot 10^{-20}$ J, which was used for the interaction of MF-RhB and PS surfaces throughout the thesis. Deviations begin to take noticeable effect, when the Hamaker constant is increased by a factor of >10. Likewise, the effect of the hydrodynamic correction $B_{P',P''}$ in Eq. (2.24) is shown to be negligible. For $B_{P',P''} = 1$, no differences in aggregation kinetics were detected at all (data not shown). Both effects show how the electrostatic particle interaction physically dominates the aggregation process over van der Waals attraction and hydrodynamic close distance effects.

Simulations also demonstrated the sensitivity of aggregation kinetics on the ionic strength of the surrounding medium. The increased stability of MF particles agains aggregation to PS surfaces could however not be validated by simulations. At increasing electrolyte concentration, particle surface charge is shielded more effectively, reducing the extent of the electrostatic double layer and interaction potentials[23,151]. Aggregation kinetics begin to be affected by increasing electrolyte concentration from ionic strengths of $I_M > 10$ mM. The aggregation results for $I_M = 20$ M are included in Figure 6.5 and exactly match those for a pure DLCA regime, simulated with constant stability ratio $W = 1$. This is in full accordance with theory because at very high ionic strengths virtually no electric double layer remains around the particles and they can aggregate spontaneously as fast as diffusion permits. Therefore, the coverage of MF-RhB particles on PS monomers is not impeded by electrostatic repulsion and can increase beyond the coverage reached under RLCA. Furthermore, at increased ionic strength cluster-cluster aggregation does not require monomer destabilisation and aggregation occurs species-independent and simultaneously, not consecutively. Because the aggregation between MF-RhB monomers is not accounted for in the pop-

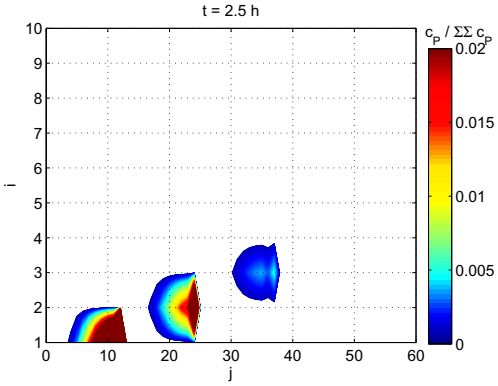

Figure 6.4: Two-dimensional distribution of cluster composition for $c_{MF-RhB}/c_{PS} = 20{:}1$ at $t = 2.5$ h. Destabilisation of PS monomers initiates cluster-cluster aggregation. Colour coding shown in particle fraction linearly interpolated between two consecutive discrete elements.

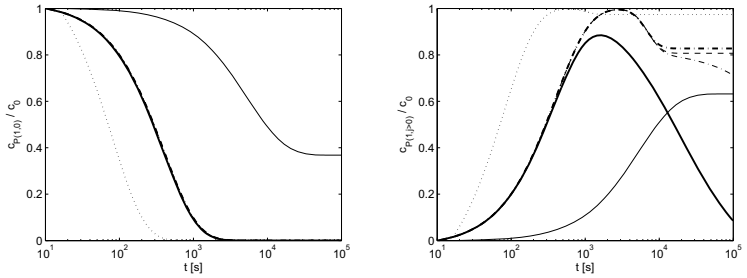

(a) PS primary particles. (b) PS monomers covered with MF-RhB.

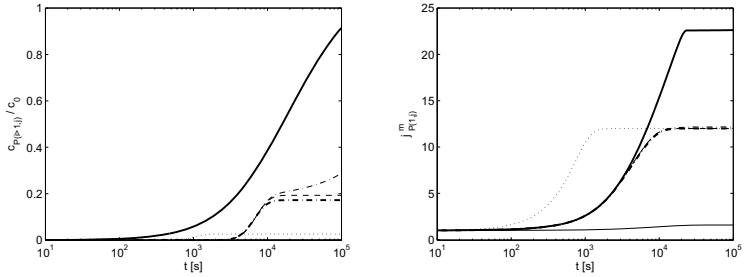

(c) PS oligomers. (d) MF-RhB coverage of PS monomers.

Figure 6.5: Heteroaggregation dynamics simulated with the charge-balance kernel ($\mathcal{C} = 1$) expressed as concentration fractions and mean coverage. PS monomers at $c_{PS} = 1.14 \cdot 10^4$ particles/μl were set as initial condition. Standard conditions (—) imply a 20:1 mixing ratio , $d_f = 1.8$ for primary and $d_f = 2.1$ for secondary heteroaggregation, $I_M = 0.1$ mM and $T = 298$ K. The following parameter variation are presented: 1:1 mixing ratio (—), 100:1 mixing ratio ($\cdots$), identical $d_f = 1$ (—·—), identical $d_f = 1000$ (—•—•—), $I = 20$ M (—). In (a) all variations coincide with the simulation at standard conditions.

ulation balance equation (6.21), simulations at elevated ionic strength tend to loose their accuracy.

Besides the ionic strength, the most dominant effects on aggregation kinetics were observed by variations in absolute PS particle concentration c_{PS} and by the particle mixing ratio c_{MF-RhB}/c_{PS}. By doubling c_{PS}, primary and secondary heteroaggregation are enhanced. All curves in Figure 6.5 are shifted towards the left, so that the peak of covered PS monomers for the 20:1 ratio at $I_M = 0.1$ mM moves from $t = 2830$ s at $1.14 \cdot 10^4$ particles/μl to $t = 1410$ s at $2.28 \cdot 10^4$ particles/μl (data not shown). At half concentration the peak of covered PS monomers is observed at $t = 5660$ s. Variations of the particle mixing ratio c_{MF-RhB}/c_{PS} considerably changes the aggregation dynamics as well. The underlying electrostatic effects are discussed in the following section.

6.3.2.1 Electrostatic effects

Electrostatic effects dominate the aggregation behaviour of the investigated binary particle system. As discussed in Chapter 5, they can be controlled by the macro-

scopic mixing ratio c_{MF-RhB}/c_{PS}. Simulations were conducted for particle ratios of 1:1, 20:1 and 100:1, each representing a distinct electrostatic effect. For the 20:1 ratio primary is joined by secondary heteroaggregation and complex oligomer aggregates are readily formed. For the 1:1 and 100:1 ratios aggregation ceases after primary heteroaggregation. In the 1:1 ratio secondary heteroaggregation is impeded by lacking destabilisation, while in the 100:1 suspension highly covered PS monomers are restabilised (Figure 5.9).

The same is also expressed by the simulation data of Figure 6.5. For the 20:1 particle ratio, PS monomers are quickly covered by MF-RhB particles. The sigmoidal decrease of uncovered PS monomers in Figure 6.5(a) correlates with an increase of covered PS monomers in Figure 6.5(b). Once the critical coverage is reached, PS monomer heteroaggregates are electrostatically destabilised and aggregate with other clusters, forming more complex aggregates. Similar to the experimental section, these are lumped into a single PS oligomer class for clarity of presentation, which is shown in Figure 6.5(c). Once the source of covered PS monomers is outbalanced by oligomer formation, the amount of covered PS monomers in Figure 6.5(b) reaches a peak and decreases. Towards the end of the simulation, nearly all MF-RhB particles have adsorbed ($> 98\%$, data not shown) and the coverage on PS monomers in Figure 6.5(d) reaches an asymptotic limit of ≈ 12 MF-RhB particles per PS monomer.

For the 1:1 ratio, aggregation kinetics are much slower, due to fewer collisions between PS and MF-RhB monomers. PS particles are divided between the uncovered and covered state (Figures 6.5(a) and (b)), no oligomers are formed (Figure 6.5(c)) and the PS monomer coverage remains steady at 1 particle per PS monomer as is expected at this mixing ratio (Figure 6.5(d)). The electrostatic repulsion of weakly covered PS monomers is maintained and prevents cluster-cluster aggregation.

At $c_{MF-RhB}/c_{PS} = 100:1$, PS monomers are rapidly covered with MF-RhB particles (Figure 6.5(b)). The chances of destabilised PS monomers to aggregate with other clusters are very slim, due to low cluster-cluster collision probabilities. Owing to the high concentration ratio, increasing MF-RhB particle coverage is more probable and the time-window, in which cluster-cluster aggregation is possible, passes without significant oligomer formation (Figure 6.5(c)). Finally, aggregation is retarded by the restabilisation effect with an average of 12 MF-RhB particles adsorbed on each PS monomer (Figure 6.5(d)).

6.3.3 Comparison of both kernels to experimental data

In principle all variations performed with the charge-balance kernel can also be done with the patchy-particle kernel. Since the central statements remain unchanged, the results are not included. The patchy-particle kernel is however tested against the experimental data for different particle mixing ratios.

The fit of simulation results and experiments could be improved by slight modifications of γ, N_{11} and α. By choosing $\gamma = 3$ the effective surface area covered by a single MF-RhB particle is extended by a factor of ≈ 8. This reduces the maximum number of MF-RhB particles from 163 to ≈ 21, which is more consistent with experimental data. The introduction of an excluded surface area to each adsorbed MF-RhB particle, is also physically reasoned by the electrostatic repulsion to other MF-RhB particles on the PS surface. However, the exact extent caused by this eluded experi-

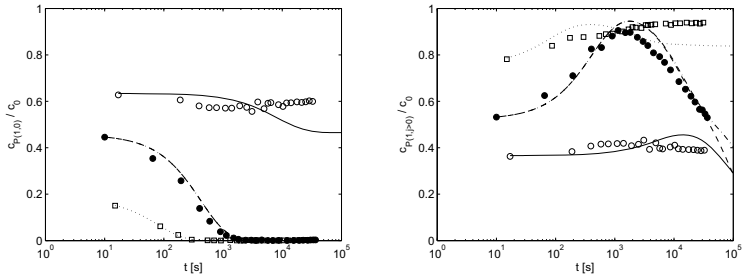

(a) PS primary particles.

(b) PS monomers covered with MF-RhB.

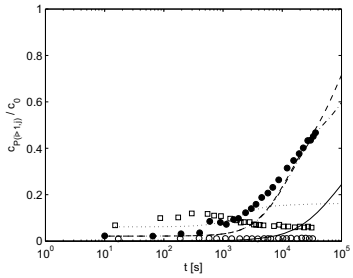

(c) PS oligomers.

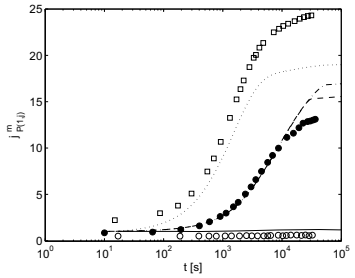

(d) MF-RhB coverage of PS monomers.

Figure 6.6: Comparison of experimental with simulated aggregation dynamics using the patchy-particle aggregation kernel. Experimental and simulated data for mixing ratios of 1:1 (○, ——), 20:1 (•, – –) and 100:1 (□, · · ·) along with $P^c_{P',P''} = 0$ as modification of the patchy-particle kernel (·—·—). The remaining experimental and simulation conditions match the standard conditions of Figure 6.5.

mental observability with the given devices. Furthermore it is known from literature that shielding effects due to cluster formation[102,103] create surface regions that are inaccessible for MF-RhB particles and thus limit the the average number of surface MF-RhB particles. The kernel approach developed by Olsen et al.[102] was however not considered here. In the simulations, particle concentrations and initial conditions were chosen identical to the experimental values. The results are plotted in Figure 6.6 along with the experimental data.

The charge-balance kernel was also tested against the experimental results. The results at standard conditions for different mixing ratios of 1:1, 20:1 and 100:1 are shown in Figure 6.7. The charge balance was fitted by choosing $\mathcal{C} = 0.7$ in Eq. (6.9). This allows more MF-RhB particles to be attached to a PS monomer, but delays the onset of secondary heteroaggregation.

In principle, all simulations predict the aggregation behaviour for different concentration ratios correctly. However, deviations exist between the different kernel models, and between simulations and experiments. In Figures 6.6(a) and 6.7(a) the decrease of uncovered PS monomers is predicted equally well by both kernels and nearly matches experimental data. Differences exist for the 1:1 ratio, where the simulation predicts a sigmoidal change of PS monomer concentration fractions, while the experimental data indicates a flat response. Depending on the values of α and N_{11},

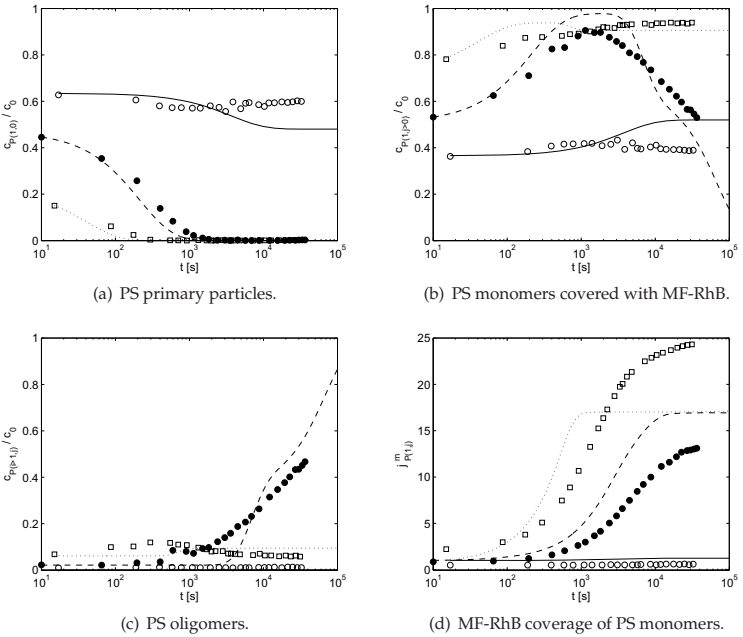

(a) PS primary particles.

(b) PS monomers covered with MF-RhB.

(c) PS oligomers.

(d) MF-RhB coverage of PS monomers.

Figure 6.7: Comparison of experimental with simulated aggregation dynamics using the charge-balance kernel. Experimental and simulated data for mixing ratios of 1:1 (○, ——), 20:1 (•, – –) and 100:1 (□, –·–·–) fitted with $\mathcal{C} = 0.7$. The remaining experimental and simulation conditions match the standard conditions of Figure 6.5.

the patchy-particle kernel maintains a slight decrease of uncovered PS monomers even towards the end, while the charge-balance kernel is quite robust here. For both kernels the small changes caused by the adsorption of a single MF-RhB particle seem to permit the formation of a small PS oligomer fraction.

The fraction of covered PS monomers is shown in Figures 6.6(b) and 6.7(b) and the different aggregation regimes for the different mixing ratios are clearly visible: lacking destabilisation at low, continuous aggregation for intermediate and restabilisation at high mixing ratios. The concept of the charge-balance kernel proves to be more robust for the extreme mixing ratios of 1:1 and 100:1, while for the intermediate 20:1 ratio the aggregation kinetics are better described by the patchy-particle kernels. The two variations of the patchy-particle kernel represent an upper ($P^c_{P',P''} > 0$) and a lower boundary ($P^c_{P',P''} = 0$) with regard to aggregation kinetics[98]. As can be seen from Figure 6.6(b)-(d), this only affects the 20:1 ratio. For this ratio, the peak of covered PS monomers is predicted closer to experimental observations by the patchy-particle kernel. Only towards the end, the patchy-particle kernel overestimates the aggregation dynamics. The peak predicted by the charge-balance kernel is higher and prolonged. The delayed onset of cluster-cluster aggregation is influenced by the fitting parameter $\mathcal{C}$ as was explained in section 6.1.2.1. For both extreme mixing ratios, 1:1 and 100:1, the simulation results qualitatively match the experimental findings over a large interval for the selected parameters. Any cluster-cluster aggregation is

indicated by the decrease of raspberry aggregates correlating with an increase of the PS oligomer fraction in Figure 6.6(c) or 6.7(c). For the 100:1 ratio, the charge-balance kernel predicts a slightly lower fraction of PS oligomers and therefore compares better to experimental data.

The evolution of the oligomer fractions is shown in Figures 6.6(c) and 6.7(c). Deviations from experimental data correlate with deviations of the PS monomer fractions in Figures 6.6(b) and 6.7(b). The slight overestimation of aggregation dynamics by the patchy-particle kernel causes a steeper rise of PS oligomer concentration as can be observed in Figure 6.6(c). Similarly, the delayed onset of cluster-cluster aggregation as predicted by the charge-balance kernel with $\mathcal{C} = 0.7$ propagates into the PS oligomer fraction as shown in Figure 6.7(c). For this kernel, oligomer formation only sets in following PS monomer destabilisation, but then causes a very rapid oligomer increase similar to that of the patchy-particle kernel.

The number of adsorbed MF-RhB particles on PS monomers is shown in Figures 6.6(d) and 6.7(d). It is compared to the experimental data from fluorescence intensity measurements. The restriction to the coverage of PS monomers was done to limit the complexity. Although the coverage of higher order PS clusters is available from experimental and simulated distributions, it is not shown here since no new information of essential importance regarding an understanding of the aggregation process is added. In most cases the simulations confirm the sigmoid increase of MF-RhB coverage on PS monomers. Some mismatch exists with respect to the final equilibrium coverages. In simulations these can be tuned by γ for the patchy-particle kernel or $\mathcal{C}$ for the charge-balance kernel. But since the calibration $fl2$ by which fluorescence intensities are converted into absolute particle numbers is accompanied by a large error, a rough fit to the experimental is considered as sufficient.

The results for all three mixing ratios vary with regard to the final PS monomer coverage. For the 1:1 ratio the minimum coverage of a single MF-RhB particle is confirmed in both cases. For the 100:1 ratio, the respective maximum coverage is reached quickly for both kernels. Since PS monomers have reached stability against further aggregation at maximum coverage, the remaining MF-RhB particle remain unbound in solution. For the intermediate 20:1 ratio determined with the patchy-particle kernel, the final coverage of ≈11 MF-RhB particles falls remains below the maximum coverage of ≈ 18 MF-RhB. Thus, a lack of further free MF-RhB particles is noticed, although both the mixing ratio and maximum coverage exceed the final MF-RhB number. The difference to the theoretically possible maximum coverage is caused by the simultaneous aggregation of MF-RhB particles with higher order PS clusters. Because primary heteroaggregation is not limited to PS monomers, PS clusters can also act as sinks for free MF-RhB particles and thus deplete the number of free MF-RhB particles. In contrast, the maximum coverage reaches only ≈14 MF-RhB particles for the charge balance kernel. Since the charge balance kernel allows less MF-RhB particles on PS particles, the maximum coverage for this kernel is also achieved in case of the 20:1 ratio.

All in all, the results suggest that cluster-cluster aggregation is influenced by bridging effects between surface patches more than by an averaged cluster surface potential. The SEM images for binary and ternary systems shown in Figure 5.7 support these indications. The observed deviations between simulations and experiments are probably caused by a combination of uncertainties from both approaches. With regard to the simulations, both kernel concepts are based on assumptions, which are

inevitable for a reduction of the system complexity. On the one hand, the charge-balance kernel is based on an approximate calculation of the aggregate surface potential (Eq. (6.8)), on the other hand, the patchy-particle concept allows cluster-cluster aggregation via a bridging effect. Both concepts only provide rather crude considerations of morphological details. In addition, the presented results neglect any restructuring effects, like surface diffusion of MF-RhB particles on PS surfaces. Restructuring effects and aggregate morphology can exert important influence on aggregation dynamics and would have to be examined in more detail by simulation methods that resolve geometric details, like Brownian dynamics simulations mentioned in Chapter 4. With respect to the experiments, several sources of error were identified in section 5.2. Next to the assumption of homogeneous mixing, which can only be approximate in diffusive systems, the adjustment of particle concentration and mixing ratio probably present the main sources of error. Additional errors might arise from measurements by flow cytometry. Although narrow confidence intervals around the dynamic particle concentrations were verified in section 5.2.2.1, very weak particle aggregation dynamics might not be detected or breakage of large aggregates might occur. Furthermore, the transformation of the measured fluorescence intensity into a MF-RhB number is based on a somewhat insecure microscopic calibration.

6.3.3.1 Phase portraits

The transition between destabilisation, i.e. PS monomer coverage, and cluster-cluster aggregation for the 20:1 ratio is emphasised in the phase plots of Figure 6.8. While the results of the charge-balance kernel suggest a very sharp onset of secondary aggregation, the patchy-particle concept indicates a more gradual change consistent with experimental data. The more gradual transition between initial destabilisation phase and cluster-cluster aggregation of the patchy-particle kernel, weakens the onset of restabilisation, and the flattening of the 100:1 curve in Figure 6.6(d) compared to Figure 6.7(d) is not as pronounced.

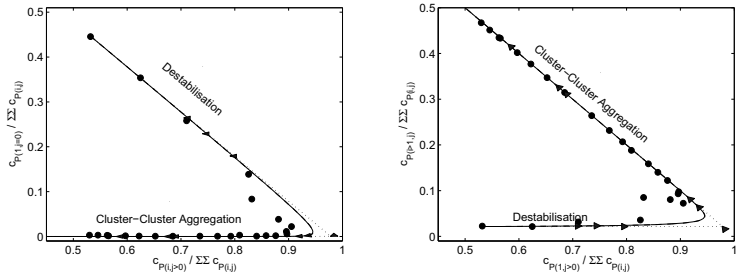

Figure 6.8: Phase portraits of PS monomer and aggregate fractions for $c_{MF-RhB}/c_{PS} =$ 20:1. Destabilisation and cluster-cluster aggregation regimes are indicated. Simulated results are shown for the charge-balance kernel (Eq. (6.5), ——), the patchy-particle kernel (Eq. (6.10), – – –) and the patchy-particle kernel with $P^c_{P',P''} = 0$ ($\cdots$). They are independent of the initial condition. Arrows indicate the direction of temporal evolution and are plotted at simulation times $t/t_{tot} = 0.3, 0.5, 0.85$.

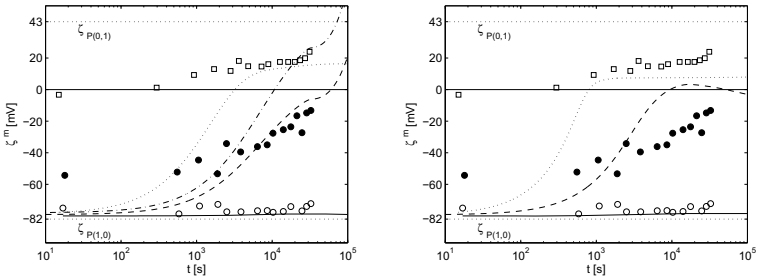

(a) Patchy-particle kernel (b) Charge-balance kernel

Figure 6.9: Comparison of experimental and simulated ζ-potentials for mixing ratios of 1:1 ($\circ$, ——), 20:1 ($\bullet$, $\mathcal{C} = 0.7$: – –, $\mathcal{C} = 1$: ·–·–·) and 100:1 ($\square$, · · ·).

6.3.3.2 Evolution of aggregate ζ-potentials

The experimental evolution of the ζ-potential was presented in section 5.3.1.3 for the Microparticle PS standard. It shows the dynamic evolution of average values over the total particle ensemble that passed the laser beam. For the Duke Scientific PS standard the experimental results are plotted in Figure 6.9 and show slight differences as a consequence of the different pure ζ-potentials (Table 5.1).

To compare this data with simulations, the simulated particle distributions have to be transformed into averaged aggregate surface potentials $\Psi^0_{P(i,j)}$. This can easily be achieved with the charge balance of Eq. (6.9). For each coordinate in property state a representative cluster charge is calculated and weighted by the respective particle fraction inside that coordinate. In principle, the surface potential can be obtained for the distributions calculated with both kernel concepts. But it is only for the charge-balance kernel that a changing potential has direct influence on the aggregation dynamics. For the patchy-particle kernel this information does not affect the aggregation dynamics. The surface potentials $\Psi^0_{P(i,j)}$ obtained from the simulated cluster distribution are plotted in Figure 6.9(a) and (b). In order to compare experimental data with simulation results we have to assume that the surface potential $\Psi^0_{P(i,j)}$ matches the ζ-potential of the clusters. This assumption was already made to derive Eq. (6.8).

As already mentioned in section 5.3.1.3, ζ-potential measurements in highly concentrated systems with particles of opposite ζ-potential are subject to errors. With increasing mixing ratio, the measured initial ζ-potential of PS aggregates is higher than an increased initial coverage would account for. Because this cannot be accurately copied in silico, simulations deviate from experimental results, especially in the beginning when large numbers of MF-RhB particles are free in solution. The trends, however, are predicted well for all three mixing ratios. For the 1:1 ratio we obtain nearly unchanged particle ζ-potentials, and for $c_{MF-RhB}/c_{PS} = 100{:}1$ charge reversal and restabilisation agree qualitatively. For the 20:1 ratio an asymptotic limit is reached for the charge-balance kernel, which shows a slight overshoot into mean positive cluster charge. For the patchy-particle kernel, the surface potential at 20:1 shows an artifact towards the end. For $\mathcal{C} = 0.7$ the mean aggregate potential even exceeds the ζ-potential of MF-RhB particles. This is caused by the slightly greater maximum

coverage defined by the patchy-particle kernel in comparison to the charge-balance kernel. Naturally, the mean aggregate charge takes off towards unphysically high surface potentials. This can be corrected by adjusting the fitting parameter $\mathcal{C}$ to unity, yielding a higher maximum coverage. The rapid potential towards the end remains however.

The qualitative agreement between the simulations and the experimental data is quite satisfactory, especially if the crudeness of the kernel models is considered. The three main electrostatic effects at the different mixing ratio are predicted well. It seems reasonable that these results reflect the microscale origin of the dominating electrostatic effects on the macroscale.

6.4 Summary

Heteroaggregation phenomena in particle mixtures comprising two species of different size and ζ-potential were investigated by simulation. A bivariate population balance model was established on an adaptive grid within a property-discrete state space, which was subject to reduction by a semi-heuristic approach. The two internal coordinates represent the particle species and characterise the cluster composition. The aggregation rates are determined by two different kernel concepts, which are based on deterministic models under consideration of Brownian motion and DLVO theory, incorporating Born, van der Waals and electrostatic pair interaction energies. The kernel for patchy-particles accounts for the heterogeneous surface structure of aggregated clusters[98], while a charge-balance kernel calculates the interaction potential between two clusters on the basis of a mean electrostatic charge. Averages of the calculated rates agree with literature values. Simulations with the charge-balance kernel were studied with respect to parameter sensitivity. Variation of the fractal dimension and the aggregate size, as well as of the hydrodynamic correction in the stability ratio only show minor effects. The simulation results show sensitivity with respect to the ionic strength and absolute particle concentration.

Both models are successfully tested against experimental findings. Although slight deviations exist between simulations and experiments, aggregation phenomena influenced by the macroscopic mixing ratio c_{MF-RhB}/c_{PS} are predicted correctly. At 1:1 ratio aggregation is essentially prevented, at 20:1 ratio primary aggregation is followed by cluster-cluster aggregation forming complex heteroaggregates, and at 100:1 ratio PS monomers are restabilised by a dense coverage with MF-RhB particles impeding any further aggregation. While the charge-balance kernel performs slightly better in the cases of lacking destabilisation at low mixing ratios (1:1) and restabilisation at high ratios (100:1), the patchy-particle kernel predicts a more gradual transition between the initial destabilisation phase and secondary heteroaggregation at intermediate ratios (20:1). The measured dynamic evolution of the mean ζ-potential confirms the trends investigated in the simulations.

Part III

Preferential aggregation in biological systems

Equipped with the experimental tools and simulation methods presented in Part I and Part II, we can direct our attention to the systematic investigation of cellular targeting dynamics for drug delivery purposes. The selective adsorption to specific cells is considered as first important transport limitation that carrier entities encounter on their route to intracellular drug delivery. Efficient drug delivery under simultaneous minimisation of adverse effects is a rapidly evolving research area of very high potential for medical applications. In this context, the preferential adsorption of biomolecules, like antibodies, to cellular receptors represents a competitive heteroaggregation process. Numerous recent studies have focused on tailoring these interactions to achieve improved control over this process[58,85,126]. For drug targeting purposes different receptor expression levels are required on the surfaces of the cell types involved. However, cellular systems in which a certain kind of receptor is exclusively expressed on one cell type are rare, so that in practice the targeting selectivity is determined by the extent of receptor expression. Facing these and other limitations, the targeted delivery of drugs poses a research area of high activity, especially in optimising the carrier particles[31,57,105,112,136,143,158] and in cellular uptake studies[17,34,91,129,139], including the special focus on virus infection studies[1,43,137,153]. These two angles of perception, one from particle technology and one from biomedicine, are necessary to cope with the interdisciplinarity and immense system complexity.

Carrier design for in vivo applications has to combine versatile and sometimes conflicting functionalities. Next to carrier morphology, which was recently shown to play a major role in the uptake behaviour of cells[17], appropriate surface functionalities are subject to intense investigations. In general, the surfaces of drug carrier particles should incorporate functionalities regarding bioavailability inside an organism, specificity for a target cell and a controlled release of the drug at the target destination. To enhance the bioavailability of carrier particles inside an organism, biocompatible polymer coatings, for example with polyethylene glycol (PEG), avoid premature removal from the vascular system by an immune response (stealth particles)[31,105]. Biological specificity is usually generated by attaching specific ligands, like antibodies or DNA/RNA, to the particle surface[31,57,99,129,143]. And finally, entry into the cell and the release of the drug from the carrier at the target site has to be controlled. The latter can be achieved by time dependent degradation of the carrier particle or by other approaches that either harness environmental conditions at the target destination, for instance pH dependent degradation in endosomes[26], or make use of external stimuli[139]. Furthermore, the biodegradability of the carrier after drug delivery has to be ensured or at least any adverse effects have to be prevented[31,112].

In this part, the targeting dynamics in a model biological system is presented as case study. It focuses on targeting of two human tumour cell lines in mixture with antibodies. Experimental results are illustrated in Chapter 7. U-937 histiocytic lymphoma cells in mixture with KARPAS-299 cells from anaplastic large cell lymphoma were targeted by aminopeptidase N (CD13) antibodies. The targeting dynamics were simulated by means of a discrete population balance model with three internal coordinates in Chapter 8. All species were approximated as particulate entities, so that the models for geometry and aggregation rates of Part II remain conceptionally valid. The aggregation rates are based on similar deterministic models, adapted to discriminate between biologically specific and unspecific interaction on heterogeneous cell surfaces. For convenience, antibodies and antibody coated drug carrier particles are jointly termed bionanoparticles. The validated model of the targeting process with antibodies on tumour cells was published as journal contribution[123].

Chapter 7

Experimental targeting dynamics

The dynamics of heteroaggregation processes in biocolloidal systems were investigated with flow cytometry. By means of multi-fluorescence staining, the dynamics of antibody-cell aggregation could be detected separately for each cell type. Fluorescent aminopeptidase N antibodies were used to study targeting in a model cellular system. The adsorption of antibodies to surface receptors on cells represents the first major transport limitation on a single-cell level. Any insight into the aggregation process and its dynamics might therefore present a basis to optimise the surface functionalisation of carriers and improve targeted drug delivery. Direct in vivo targeting studies with functionalised carriers were not conducted within this thesis. Although they would present the principal aim on a long-term perspective, the extension of investigations to this area lies beyond the scope of this work.

Following a short introduction into the biomedical background in section 7.1 that sets the stage as model system for our case study, the experimental materials and methods are explained in sections 7.2 and 7.3. Like in Chapter 5, special attention is paid to methods concerning flow cytometry, revealing several matching procedures. The detected antibody aggregation dynamics are presented and discussed in section 7.4.

7.1 Biological background

As mentioned in the introduction, nanotechnology opens up promising perspectives for the targeted delivery of pharmaceuticals to specific cells within an organism by means of carrier particles. The applied carriers are usually tailored to minimise adverse effects for the remaining cells. This application is closely linked to marking specific cells, e.g. tumour cells, for therapeutic purposes. An interesting model system with a specific biomedical application is represented by aminopeptidase N receptors on human tumour cells.

Aminopeptidase N (also known as membrane alanyl-aminopeptidase, EC3.4.11.2, mAAP, CD13) is a type II membrane spanning 150 kDa cell surface protein that is expressed in various epithelial cells and in macrophages [104]. It is known from literature that the only vascular structures with detectable CD13 proteins are tumour blood vessels and other types of vessels undergoing neo-angiogenesis [106]. Therefore, CD13 can be employed as a functionally important marker of angiogenically active vasculature and might represent an important marker for tumours.

Angiogenesis is the fundamental process by which new blood vessels are formed, a process that requires new capillaries to sprout from existing blood vessels. It is a highly regulated process and the normally quiescent vasculature is activated for a brief period of time only. Persistent, deregulated angiogenesis has been implicated in several pathological conditions, notably in tumour development[145]. Extensive research has shown that tumours can deregulate angiogenesis to ensure their survival, growth and metastasis[145]. Because cells require oxygen and nutrients from the blood, a location within 100 to 200 μm of blood vessels is necessary, which is approximately the diffusion limit of oxygen within tissue[15,36]. Therefore, the formation of new blood vessels presents a rate-limiting step in solid tumour growth. The identification of a negative regulator of angiogenesis could provide a strategy for tumour dormancy[36], and a promising method for an efficient administration of such regulators is posed by targeted drug delivery.

Common drug carrier systems involve biocompatible and biodegradable liposomes or virosomes[34,129], (nano)particles[105,158], or multi-layer capsules[57,143]. In order to target specific cellular receptors or antigens, the surface of the carrier has to be functionalised[99], which is usually achieved by coating with different molecules or biological entities, like DNA/RNA[85] or antibodies. Usually the highly specific non-covalent binding between complementary biological proteins is facilitated by a superposition of molecular interactions and bridging forces as well as dynamic conformational adaptations. Due to their high specificity, biomolecules are well suited for biologically mediated self-assembly processes, like the reversible formation of binary colloidal structures. Numerous recent studies have focused on tailoring these interactions between colloidal particles to achieve an improved control over the self-assembly process[58,85]. Experimental investigations of cellular uptake of functionalised carrier particles is an area of ongoing interdisciplinary research[91,158]. In some studies the targeted drug is designed to influence cellular control mechanisms or to preferentially kill the internalising cells[1,52].

7.2 Materials

Aggregation experiments were conducted in incubated mixtures of human U-937 and human KARPAS-299 suspension cells. Both cell lines were obtained from the German Collection of Microorganisms and Cell Cultures (DSMZ, Braunschweig, Germany; ACC 31 and ACC 5, respectively) and cultured at 37°C in a 5% CO_2-in-air atmosphere in 90% RPMI 1640 supplemented with 10% FBS (PAA, Austria, Cat.No. E15-840). Light microscopic images of the cells are shown in Figure 7.1. Immunological data as determined by the DSMZ is shown in Table 7.1. Based on this information, CD13 and CD33 were chosen as cellular targets for the preferential aggregation of antibodies to tumour cells.

Phycoerythrin (PE) labelled monoclonal mouse anti-human CD13 and mouse anti-human CD33 antibodies were purchased from BD Biosciences (Becton Dickinson, USA) at concentrations of $c_{AB,sol} = 25$ μg/ml and 50 μg/ml, respectively. To obtain an estimate for non-specific binding and binding mediated by interaction with Fc-receptors, polyclonal mouse IgG1 (50 μg/ml bottling concentration, BD Biosciences, USA) was used as an isotype control. Representatively, the structure of an IgG1 an-

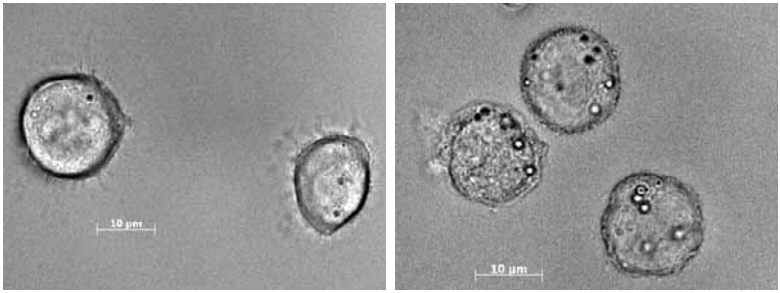

(a) KARPAS-299 cells. (b) U-937 cells.

Figure 7.1: Microscopic images of human tumour cells used in the aggregation experiments in PBS. The images were recorded with a Zeiss Axio Imager.A1. The bar indicates a scale of 10 μm.

tibody is illustrated in Figure 7.2. The antibody suspensions were used as delivered without any further preparation.

To distinguish between both cell lines in the flow cytometer, KARPAS-299 cells were fluorescently stained with the lipophilic membrane dye 5-hexadecanoylaminofluorescein (H110, Invitrogen, USA). The solid dye was solved at 5 g/l in ethanol and a stock solution was obtained by diluting 1:10^5 with MilliQ water. For a validation of cell viability, propidium iodide (PI) was used which was obtained from Sigma Aldrich, USA (P4170).

7.3 Methods

7.3.1 Experimental procedures

All experiments were carried out in 50 ml polypropylene centrifuge tubes (Sarstedt, Germany) which were thoroughly rinsed with deionised water before use. Before the aggregation experiments, the cell number c_{RPMI} and viability in culture medium of both cell lines was determined with a Vi-CELL XR (Beckman Coulter, USA). The cells were collected by centrifugation at 200 g for 10 min and the cell pellet was resuspended in PBS (ionic strength $I_M \approx 0.2$ M). The resuspension volume was adjusted to

Table 7.1: Characterisation of KARPAS-299 and U-937 cell lines.

Cell line	d [a] [μm]	ζ [b] [mV]	Immunology[c] CD13	CD33
KARPAS-299	14.1	-12.6	+	-
U-937	13.8	-11.9	(+)	+

[a] determined with a Mastersizer 2000 (Malvern, UK) as the average of measurements in RPMI and PBS
[b] determined with a Zetasizer Nano ZS (Malvern, UK) as the average of measurements in RPMI and PBS
[c] determined by the German Collection of Microorganisms and Cell Cultures (DSMZ, Braunschweig, Germany). Positive, moderately positive and negative immunological results are labelled with +, (+) and -, respectively.

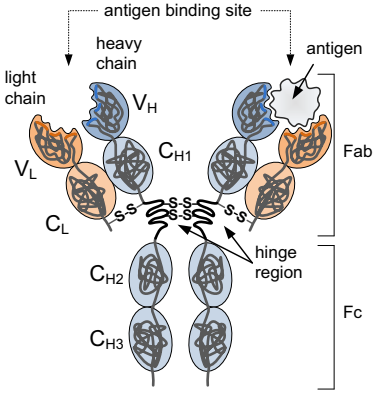

Figure 7.2: Schematic representation of an IgG1 antibody composed of four polypeptide chains: two identical heavy chains (blue colour) each composed of one variable (V_H) domain followed by a constant domain (C_{H1}), a hinge region, and two more constant (C_{H2} and C_{H3}) domains, as well as two identical light chains (orange colour) each with one variable (V_L) and one constant (C_L) domain connected by disulfide bonds in the hinge region. Constant Fc (fragment constant) domains and specific Fab (fragment antigen binding, i.e. antigen binding site) domains are indicated.

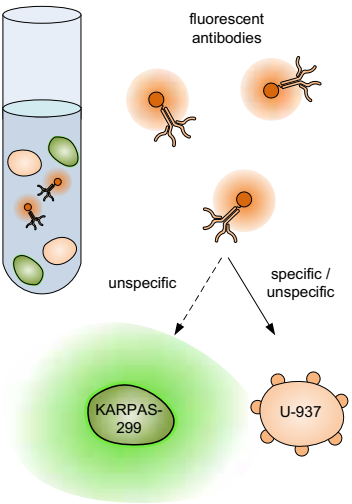

Figure 7.3: Process scheme of preferential bionanoparticle aggregation to cellular surface receptors in mixtures of KARPAS-299 and U-937 cells. KARPAS-299 cells are fluorescently stained with fluorescein (H110) while the CD13 antibody is labelled with phycoerythrin. Unspecific binding to both cell types as well as biologically specific binding to antigen-positive cells is indicated.

yield cell numbers of $c_{PBS} \approx 10^6$ cells/ml. Of all independent repetition experiments, two were analysed in detail with respect to the cellular concentrations. The results regarding cell concentration and viability are shown in Table 7.2.

KARPAS-299 cells were fluorescently labelled with small volumes of the H110 stock solution and incubated for approximately 20 min at 37°C. After incubation the cells were washed with PBS by centrifugation for 10 min at 200 g to remove excess dye which would cross-label U-937 cells in mixtures of both cell types. Flow cytometric measurements showed that the cell lines could be distinguished very well when 1 μl H110 stock solution was added per 10^6 cells. The stock solution volume was determined from the concentration of cells in the PBS solution c_{PBS} of Table 7.2, so that similar fluorescence is achieved and compensation in the flow cytometer does not have to be adjusted for each experiment (section 7.3.2). The cells were mixed in a 1:1 volumetric ratio. The resulting KARPAS-299 to U-937 cell ratio was confirmed by flow cytometry and varied in an interval from 0.74:1 to 1.56:1. In exceptions, large deviations were corrected manually by dilution. The cell ratios determined from flow cytometry are shown in Figure 7.6 listed for several independent experiments. On average a satisfactory ratio of $c_{\text{KARPAS-299}}/c_{\text{U-937}} = 1.09$ was obtained.

Table 7.2: Concentration and viability characterisation of the cell lines measured with a Vi-CELL XR.

Cell line	Experiment	c_{RPMI} [10^6 cells/ml]	c_{PBS} [10^6 cells/ml]	Viability in PBS[a] [%]
KARPAS-299	1	0.82	0.93	91.4
	2	0.82	1.19	86.6
U-937	1	0.87	1.06	91.5
	2	1.38	1.10	87.3

[a] automatically determined by Vi-CELL XR with tryptan blue dye exclusion method

Table 7.3: Calculation of cell specific antibody amount for IgG1, CD13 and CD33.

Antibody - fluorophor	m_{AB-PE}[a] [10^{-13} μg]	ratio [AB/cell]	m^{tot}_{AB-PE} [10^{-5} μg/cell]	$c_{AB-PE,sol}$[b] [μg/ml]	$V^{tot}_{AB-PE,sol}$ [μl/10^6 cells]
IgG1-PE	6.48	10^6	6.5	50	12.95
CD13-PE	6.48	10^6	6.5	25	25.90
CD33-PE	6.48	10^6	6.5	50	12.95

[a] calculated from $\overline{M}_{AB}$ = 150 kDa and $\overline{M}_{PE}$ = 240 kDa with 1 Da = 1 u = $1.66054 \cdot 10^{-18}$ μg. A single PE molecule per antibody was assumed and molar masses were provided by BD Biosciences.
[b] provided by BD Biosciences

The aggregation experiments with bionanoparticles in binary mixtures of human tumour cells are schematically illustrated in Figure 7.3. They were conducted at a bionanoparticle concentration ratios of 10^6 AB/cell. From this, the added bionanoparticle solution volumes $V^{tot}_{AB,sol}$ per cell were calculated for each antibody type according to Table 7.3. At $t = 0$ the antibody solution was pipetted to the cell mixture, incubated at 37°C, and dispersed by gently tipping the tube upside down once, similar to the procedure for the particle systems. Further gentle shaking was performed immediately before taking samples in order to resuspend the cells homogeneously. As in Part II, we assume that cells and antibodies are perfectly mixed inside the medium. Although this is hardly achieved instantaneously upon the start of each experiment in perikinetic regimes, a mean-field approach seems to be justified. Samples of 500 μl volume were taken at $t = 2$, 5, 10, 20, 40 and 60 min. Aggregation was terminated by diluting each sample with 500 μl PBS stored on ice and by separating the remaining unbound antibodies by centrifugation for 5 min at 200 g. Cells were resuspended in 300 μl PBS to obtain a slightly higher concentration for flow cytometric analysis.

7.3.2 Flow cytometric analysis of biocolloids

To detect the aggregation of antibodies to the tumour cells, the Epics-XL flow cytometer was used. A detailed description of the working principle and the evaluation of the scattering signals in distribution dot plots was presented in section 3.2.1. Living cells were discriminated from dead cells, cell debris or other particulate contaminants by analysing forward (FS) and side (SS) scatter data. For a sample measurement, the dot plots are shown in Figure 7.4(a) and 7.4(b). Cells were distinguished on the $FL1$ channel, while the aggregation process was detected via the evolution of the $FL3$ signal, as plotted in Figure 7.4(c). In all experiments, the standard FS intensity is based on the peak area signal and a FS discriminator value of 30 a.u. was used. Prior to the

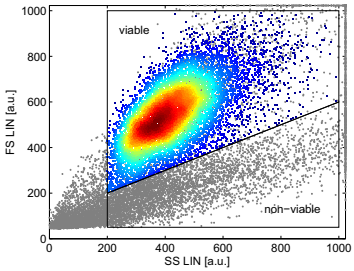

(a) Forward scatter (*FS*) versus side scatter (*SS*) plot showing the gates for viable and non-viable (dead) cells.

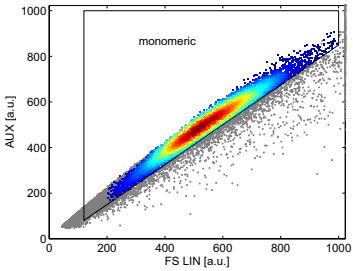

(b) Forward scatter peak signal (*FS Peak*) versus forward scatter area signal (*FS*) with the gate for monomeric cells.

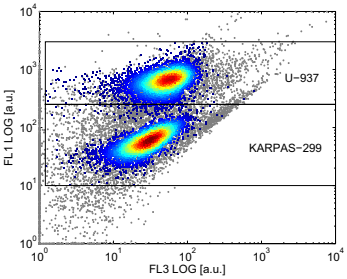

(c) Dot plot of *FL*1 versus *FL*3 fluorescence intensity (compensation *FL*1=23.4%). Gates for KARPAS-299 and U-937 cells are indicated.

Figure 7.4: Flow cytometric analysis of a cell mixture without bionanoparticles. Positive events are coloured by density.

experiments, the detector voltages of all considered channels *FS*, *SS*, *FL*1 and *FL*3 were calibrated in order to detect all events in appropriate regions. The *FL*3 intensity was aimed at 10^1 a.u. for antibody-free cells.

By plotting *FS* over *SS* different regions are visible which could be identified as viable and dead cells as well as cell debris and other particulate contamination at small scattering intensities (Figure 7.4(a)). A plot of the *FS Peak* signal against the area based *FS* intensity identifies multimeric cell agglomerates, which would appear as separate peaks below the diagonal of the gate[44]. In the tumour cell mixtures hardly any cell agglomerates formed over the whole experiment (Figure 7.4(b)). Cell viability was validated by a propidium iodide (PI) test. The dye PI fluorescently marks dead cells because it only penetrates ruptured cell membranes. Stained dead cells can be distinguished from unstained viable cells on an *FL*2 vs. *FL*3 plot by their higher fluorescence intensity. Cells were dyed with a cell specific volume of $V_{PI} \approx 5 \cdot 10^{-6}$ μl/cell directly before analysis. Figure 7.5 shows the results of the PI viability test, where cells considered as viable in Figure 7.4(a) are coloured in blue and inviable cells in red. The gates for viable and non-viable cells in Figure 7.4(a) match the result from PI staining to great extents. The overlap is considered as negligible, especially its influence on the total cell population.

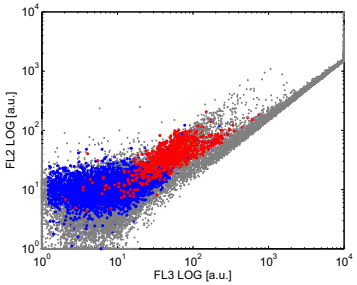

Figure 7.5: Overlay of cell viability tests with propidium iodide (PI) on separate KARPAS-299 and U-937 cell populations in the $FL2$ over $FL3$ fluorescence intensity plot. Viable, monomeric cells gated as in Figure 7.4 are coloured in blue, monomeric cells from the non-viable gate are displayed in red. Events outside the viable and non-viable gates from Figure 7.4(a) as well as outside the monomeric gate from Figure 7.4(b) are shown in grey.

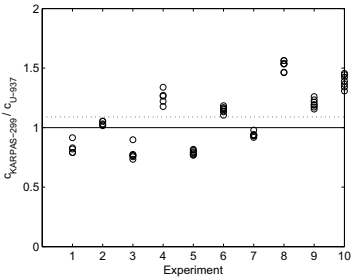

Figure 7.6: Validation of KARPAS-299 to U-937 cell ratio from flow cytometric data. The average ratio over all plotted data is $c_{\text{KARPAS-299}}/c_{\text{U-937}} = 1.09$.

Due to the staining of KARPAS-299 cells with H110, the cell lines can be differentiated by the $FL1$ fluorescence intensity. The ratio of viable monomeric KARPAS-299 to U-937 cells can thus be obtained for each experiment and is shown in Figure 7.6. The antibody aggregation dynamics were analysed in a two-dimensional $FL1$-$FL3$ dot plot, as shown in Figure 7.4(c). Due to the intense staining by H110 the fluorescence cross-over from the $FL1$ channel into the $FL3$ channel due to a smeared out emission spectrum had to be compensated by 23.4%. The compensation is quite high but guarantees an accurate discrimination between both cell populations. No compensation was necessary for the PE cross-over from $FL3$ into $FL1$. Every measurement was terminated after detection of 20000 events but latest after 100 s, always requiring less than 300 μl sample volume.

As already discussed for particles in Chapter 5, a direct quantification of antibody numbers remains difficult in flow cytometry. A calibration is necessary, by which the measured fluorescence is related to an equivalent number of fluorophore molecules. In contrast to particle systems, where the particles can be counted microscopically, this can only be achieved by MESF (mean equivalents of soluble fluorochrome[44]) calibration kits for antibodies. While the assumption that each antibody is labelled with only one fluorochrome molecule is usually satisfied (but not guaranteed for by the manufacturer), a remaining uncertainty regarding the fluorescence intensity of the fluorophores from different companies and different flow cytometers persists. Therefore, the exact antibody number was not quantified and the comparison to simulation results in Chapter 8 is performed on a relative basis only.

7.4 Antibody targeting dynamics

Preferential antibody aggregation dynamics in mixtures of human tumour cells were investigated for IgG1, CD13 and CD33 antibodies by means of flow cytometry. In our studies KARPAS-299 and U-937 cells were selected as model human tumour cell lines. The antibodies were fluorescently labelled with PE, while KARPAS-299 cells were stained with FITC. As described above, gates were established in a $FL1$-$FL3$ plot to determine the aggregation dynamics separately for each cell type. The mean $FL1$ intensities for KARPAS-299 and U-937 cells remained nearly constant throughout the experiments and enabled the distinction between both cell-types.

The aggregation dynamics with PE labelled antibodies in terms of the averaged absolute $FL3$ fluorescence intensity is shown in Figure 7.7(a) for a single representative experiment. As can be clearly seen, the cell lines deviate by an initial offset. This is caused by different autofluorescence intensities associated with the individual cell types. Assuming a constant mean offset throughout the experiments, the autofluorescence can be corrected for by subtracting the initial fluorescence intensity $FL3_{/}^{m,0}$ from the actual signal value $FL3_{AB}^{m}(t)$.

Furthermore, the fluorescence intensity may include antibody binding beyond that of the respective target antigens. These artifacts can be identified by an isotype control with mouse IgG1. The use of mouse IgG1 guarantees that the Fab region of the antibody (Figure 7.2) is non-specific against any human antigens, so that any detected binding has to be associated with Fc receptors. Although the adsorption to Fc receptors is biologically specific, it cannot be considered as target specific and is therefore categorised as an unspecific interaction in Chapter 8. Isotype control experiments were run parallel to the CD13 and CD33 experiments. The difference of CD13 or CD33 binding to IgG1 binding indicates the degree of targeted, i.e. receptor-specific binding. Corrected antibody binding dynamics are then obtained from $FL3_{AB}^{m}(t) - FL3_{IgG1}^{m}(t) - FL3_{/}^{m,0}$. Any comparison of experimental data should be based on these differences and not on total fluorescence intensities.

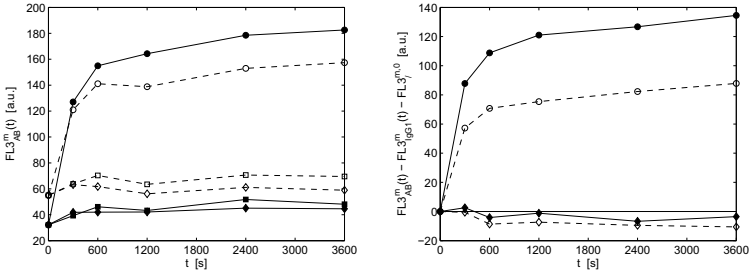

(a) Detected mean absolute $FL3_{AB}^{m}(t)$ fluorescence intensity.

(b) Mean $FL3_{AB}^{m}(t)$ intensity corrected by the respective mean autofluorescence $FL3_{/}^{m,0}$ and IgG1 isotype control $FL3_{IgG1}^{m}(t)$.

Figure 7.7: Experimental aggregation dynamics of IgG1 (□), CD13 (○) and CD33 (◇) antibodies on KARPAS-299 (– –, open symbols) and U-937 (——, filled symbols) cells measured by flow cytometry. Lines represent linear interpolations between measurements.

The resulting dynamics are shown in Figure 7.7(b). For CD13 antibodies they indicate a classical saturation behaviour towards an equilibrium value towards the end of the experiment, while for CD33 the results even underscore untargeted IgG1 binding throughout the experiment. This is a strong indication for a complete lack of CD33 receptor protein expression on the cell surfaces, which was not expected for the U-937 cells and contrasts manufacturer information presented in Table 7.1. For the CD13 antibody, differences between the two cell types can be noticed that indicate selective (preferential) aggregation. Generally U-937 cells bind more antibodies than KARPAS-299 cells, as was validated by several repetitions. All final corrected fluorescence intensities are plotted in Figure 7.8, separated according to cell type and experiment.

The selectivity of U-937 cells over KARPAS-299 cells is unexpected if compared to the information from DSMZ presented in Table 7.1. But different receptor expression levels are not uncommon and present one of the major obstacles in an efficient drug targeting. Without reproducible specificity regarding cellular receptor expression, targeted delivery of carrier particles becomes very difficult and other routes might be better suited. Even in our studies the reproducibility regarding the antibody binding proved to be highly sensitive to the extent of surface receptor expression. Although the antibodies generally did indicate preferential binding, differences between the final antibody binding become clearly visible in Figure 7.8 and the extent of preferentiality in most repetitions does not reach expected levels. Although the cells were cultured and treated identically throughout all experiments, in some experiments only insignificant differences are observed, in two experiments the preferentiality is inverse to the majority of experiments. It is assumed that the large deviations between the individual experiments are caused by different expression levels of receptor antigens. This is strongly supported by large variations in verification measurements against CD13 receptors reported by the cell supplier DSMZ. That would explain the classification of U-937 cells as weakly positive with respect to CD13 (Table 7.1). In addition to the sources of error discussed above regarding mixing, hydrodynamic

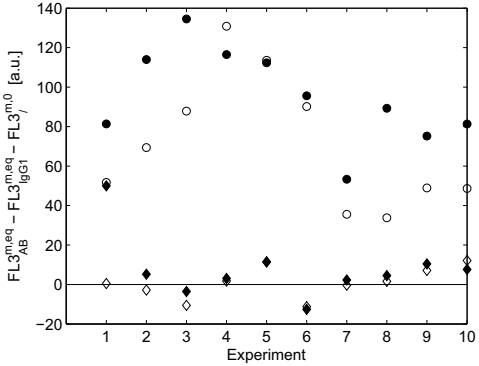

Figure 7.8: Reproducibility of antibody aggregation experiments shown as final corrected equilibrium fluorescence intensities at $t = 3600$ for CD13 (○) and CD33 (◇) antibodies on KARPAS-299 (open symbols) and U-937 (filled symbols) in 10 independent experiments. Preferential aggregation is identified by large discrepancies of KARPAS-299 and U-937.

conditions and flow cytometric measurements, some additional sources of error are discussed in the context of comparison to simulation results in section 8.3.3.

7.5 Summary

As a prerequisite for cellular uptake by endocytosis for drug targeting purposes, the preferential aggregation of antibodies to different human tumour cell lines (U-937 and KARPAS-299) in a perikinetic environment was investigated by flow cytometry. In contrast to the majority of investigations dealing with drug delivery, our studies focus only on targeted adsorption of antibodies in a deliberately simple and well defined system of suspension cells. Using this approach, the first of several further transport limitations is systematically resolved and any final uptake of antibodies into the cell is irrelevant. Two-dimensional distributions were recorded from which the aggregation dynamics of viable cells were gained separately for each cell type by appropriate gating. During the experiments the cells remained monomeric. For each cell type, CD13 adsorption followed a classical saturation behaviour towards a steady-state equilibrium coverage, while CD33 did not indicate any binding. A quantification of the adsorbed antibody number was not performed and corrected fluorescence intensities were studied instead. The saturation curve depends on the different extent of receptor surface expression on KARPAS-299 and U-937 cells. The reproducibility of the studies was found to be highly sensitive to this quantity, which varied between individual experiments. The results indicate that CD13 antibodies preferentially target U-937 cells compared to KARPAS-299 cells. This confirms that carrier particles functionalised with antibodies provide a feasible route to specifically address cells which exhibit selective expression of a corresponding antigen protein. Selective drug delivery to target cells might represent a future application of this principle.

Chapter 8

Population balance simulation of preferential aggregation

Although abundant literature regarding carrier design and cellular uptake has been published in recent years, systematic approaches to model the dynamics of targeted aggregation phenomena for property-distributed systems of cell populations are less frequent, especially on the basis of colloidal phenomena and population balance equations. On the single particle scale, adsorption models were developed for particle aggregation[98,101] and biologically mediated receptor-ligand aggregation[6,30,153]. On the population scale, some simulations were conducted in the context of virus infection regarding the adsorption and uptake of viruses by cells[43,137]. These models are based on macroscopic ODE models with kinetics fitted to experimental data. Aggregation and fragmentation processes of DNA-mediated assembly have also been studied by Monte Carlo simulations[108].

In this chapter, a property-discrete population balance model in terms of three internal coordinates, which quantify the number of particles or cells in an aggregate, was formulated to describe the dynamics of the preferential aggregation phenomena. Assuming homogeneous mixing of antibodies and cells throughout the medium in the considered system, a deterministic mean-field approach is expected to deliver a reasonable representation of the process. Any structural changes taking place within the receptor and ligand proteins during the aggregation process remain unconsidered. Furthermore, any intercellular aggregation is neglected, in accordance with the experimental evidence of Chapter 7. Adopting an analogous model structure as in Chapter 6, first the aggregation kinetics are established in section 8.1. Conceptually identical deterministic models from colloid science were adapted to biological applications with strongly heterogeneous surface characteristics. Aggregation primarily depends on Brownian motion, receptor coverage and receptor-ligand interaction potentials. The trivariate population balance equation and its property-discrete state space are defined in section 8.2. Similar to particle systems in Part II, each coordinate of state space is assumed to represent the orientational and morphological average over all clusters containing the respective number of constituent particles. The investigations for antibodies are complemented with simulations for biofunctionalised carrier particles, that differ in size and assumed ζ-potential. Finally, simulated antibody aggregation dynamics are compared to experimental data from Chapter 7.

8.1 Aggregation kernel

The experimental aggregation dynamics for antibodies were presented in Chapter 7. The results imply that the process is kinetically limited and demands a kinetic rather than an equilibrium treatment. In contrast to the predominant equilibrium approaches for numerous biological processes, kinetic models from colloidal sciences are applied for the preferential heteroaggregation of bionanoparticles. Consequently, bionanoparticles and cells are abstracted as different spherical particle species with aggregation rates that are defined by encounter frequency and sticking efficiency as before.

For the following discussion, the ternary system of bionanoparticles, KARPAS-299 and U-937 cells is written in a pseudo-binary notation with i and j expressing the species and number of bionanoparticles inside an aggregate respectively. This is permitted by the exclusion of intercellular aggregation, as will be shown during the development of the state space in section 8.2.1. The species index i represents bionanoparticles ($i = 1$), KARPAS-299 ($i = 2$) and U-937 cells ($i = 3$). The number of bionanoparticles can adopt any whole number between zero and a certain maximum number j^{max}. The adsorption of a monomeric or aggregated bionanoparticle $P'_{1,j}$ to an uncovered cell $P''_{i,0}$ thus yields an aggregate $P_{i,j}$.

8.1.1 Encounter frequency

The frequency of encounters is subject to essentially the same influences as in particle systems, which were discussed in section 6.1.1. For perikinetic regimes, the encounter frequency $\omega^F_{P',P''}$ is therefore calculated on basis of Eq. (6.4). It involves temperature T and dynamic viscosity η as well as antibody and cell radii. The mixed cell suspension was incubated at $T = 310$ K in order to guarantee the survival of the cells, and the viscosity of the culture medium PBS was approximated by that of pure water $\eta = 1 \cdot 10^{-3}$ Pas. The size difference between antibody and cells is expressed by the dimensionless aggregate volume ν_P, which is determined by assuming a fractal geometry. For bionanoparticle homoaggregates it is given by $\nu_P = j$ where j denotes the number of bionanoparticles inside a homoaggregate. For bionanoparticle-cell heteroaggregates $\nu_P = 1 + j_i \left(r_1/r_i\right)^3$ is obtained from Eq. (2.27) with $i = 2, 3$ representing KARPAS-299 and U-937 cells, respectively. At an electrolyte concentration of $I_M = 0.2$ M for PBS, the homoaggregation of bionanoparticles, antibodies in particular, is considered as diffusion limited and $d_f = 1.8$ was chosen as fractal dimension[88]. For the heteroaggregation of bionanoparticles with cells, deviations from the spherical shape of the cells are negligible due to the extreme difference in size. Therefore, a fractal dimension of $d_f = 3$ was assumed and with $r_{1,0} \ll r_{i=\{2,3\},0}$ hardly any influence is observed regarding the aggregate size for antibody targeting. For the targeting with functionalised particles at elevated ionic strength, however, noticeable effects of increasing aggregate size on the targeting dynamics are expected.

8.1.2 Sticking efficiency

The specificity of bionanoparticle interactions with cellular surface receptors expresses substantial surface heterogeneities. To discriminate specific interactions with cel-

lular receptors from unspecific interactions on the remaining surface, characteristic surface patches are established to model the efficiency of an encounter[98]. The efficiency is given by Eq. (6.10) which is repeated here for convenience

$$\omega^{E}_{P',P''} = \frac{P_{P',P''}(\phi)}{1-\left[1-P_{P',P''}(\phi)\right]\ P^{c}_{P',P''}}\,. \tag{8.1}$$

The sticking probability $P_{P',P''}(\phi)$ and the probability of multiple collisions $P^{c}_{P',P''}$ are based on the same approach as Eqs. (6.12) and (6.11). The collision probability between two specific patches during an encounter is proportional to the surface fraction ϕ. While the coverage $\phi_{P''}$ of cells is treated more detailed in section 8.1.2.1, the bionanoparticle coverage $\phi_{P'}$ is approximated by assuming that the interactions of all bionanoparticles are radially symmetric. This yields a constant surface fraction of $\phi_{P'} = 1$ and a simplified expression for the sticking probability:

$$\begin{aligned} P_{P',P''}(\phi) &= \frac{\phi_{P'}\phi_{P''}}{W^{unspec}_{P',P''}} + \frac{\phi_{P'}(1-\phi_{P''}) + (1-\phi_{P'})\,\phi_{P''}}{W^{spec}_{P',P''}} \\ &= \frac{\phi_{P''}}{W^{unspec}_{P',P''}} + \frac{1-\phi_{P''}}{W^{spec}_{P',P''}}\,. \end{aligned} \tag{8.2}$$

The two terms correspond to unspecific and specific interactions between the respective surface patches. The quality of interaction is captured by the stability ratio W, discussed in section 8.1.2.2. Unspecific aggregation events include several effects. Apart from encounters between bionanoparticles and receptor-free surface patches, collisions between bionanoparticles and occupied cellular receptors as well as between bionanoparticles themselves are considered. They may further include target unspecific adsorption to Fc-receptors. Although this essentially represents a biologically specific process, only the Fc part of antibodies is bound independent of the Fab characteristics (Figure 7.2). Therefore target unspecific binding events are classified as an unspecific binding effects. The extent of unspecific binding is experimentally assessed by the isotype control explained in section 7.4. Figure 8.1 schematically illustrates the different surface compositions of a model cell. To reduce the modelling effort and because interaction parameters for unspecific binding to cell surfaces remain unknown, the different kinds of unspecific aggregation are collectively treated by a single term in Eq. (8.2). Finally, the probability of multiple collisions per encounter $P^{c}_{P',P''}$ is given by

$$P^{c}_{P',P''} = 1 - \frac{1}{N_{11}\ (\nu_{P'}\ \nu_{P''})^{\alpha}} \tag{8.3}$$

with fitted parameters $N_{11} = 15$ and $\alpha = 0.7$.

8.1.2.1 Cellular patch collision probability

For heterogeneous cell surfaces with receptor-free and receptor-covered patches, the patch encounter probabilities $\phi_{P''}$ for unspecific and $(1-\phi_{P''})$ for specific interactions are proportional to the respective cell surface fractions. They can be obtained from geometrical considerations. Specific interactions exist between bionanoparticles and free receptor sites. Unspecific interactions occur on the remaining cell surface $\phi_{P''}$, comprising receptor-free and bionanoparticle covered surface fractions as illustrated

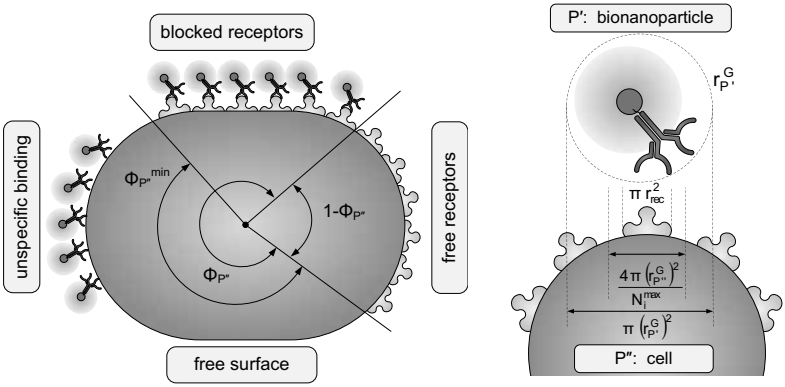

(a) Specific aggregation can only occur with free receptors, unspecific aggregation on the remaining cell surface. The surface fractions of specific ($1-\phi_{P''}$) and unspecific ($\phi_{P''}$ and $\phi_{P''}^{min}$) aggregation regions are indicated.

(b) Magnification of a binding site showing the cross-sectional areas considered in the shielding factor g_i for steric exclusion.

Figure 8.1: Schematic illustration of a heterogeneous cellular surface with receptors.

in Figure 8.1. Multiple surface heterogeneities are lumped into single representative patches for the characteristic surface compositions. The surface fraction $\phi_{P''}$ represents the weighting factor of unspecific interactions. It ranges from $\phi_{P''}^{min}$ at the beginning with exclusively free receptors to a maximum value of unity when all receptors are occupied.

Specific bionanoparticle aggregation to antigens on the cell surface is limited to the total number of expressed receptors N_i^{max}. The surface fraction of free receptors is then calculated from $1-\phi_{P''} = \left(N_i^{max} - j_i^{spec}\right)\left(r_{rec}/r_{P''}^{G}\right)^2/4$ with N_i^{max} as the total receptor number, $j_i^{spec} \leq N_i^{max}$ as the number of receptor-bound bionanoparticles and r_{rec} as the radius of a single receptor site. An exact quantification of j_i^{spec} would require a distinction of the adsorbed bionanoparticles into those specifically j_i^{spec} and those unspecifically $j_i - j_i^{spec}$ bound. The corresponding modelling effort would have to be tremendously increased by two additional property coordinates. For simplicity, we here assume that prior to full coverage the impact of unspecific binding is negligible compared to specific binding, so that $j_i^{spec} \approx j_i$ and the patch collision probability is given by

$$\phi_{P''} = \min\left\{1, 1 + \frac{g_i j_i - N_i^{max}}{4}\left(\frac{r_{rec}}{r_{P''}^{G}}\right)^2\right\} \tag{8.4}$$

not exceeding a total coverage of 1 and with g_i accounting for steric exclusion. After all receptors are saturated at $\phi_{P''} = 1$, the collision probability becomes independent of j_i^{spec} anyway, and only unspecific aggregation remains. Unspecific aggregation is not limited to monolayer coverage on the cell surfaces. Instead multilayers due to unspecific binding are possible if permitted by the interaction potentials for bionanoparticle homoaggregation $W_{P',P''}^{unspec}$. The coverage j_i^{max} of each cell type $i = 2,3$ may then exceed the maximum receptor number N_i^{max}.

Although being of minor importance for systems with low receptor coverage and small bionanoparticles, like the ones focused on in this contribution, steric shielding effects may attain a dominant influence on aggregation dynamics for cells with high coverage of large bioparticles. Then an approaching bioparticle may shield other receptors sterically from further particles and thereby decrease the probability of specific binding overproportionally. To account for additionally blocked receptors per specifically bound particle, a shielding factor g_i was introduced in Eq. (8.4). It can be estimated from geometrical considerations. Figure 8.1(b) assists in comparing the proportions of particles and receptors and by assuming an equal distribution of receptors on the cell surface, the shielding factor g_i can be derived as

$$g_i = \max\left\{1, \frac{N_i^{max}}{4}\left(\frac{r_{P'}^G}{r_{P''}^G}\right)^2\right\} \tag{8.5}$$

The lower limit of $g_i = 1$ accounts for the case without steric exclusion, when one bionanoparticle blocks exactly one receptor. For large bioparticles at high receptor densities, the exclusion effect by steric shielding increases above unity.

Common antigen expression levels on cellular surfaces can be estimated from literature. Generally they feature a broad range between 10^3 and 10^6 receptors per cell[153]. With recent advances in scanning probe microscopy, antibody binding maps have been generated from which receptor size and densities can be estimated. It could be shown that single receptors of approximately 10 to 20 nm in diameter[20] tend to form larger receptor domains on cell surfaces ranging around diameters of 50 nm[83]. Membrane pore domains range around 80 nm[130]. Based on these findings, a receptor radius of $r_{rec} = 25$ nm was assumed for our simulations. By choosing $\phi_{P''}^{min}$ as independent parameter for each cell line, the maximum number of receptors N_i^{max} can be calculated from Eq. (8.4) by setting j_i^{spec} to zero. For surface fractions of $\phi_{P''(2,j)}^{min} = 0.9991$ and $\phi_{P''(3,j)}^{min} = 0.97$ on KARPAS-299 and U-937 cells, $N_i^{max} = 200$ and $N_i^{max} = 6912$ receptors are obtained, respectively.

8.1.2.2 Receptor-ligand interaction potentials

Apart from the individual surface fractions, which represent geometric effects of aggregation, specific and unspecific interactions are characterised by potential energies contained in the Fuchs stability ratio W given by Eq. (2.3.1). The approach by Fuchs[37] was later revisited by Berg and Purcell[6] to analyse the physics of chemoreception between receptors and ligands in a biological system. The interaction energy $V_{P',P''}$ follows from the superposition of van der Waals $V_{P',P''}^{vdW}$ and electrostatic $V_{P',P''}^{el}$ energies as well as Born repulsion $V_{P',P''}^{Born}$ and biological effects between receptors and matching ligands $V_{P',P''}^{sol}$, as explained in section 2.2.3.2. The latter yield strong interactions that essentially constitute the biological specificity, for instance in immunological recognition. Biomolecules bind together extremely strong via a mechanism that is essentially a molecular 'lock and key' without establishing covalent bonds[68]. These interactions can be measured on a mesoscale with molecular probing techniques and show exponential behaviour (sections 2.2.3.2 and 2.2.4). Although detailed morphological changes of receptor and ligand during the aggregation process were not explicitly resolved, their effect on the interaction was detected. From the experimental data, mesoscale models characterising the interaction energies $V_{P',P''}^{sol}$ were gained by

Table 8.1: Parameters used in calculations of potential interaction energies. The same parameter was used for all species, except where the parameters for the individual species are given in square brackets.

Potential energy	Parameter	Value	Unit	Reference
$V^{Born}_{P',P''}(a)$	b	12	-	Feke et al.[33]
	r_σ	4	Å	Feke et al.[33]
$V^{vdW}_{P',P''}(a)$	$A_{Lipid-H_2O-Lipid}$	$4 \cdot 10^{-21}$	J	Israelachvili[68]
$V^{el}_{P',P''}(a)$	ε_r	80	-	Israelachvili[68]
	ζ_i	$[-5, -12.6, -11.9]$	mV	[a]
$V^{hydr}_{P',P''}(a)$	k^0_{hydr}	6	mN/m	Israelachvili[68]
	λ_{hydr}	0.6	nm	Israelachvili[68]
$V^{RL}_{P',P''}(a)$	k^0_{RL}	-1.5	mN/m	Leckband et al.[81]
	λ_{RL}	1.5	nm	Leckband et al.[81]

[a] determined with Zetasizer Nano ZS (Malvern, UK)

fitting. They are essentially given by the same expression in Eq. (2.19), albeit with a different set of parameters. For convenience Eq. (2.19) is copied here:

$$V^{sol}_{P',P''}(a) = 2\pi k^0 \lambda \frac{r^G_{P'} r^G_{P''}}{r^G_{P'} + r^G_{P''}} \exp\left(-\frac{a}{\lambda}\right) \tag{8.6}$$

with k^0 as extrapolated contact force and λ as the decay length. Biological specificity between an antibody and a corresponding antigen is thus expressed by a highly attractive exponential interaction potential, while unspecific interactions are expected to be similarly repulsive as those between lipid membranes. In case that the interaction energies between bionanoparticles and cells are independent of the cell type, the stability ratio for specific and unspecific aggregation only deviate with respect to these two potential energies. All model parameters used to predict the interaction potential energy are listed in Table 8.1.

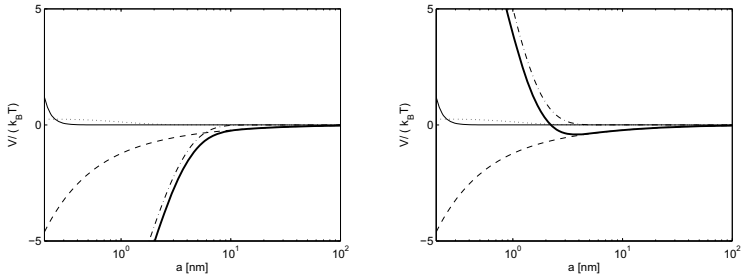

(a) Specific interaction potential. (b) Unspecific interaction potential.

Figure 8.2: Interaction potentials between bionanoparticles and cells. The potentials are essentially identical for both cell lines. The total energy (——) decomposes into contributions from Born $V^{Born}_{P',P''}$ (——), van der Waals energy $v^{vdW}_{P',P''}$ (– –), electrostatic $V^{el}_{P',P''}$ (· · ·) and specific receptor-ligand $V^{RL}_{P',P''}(a)$ (·—·—) or unspecific hydration $V^{hydr}_{P',P''}$ (·– –) energies.

The interaction potentials for specific and unspecific binding are illustrated in Figure 8.2 as functions of separation distance a. Due to their exponential nature, the solvation potentials become dominant over Born repulsion and DLVO interactions on the nanometre scale, so that $W_{P',P''}^{spec} \approx 1$ and $W_{P',P''}^{unspec} \gg 1$. As already mentioned, detailed interactions at direct contact of antibody and antigen with any induced conformational changes are not captured by this approach. But if a high binding affinity is assumed which allows the use of net aggregation rates, the detailed binding mechanism is not required for a simulation of aggregation dynamics on a mesoscale in a many body system.

8.2 Population balance model

The kernel is applied in a population balance equation to simulate the preferential aggregation bionanoparticles in an incubated mixture of human tumour cells. Due to the different extent of receptor expression on the cell surface, U-937 cells are expected to be targeted. In the following simulations, the potential interactions are assumed to be independent of cell type and therefore do not cause any aggregation bias. Similar to section 6.2, a reduced state space is established on which the population balance equation is formulated.

8.2.1 Definition of state space

In order to treat three populations, the property space $\mathcal{P}$ of the population balance model has to be three-dimensional. By excluding intercellular aggregation, the majority of coordinates is omitted and property space can be reduced to two dimensions only. Aggregation of bionanoparticles with other bionanoparticles or KARPAS-299 or U-937 cells can then be illustrated as matrix, in which the first row represents the bionanoparticles (•) and aggregates thereof, the second row the KARPAS-299 cells (◯) with $j \in [0 \ldots, j^{max}]$ bound bionanoparticles and the third row U-937 cells (●) with likewise varying bionanoparticle coverage. The property space is treated physically discrete with regard to the number of particles in each aggregate, each coordinate representing the orientational and morphological average as before. Similar to the state space established in Chapter 6.2.1, the aggregate number concentrations are stored in a concentration matrix $\underline{c}$ that is shown in Eq. (8.7):

$$\underline{c} = \begin{pmatrix} c_{1,1}\left(\bullet\right) & c_{1,2}\left(\bullet\bullet\right) & c_{1,3}\left(\bullet\bullet\right) & c_{1,4}\left(\bullet\bullet\right) & \cdots & c_{1,j^{max}} \\ c_{2,0}\left(\bigcirc\right) & c_{2,1}\left(\bigcirc\right) & c_{2,2}\left(\bullet\bigcirc\right) & c_{2,3}\left(\bullet\bigcirc\bullet\right) & \cdots & c_{2,j^{max}} \\ c_{3,0}\left(\bullet\right) & c_{3,1}\left(\bullet\right) & c_{3,2}\left(\bullet\bullet\right) & c_{3,3}\left(\bullet\bullet\bullet\right) & \cdots & c_{3,j^{max}} \end{pmatrix} \tag{8.7}$$

where the first index refers to bionanoparticles ($i = 1$) , KARPAS-299 ($i = 2$) and U-937 ($i = 3$) cells respectively and the second index $j \in [0, \ldots, j^{max}]$ to the number of bionanoparticles in each cluster. The maximum number of bionanoparticles j^{max} can theoretically equal the total amount of bionanoparticles inside the system, and would result in property spaces with many thousands of coordinates for systems with

high antibody and receptor concentrations. Since each discrete property coordinate is described by an ordinary differential equation, the full property space has to be reduced further to facilitate numerical solutions.

8.2.2 Model reduction

In addition to the two assumptions already made in section 8.2.1 concerning intercellular aggregation and morphological averaging, the state space can be reduced further by focusing on physically relevant property coordinates only. These can be identified either by using heuristic approaches for fixed cut-off boundaries or by creating an adaptive coordinate grid limiting the total amount of coordinates within the simulation to those above a certain threshold concentration. Since here the number of species is fixed to antibodies, KARPAS-299 and U-937 cells, property space is reduced by establishing an adaptive grid regarding the number of bionanoparticles j.

For each of the species i the common j^{max} can additionally be replaced by independent $j_i^{max} \leq j^{max}$. Both simplifications relieve the population balance from unnecessary equation ballast for physically irrelevant aggregation events. As before, the adaptation of property space is performed, once the sum over the final few property coordinates of either species exceeds a threshold concentration fraction ξ. Depending on the initial condition with regard to bionanoparticles $i = 1$, it is possible that the final coordinate in the reduced system cannot be filled, because formation of the specific configuration is not possible. For example, if only antibody dimers are assumed as initial condition, formation of aggregates with uneven antibody numbers is impossible.

Therefore, it can happen that the final property coordinate j_i^{max} may never be filled and the adaptation has to rely on a final few coordinates. Their number is obtained from the initial bionanoparticle distribution. For our simulations a threshold of $\xi = 1 \cdot 10^{-3}$ was chosen, which represents a compromise between system size and loss of information. Particle concentrations below the threshold are simply neglected, which is justified by the marginal loss of aggregates. As control, the absolute particle numbers were confirmed by balancing each simulation at the end. Once the threshold $\left(\sum_n c_{P\left(i,\left[j_i^{max}-n,\ldots,j_i^{max}\right]\right)} > \xi \cdot \max\left\{c_{P\left(i,\left[0,\ldots,j_i^{max}\right]\right)}\right\}\right)$ is reached for either species , the integration is terminated and property space extended by Δ_i in this row. Because breakage processes are excluded, the distribution can only evolve in direction of higher coverage j_i and the lowest property coordinate is replaced by the lowest filled coordinate $j_i^{min} = \max\left\{1, \min_j\left\{j \middle| c_{P(i,j)} > \xi \cdot \max\left[\vec{c}_{P(i,j)}\right]\right\}\right\}$ for each species i before the integration is resumed on the new state space. The extension of property space by Δ_i is heuristically adapted to the aggregation kinetics of each species. An example for a reduced system $\underline{c}^R$ is illustrated in Eq. (8.8) with neglected coordinates coloured grey:

$$\underline{c}^R = \begin{pmatrix} c_{1,\left[1,\ldots,j_1^{min}-1\right]} & c_{1,j_1^{min}} & \ldots & c_{1,j_1^{max}} & c_{1,\left[j_1^{max}+1,\ldots,j^{max}\right]} \\ c_{2,\left[0,\ldots,j_2^{min}-1\right]} & & & c_{2,j_2^{min}} \ldots c_{2,j_2^{max}} & c_{2,\left[j_2^{max}+1,\ldots,j^{max}\right]} \\ c_{3,\left[0,\ldots,j_3^{min}-1\right]} & c_{3,j_3^{min}} & \ldots & c_{3,j_3^{max}} & c_{3,\left[j_3^{max}+1,\ldots,j^{max}\right]} \end{pmatrix} . \quad (8.8)$$

For improved mathematical handling, the matrix $\underline{c}^R$ is transformed into a vector by concatenating the rows and simply omitting unfilled coordinates as shown in Eq. (8.9).

$$\vec{c}^{\,R} = \left(\; c_{P(1,j_1^{min})} \; \cdots \; c_{P(1,j_1^{max})} \; c_{P(2,j_2^{min})} \; \cdots \; c_{P(2,j_2^{max})} \; c_{P(3,j_3^{min})} \; \cdots \; c_{P(3,j_3^{max})} \; \right) \quad (8.9)$$

The index $P(i,j) = \left[j_i - j_i^{min} + 1\right] + \sum_{i=1}^{i-1} \left[j_i^{max} - j_i^{min} + 1\right]$ relates the position in the vector to the coordinates of the concentration matrix, i.e. to the kind and number of constituent particles.

8.2.3 Trivariate population balance equation

To describe aggregation in a ternary mixture of bionanoparticles with KARPAS-299 and U-937 cells only the net aggregation will be considered. In a system where breakage is considered, net rates balance particle aggregation with breakage events. Disregarding unspecific binding, this implies that aggregation ceases when all cellular receptors are occupied, and not when the equilibrium between aggregation and breakage is reached with some receptors remaining unoccupied. This approximation becomes exact whenever aggregation or breakage are not restricted by concentration and in systems with a high ratio of binding to desorption affinities. The first was ensured by adding bionanoparticles in excess to the medium in the experiments of Chapter 7, the latter had to be postulated.

With excluded intercellular aggregation and neglecting any spatial variations of concentration in the homogeneously mixed system, the population balance equation collapses to a set of three ODE systems each describing the dynamic bionanoparticle distribution for one species i. The equations can be expressed in the following compact form

$$\frac{d}{dt} c_{P(i,j)} = \frac{1}{\delta_{i1}+1} \sum_{j'=1}^{j} \omega_{P',P''} \, c_{P'(1,j')} \, c_{P''(i,j-j')} - c_{P(i,j)} \sum_{i'=1}^{2\delta_{i1}+1} \sum_{j'=\delta_{i'1}}^{\infty} \omega_{P,P'} \, c_{P'(i',j')} \quad (8.10)$$

with the Kronecker delta δ_{i1} as

$$\delta_{i1} = \begin{cases} 1, & \text{if } i = 1 \\ 0, & \text{if } i \neq 1 \end{cases} . \quad (8.11)$$

Because $c_{P'(1,j')}$ is already assigned as one educt particle in the source term, symmetry is lost and double counting avoided for particle-cell aggregation. Therefore, the prefactor has to be changed from the usual $1/2$ to unity. For bionanoparticle-bionanoparticle aggregation symmetry is maintained and the prefactor remains at $1/2$. Further use of the Kronecker delta has been made to define the summation limits in the sink term. Here, the sum over i' also depends on the species due to the restriction that aggregation between two cells is not allowed. When i is chosen as 2 for KARPAS-299 or 3 for U-937 cells, the second educt particle inside the sum is automatically specified as bionanoparticle(aggregate) with $i' = 1$ and only the sum over $i' = 1$ has to be accounted for. Also, the lower bound of j' is represented by $\delta_{i'1}$, since particles $P_{1,0}$ do not exist physically and $c_{P(1,0)} = 0$.

8.3 Simulated targeting dynamics

The preferential aggregation of CD13 antibodies to different cell types presents the main focus of this chapter. With a few changes in parameters, CD13 biofunctionalised particles were also treated. The particle property parameters are summarised in Table 8.2. The bionanoparticle concentration was chosen as $c_1 = 10^{12}$ particles/ml, while the cell lines were each assigned $c_{i=2,3} = 10^6$ cells/ml, yielding ratios of 1:1 between the cell lines and 1:10^6 between cells and particles. The PBS medium was treated as water with an elevated ionic strength of $I_M = 0.2$ M and a temperature of $T = 310$ K, matching that of the targeting experiments. Because the exact number of cellular CD13 receptors remains unknown for both cell types, it was estimated in section 8.1.2.1 from the experiments presented in the previous chapter and from literature. For KARPAS-299 cells 200 CD13 receptor domains per cell were set corresponding to $\phi_{P''(2,j)} = 0.9991$ for mean domain radii of $r_{rec} = 25$ nm. For U-937 cells a surface fraction of $\phi_{P''(3,j)} = 0.97$ was assumed that resulted in 6912 CD13 receptors. Given these receptor numbers, property space adaptations were performed with $\Delta = [30, 200, 500]$. All simulations were implemented in MATLAB and performed on a personal computer (2.66 GHz, 2 GB RAM).

Table 8.2: Characteristic bionanoparticle and cell properties used in the simulations.

Particle species	d [μm]	ζ [mV]	ϕ_P [-]	c_P [ml^{-1}]
Antibody	0.01	-5	1	10^{12}
Carrier	0.5	+40	1	10^{12}
KARPAS-299	12	-12.6	0.9991	10^6
U-937	12	-11.9	0.97	10^6

8.3.1 Kernel evaluation

The aggregation rates used in the population balance model show a characteristic distribution over state space. The distribution originates from variations in cluster properties, which affect encounter frequency and efficiency. For perikinetic systems the encounter frequency $\omega^E_{P',P''}$ only changes moderately with increasing aggregate radius and remains nearly constant over all property space coordinates. The sticking efficiency $\omega^E_{P',P''}$, however, becomes crucial in expressing distributed aggregation rates. As can be seen from Eqs. (8.1) and (8.2), the cellular surface fractions $\phi_{P''}$ and $(1 - \phi_{P''})$ as well as the stability ratios for unspecific $W^{unspec}_{P',P''}$ and specific $W^{spec}_{P',P''}$ aggregation constitute the main influences. To study them in more detail, the rate distribution is representatively shown in Figure 8.3 for a property space that is confined to $N_2^{max} = 200$ ($\phi_{P''(2,j)} = 0.9991$) receptors for KARPAS-299 cells and $N_3^{max} = 300$ ($\phi_{P''(3,j)} = 0.9987$) for U-937 cells.

In Figure 8.3(a) the interaction probability $\phi_{P''}$ is shown as matrix over all possible combinations of particle aggregation processes. For every selected particle pair P' and P'', the collision probability of receptor-free surface $\phi_{P''}$ is indicated by colour coding. The matrix is symmetric on its diagonal because P' and P'' may be exchanged. Dark blue areas indicate $\phi_{P''} = 0$. Zero-probabilities occur for all kinds of cell-cell aggregation which were excluded from the model, as well as for aggregation between particles yielding product particles which would exceed property space.

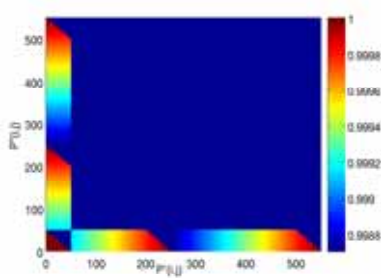

(a) Patch encounter probability $\phi_{P''}$.

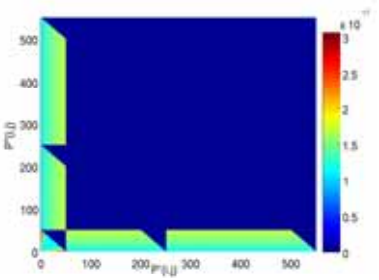

(b) Collision frequency aggregation rates $\omega^F_{P',P''}$ for pure DLVO interaction.

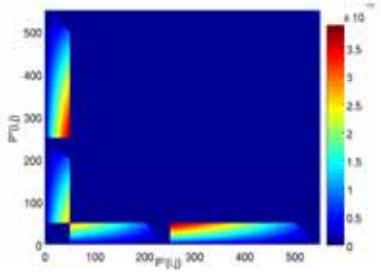

(c) Preferential aggregation rates $\omega_{P',P''}$ as function of property space coordinates $P(i,j)$.

Figure 8.3: Kernel evaluation for bionanoparticle targeting. In (a) $\phi_{P''} = 1$ for the bionanoparticles; for KARPAS-299 and U-937 cells the surface fraction for unspecific interaction increases with increasing receptor coverage. In (b) rate deviations for pure DLVO interaction result from changes in r^G_P. In (c) total aggregation rates including specific binding energies $V^{sol}_{P',P''}$ show superimposed effects of receptor coverage and fractal aggregate geometry. All rates are given in $[m^3/s]$.

The latter yields the triangular kinks. Since in our system $g_i = 1$ indicates a negligible dependence of $\phi_{P''}$ on $r^G_{P'}$, the patch collision probability $\phi_{P''}$ only changes with receptor coverage.

In a similar manner, Figure 8.3(b) shows the aggregation rates for pure DLVO interaction. At $I_M = 0.2$ M, the interaction energies are generally attractive and $W^{unspec}_{P',P''} = W^{spec}_{P',P''} = 1$. Eq. (8.2) then collapses to $P_{P',P''}(\phi) = 1/W_{P',P''} = 1$ and becomes independent of $\phi_{P''}$, so that the aggregation rates exactly match the collision frequency $\omega_{P',P''} = \omega^F_{P',P''}$. For perikinetic systems, the aggregation rate remains near $1.5 \cdot 10^{-17}$ m^3/s over the whole property space. As can be seen from Eq. (6.4), it is subject to variations of aggregate radius r^G_P. However due to the high size ratio between antibodies and cells and their different fractal dimensions d_f, only the radii of antibody aggregates change noticeably, causing a characteristic distribution of the collision frequency $\omega^F_{P',P''}$ in Figure 8.3(b).

For preferential interaction with non-zero solvation potentials the influences of $\phi_{P''}$ and r^G_P are superimposed, as is illustrated in Figure 8.3(c). Because the stability ratios are very sensitive regarding interaction energies and the patch collision probability

$(1 - \phi_{P''})$ is very low at the given antigen expression level, the rates are two orders of magnitude smaller than for pure Brownian motion. The highest rates occur for completely uncovered cells, which feature a maximum probability for specific binding. On these grounds, biological CD13 receptor-ligand interactions can be considered as rate limited (RLCA). Please note that for the given model parameters of the solvation potential the homoaggregation between antibodies remains negligible.

8.3.2 Bionanoparticle aggregation with cells

The aggregation dynamics of the preferential cell targeting by antibodies was simulated for a time-span of two hours. A 1:1 mixture of human tumour cells was incubated with antibodies at $T = 310$ K. KARPAS-299 cells were simulated with $\phi_{P''(2,j)} = 0.9991$ ($N_2^{max} = 200$) and U-937 cells with $\phi_{P''(3,j)} = 0.97$ ($N_3^{max} = 6912$). The aggregation results are summarised in Figure 8.4.

In Figure 8.4(a) the sigmoid decrease of free antibodies coincides with the increase of antibodies adsorbed either specifically or unspecifically on the cell surfaces. No distinction of specific from unspecific aggregation can be made from the integral antibody numbers. Due to the high concentration ratio of 10^6 antibodies per cell, low

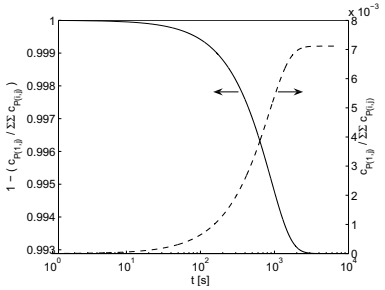

(a) Fraction of free and adsorbed antibodies.

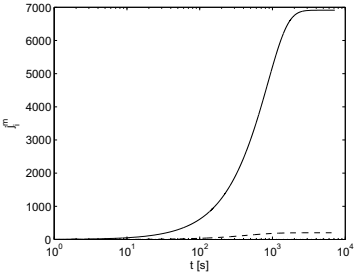

(b) Mean number of antibodies.

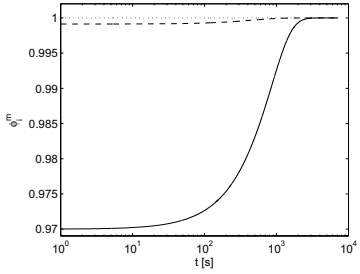

(c) Mean patch encounter probability $\phi_{P'}$ and $\phi_{P''}$ for all species.

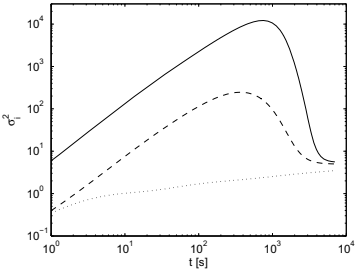

(d) Variance σ_i^2 of the distribution for all species.

Figure 8.4: Simulated antibody targeting dynamics for antibody homoaggregates (···), KARPAS-299 cells (−−) and U-937 cells (——) at $r_1 = 10$ nm, $r_{rec} = 25$ nm, $\phi^{min}_{P''(2,j)} = 0.9991$, $\phi^{min}_{P''(3,j)} = 0.97$ and the potential parameters of Table 8.1 at $T = 310$ K. All rates are given in $[m^3/s]$.

fractions follow even for absolute receptor saturation at the given receptor density. An indication of the different kinetics for both modes of aggregation can be gained from Figure 8.4(b). Here, the average amount j_i^m of antibodies in each of the three species is shown as function of time. For the antibody population only unspecific interactions were assumed in the model. This results in nearly constant aggregation until clusters contain about six antibodies on average after two hours. The aggregation of antibodies can be completely eliminated (as all unspecific aggregation) by increasing the zero-separation energies k^0_{hydr} or the decay lengths λ_{hydr} for the unspecific interaction potentials. In contrast to antibody homoaggregation, the antibody binding to KARPAS-299 and U-937 cells occurs faster due to additional specific binding. A rapid increase of total bound antibodies is evident up to the complete saturation of all cellular receptors. From then on, the amount of antibodies only increases moderately, which is not clearly visible due to the logarithmic axis scaling. The amount of bound antibodies on U-937 cells exceeds that on KARPAS-299 cells for all times because a larger surface fraction is covered with receptors. This increases the probability of an antibody-receptor collision and enhances the aggregation rate, as explained in section 8.3.1. The saturation of receptors is confirmed by Figure 8.4(c), which displays the change of the average patch-collision probability ϕ over time. At $\phi = 1$, all receptors are saturated. With increasing receptor surface fraction, the saturation time is increased. For KARPAS-299 saturation is reached after nearly 15 min, while for U-937 cells it takes about two times longer. The variance σ_i^2 for all species is shown in Figure 8.4(d) and quantifies the distribution of cells with regard to their coverage j. As expected, the distribution broadens quicker for higher aggregation rates. For antibody homoaggregates, the variance increases moderately due to slow unspecific aggregation. In contrast, the distribution of cells along the number of bound particles becomes greater with increasing extent of specific binding, so that the variance for U-937 cells exceeds that for KARPAS-299 cells. Once all receptors on a cell are saturated, only much slower unspecific aggregation events remain. The distribution narrows down considerably and asymptotically runs into that of the aggregated antibodies.

The superposition of specific and unspecific aggregation can be illustrated by variation of interaction potential parameters. Here, the zero-distance potential energy of unspecific binding k^0_{hydr} was varied. For higher values of k^0_{hydr} the unspecific stability ratio $W^{unspec}_{P',P''}$ increases, reducing the unspecific sticking probability and aggregation rates. The decreasing total amount of bound antibodies is clearly visible in Figure 8.5. A complete decoupling of the two aggregation modes is not possible when using the sticking probability $P_{P',P''}(\phi)$ of Eq. (8.2) because it lumps both effects into a single probability averaged over the whole cell surface. Information discriminating between specific and unspecific binding is sacrificed to computational efficiency by this approach.

If the antibody is replaced by a biologically functionalised carrier particle, as intended in drug targeting, different effects on aggregation dynamics are expected. First, the shielding factor g_i may attain values beyond unity which would increase the number of sterically blocked receptors per bound particle. Secondly, Brownian motion is decelerated with increasing particle size. To assess the effects on the targeting dynamics, simulations were conducted for biofunctionalised radially symmetric carriers with an assumed diameter of $d_1 = 500$ nm and a ζ-potential of $\zeta_1 = +40$ mV. The results are plotted in Figure 8.6 along with the antibody aggregation dynamics of Figure 8.4(b) for comparison. In contrast to antibodies, the carrier particles do

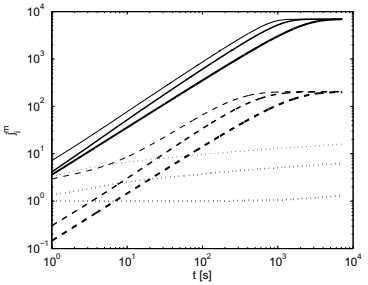

Figure 8.5: Simulated mean antibody number per antibody homoaggregate ($\cdots$), KARPAS-299 cell (– –) and U-937 cell (——) for varied unspecific interactions: $k^0_{hydr} = 4.0$ mN/m (thin lines), $k^0_{hydr} = 6.0$ mN/m (intermediate lines, from Figure 8.4(b)) and $k^0_{hydr} = 12.0$ mN/m (fat lines).

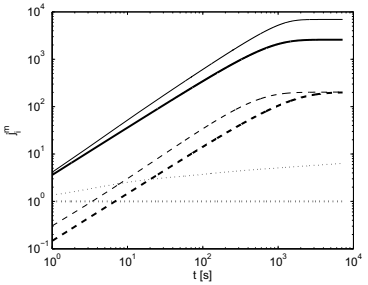

Figure 8.6: Simulated preferential aggregation of antibody-functionalised carrier particles to KARPAS-299 cells (– –) and U-937 cells (——), as well as the mean carrier number in particle clusters ($\cdots$). Carrier particles with $r_1 = 250$ nm and $\zeta_1 = +40$ mV were selected at identical concentration ratio of 10^6 particles per cell. All other interaction parameters can be taken from Table 8.1. The results are compared to antibody aggregation of Figure 8.4(b) (thin lines).

not show any homoaggregation due to their high ζ-potential which keeps them electrostatically stabilised even in PBS. Regarding the cells, particle binding is slower to both KARPAS-299 and U-937 cells than antibody binding. One reason is the reduced encounter frequency due to an increased particle radius, as follows from Eq. (6.4). A second contribution is added by the steric shielding factor g_i. In contrast to the Brownian motion, which affects both cell lines equally, the steric shielding effect deviated between the cell lines due to its dependence on the respective receptor surface fractions. Since KARPAS-299 cells only have very little receptor covered surface, the steric shielding at uniform receptor distribution remains at $g_2 = 1$. For U-937 cells, the coverage increases by a shielding factor of $g_3 \approx 3$. Steric shielding causes a decelerated binding of carrier particles, which is indicated by the reduced slope in Figure 8.6, and a reduced maximum carrier number N_3^{max} at saturation. Please note, that the radius of gyration of particle-cell aggregates $r^G_{p'}$ now increases slightly with the number of adsorbed carriers. This might cause a slight reduction of the steric shielding factor g_3 with increasing carrier number.

In summary, we have shown that the aggregation dynamics severely depends on the antibody-to-cell ratio and the receptor expression on cellular surfaces. The first determines the amount of collisions between antibodies and cells and, once a collision occurs, the second determines the probability of successful receptor-ligand interactions. Given low receptor expression levels, the aggregation rates are about two orders of magnitude lower than for the diffusion limited case, as discussed in section 8.3.1. Binding of antibodies to cellular receptors can therefore be considered as a rate limited process (RLCA). The high biological specificity in receptor-ligand interactions, expressed by the interaction potentials, is thus dominated by the mixing ratio and receptor density.

8.3.3 Comparison to experimental data

The simulation results for the targeting of antibodies are compared to the experimental data presented in Chapter 7. Since a direct quantification of antibody numbers from flow cytometric data via a calibration remains difficult, the comparison is based on relative quantities only. They are obtained from the ratio of the mean fluorescence intensity $FL3^{m}_{AB}(t)$ to the mean equilibrium intensity $FL3^{m,eq}_{AB}$ when all antigens are saturated. As before, the fluorescence intensities are corrected by autofluorescence $FL3^{m,0}_{/}$ and IgG1 binding $FL3^{m}_{IgG1}(t)$, so that dimensionless dynamics can be expressed by

$$\left(\frac{j^{m}_{i}(t)}{j^{m,eq}_{i}}\right)^{exp}_{AB} = \frac{FL3^{m}_{AB}(t) - FL3^{m}_{IgG1}(t) - FL3^{m,0}_{/}}{FL3^{m,eq}_{AB} - FL3^{m,eq}_{IgG1} - FL3^{m,0}_{/}} \tag{8.12}$$

with $AB \in \{CD13, CD33\}$. Due to this rescaling approach, experimental deviations in the final mean number of bound antibodies $j^{m,eq,exp}_{i,AB}(t)$ are eliminated, so that different absolute aggregation extents are no longer visible. For the comparison of experimental dynamics with model predictions, this presents no drawback however. The simulation results are rescaled as dimensionless fraction $\left(j^{m}_{i}(t)/j^{m}_{i}(t^{tot})\right)^{sim}_{AB}$. In the following, the comparison is restricted to the targeting dynamics of CD13 antibodies because hardly any interaction was detected for CD33 antibodies, indicating a poor expression of the corresponding antigens. The rescaled aggregation dynamics from simulations are plotted in Figure 8.7 along with the experimental data from section 7.4.

Given the model parameters applied in section 8.3.2, the aggregation dynamics of CD13 antibodies on KARPAS-299 and U-937 cells could be simulated well. To retain the focus on possible drug targeting applications, where the final transport to the cell membrane is diffusive, perikinetic conditions were assumed for all simulations. In Figure 8.7 the model predictions show a sigmoid increase of bound antibodies. When all receptors are covered, a quasi-equilibrium state is reached, where only unspecific

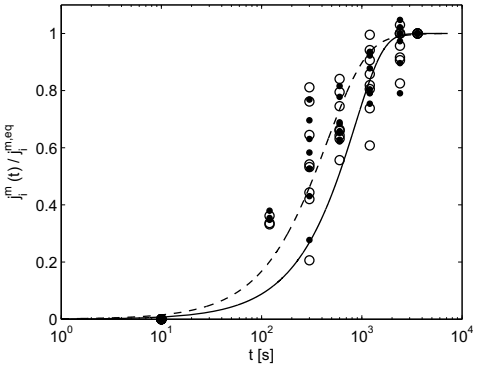

Figure 8.7: Comparison of simulated and experimental aggregation dynamics of CD13 antibodies with KARPAS-299 (– –, ○) and U-937 cells (——, •). Experimental data of eight experiments is shown.

aggregation persists as discussed in section 8.3.2. Deviations of aggregation dynamics between KARPAS-299 and U-937 cells originate from the different levels of receptor expression. For equal receptor numbers identical curves were obtained (data not shown).

Generally, a satisfactory agreement is achieved with the experimental data. The rescaled values plotted in Figure 8.7 are independent of the absolute expression level and show scattering that may still be considered as acceptable for biological systems. However, in the experimental data deviations between KARPAS-299 and U-937 cells were not observed. This could either result from methodological uncertainties or from closely matching receptor expression levels. While the latter cannot be evaluated in an exact manner due to the lacking quantification of absolute antibody numbers, several possible sources of error can be identified from the applied methods. Apart from variabilities in mixing, hydrodynamic conditions and flow cytometry - all discussed previously in section 5.2 - some additional sources of error associated with biological samples have to be considered. Biological variability might influence the expression of CD13 or C33 antigens on both cell lines, although the cultivation conditions were kept constant in all experiments. The effect of fluctuating receptor expression can be estimated from the variations of simulated KARPAS-299 and U-937 dynamics, even though it evades an absolute quantification. Furthermore, the necessity to remove free and loosely bound antibodies from the suspension before measurement, requires sample purification steps which include dilution and centrifugation. The processing of the samples probably induces additional error into the measured data.

Facing a multitude of possible errors, the introduction of some stochasticity into the model might seem beneficial. It could provide some insight into the sensitivity of the model regarding fluctuations of various input parameters, for instance the number of receptors expressed on the cell surfaces. However, an influence of stochastic fluctuations beyond the initial condition is expected to remain negligible for the considered many-body-systems. Thus the population balance model as applied throughout this thesis was selected to remain purely deterministic without the intention of incorporating any spatial or temporal fluctuations. Some variabilities might be reduced by increased model detail. For instance fluctuations regarding the homogeneity of mixing, could be considered by coupling the population balance to fluid mechanical simulations. This would retain the deterministic character of the model, but cause a tremendous increase in model complexity that is expected to impede a quick numerical solution. The application of alternative modelling techniques, like Brownian or molecular dynamics simulations, might present a further approach of increasing the model detail. These methods could deliver valuable geometric and hydrodynamic information during the aggregation process. However, simulations would be limited to rather small population ensembles. The establishment of adequate combinations of simulation approaches is an area of ongoing research. Such approaches could obtain detailed aggregation rates from microscale simulations and use them in meso- or macroscale population balance models for large particle ensembles.

8.4 Summary

As an essential step in the targeted delivery of drugs by means of cellular uptake by endocytosis, the preferential aggregation of antibodies or antibody-functionalised carrier particles to different human tumour cell lines was investigated by a trivariate population balance model. By neglecting intercellular aggregation in accordance with experiments and by defining an adaptive grid with maximum resolution in areas with high particle or cell densities based on an heuristic approach, the discrete property space was considerably reduced without the need to apply any global approximation method. The rates for bionanoparticle-bionanoparticle and bionanoparticle-cell aggregation are directly linked to the property space coordinates by deterministic models from colloidal sciences which were adapted to biological interactions. While the encounter frequency is described by the nearly constant Smoluchowski kernel for Brownian motion, the sticking efficiency is modelled by a kernel considering inhomogeneous surface patches. Here, a decisive influence is attributed to the patch encounter probability and the interaction potential energies within the stability ratio.

Given a cell specific receptor density as input parameter, the preferential aggregation of bionanoparticles to U-937 cells in mixture with KARPAS-299 cells was successfully simulated. In the model, unspecific and biologically specific aggregation modes are superimposed. During receptor coverage the distribution of adsorbed bionanoparticles per cell broadens considerably. After all receptors are saturated only unspecific aggregation remains and a quasi-equilibrium with a narrow distribution is obtained. The high bionanoparticle-to-cell concentration ratio and purely attractive interaction potentials are outmatched by the low probability of bionanoparticle-receptor collisions, so that biologically specific aggregation has to be considered as rate limited process.

Simulated targeting dynamics are compared to the validation experiments for IgG1, CD13 and CD33 antibody aggregation presented in Chapter 7. Since the receptor expression on the cell surfaces vary between the experiments and the quantification of adsorbed antibody numbers remains difficult, the comparison is performed on the basis of data that was appropriately scaled. The agreement is very good, considering several possible sources of error and the variability of biological systems. The results confirm the feasibility to target tumour cells with antibody-labelled bionanoparticles for selective drug delivery applications.

Chapter 9

Conclusions and outlook

In this thesis the selective targeting of human tumour cells by bionanoparticles was investigated with special emphasis on the dynamic aggregation behaviour. This process represents the essential first step in a series of transport limitations facing the cellular uptake of drug carrier particles. The underlying phenomena are strongly related to directed self-assembly processes in multi-component colloid systems. To establish adequate scientific methods, the specific interaction and heteroaggregation of multiple colloid constituents was studied in physical particulate systems first. Experimental methods primarily included flow cytometry and diverse microscopic techniques, while simulations are based on population balance equations with kernel models rooting in classical colloid science. Both approaches were then transferred to biological systems, achieving a more rigorous description of cellular targeting dynamics and efficiency which could prove valuable in future optimisation efforts with respect to drug delivery.

Experiments for physical particle systems investigated predominant heteroaggregation phenomena in binary and ternary particle mixtures in well defined environments by means of flow cytometry. Several variations of important experimental parameters, influencing the encounter frequency and sticking efficiency, were performed that compare well with benchmarks set by theoretical considerations and by literature. This validates flow cytometry as convenient and reliable tool to track multi-dimensional distributions of cluster composition. Dosage experiments in ternary particle mixtures demonstrated the high sensitivity of flow cytometric measurements and their versatile applicability. As a second experimental technique colloidal probe microscopy was employed to determine the pairwise particle interactions. Its potential to explain the macroscale aggregation behaviour by particle interactions on the microscale was demonstrated.

Regarding the aggregation process, the work focused on the predominant electrostatic de- and restabilisation phenomena which are strongly affected by the particle mixing ratio and the ionic strength of the dispersion medium. The dominant heteroaggregation phenomena in binary particle mixtures were reconstructed by population balance simulations. Two internal coordinates represented the particle species. They characterised the cluster composition and generated a property-discrete state space that was efficiently reduced to an adaptive grid by a semi-heuristic approach. The aggregation rates were modelled by two competing deterministic kernel concepts under consideration of Brownian motion and DLVO theory. The kernel for patchy-particles accounts for the heterogeneous surface structure of aggregated clusters[98], while a charge-balance kernel calculates the interaction potential between two clusters on the basis of a mean electrostatic charge. Both models were successfully tested

against experimental findings for variations of the particle mixing ratio. Although slight deviations to experimental data persist, it was shown that colloidal approaches originating from single species systems can be transferred to describe heteroaggregation in multi-species particle systems. Measurements of the ζ-potential confirm the trends resulting from the simulations.

In the next step, flow cytometric methods were applied to biological systems. The preferential aggregation of antibodies to U-937 cells in mixture with KARPAS-299 cells was studied in a perikinetic environment. Two-dimensional distributions were recorded from which the aggregation dynamics of viable cells were gained separately for each cell type by appropriate gating. For each cell type, CD13 and CD33 adsorption followed classical saturation behaviour towards a steady-state equilibrium coverage. The saturation curve depended on the different extent of receptor surface expression on KARPAS-299 and U-937 cells. This quantity was subject to considerable variation between the individual experiments and had a strong influence on the reproducibility of the studies. Nevertheless, the results confirmed that cells which exhibit selective expression of a corresponding antigen protein can be specifically targeted by antibody-functionalised drug carrier particles.

Finally trivariate population balance simulations were presented for the investigation of preferential aggregation of bionanoparticles to different human tumour cell lines. The corresponding state space was reduced to a two-dimensional adaptive grid, using a similar approach as for particle systems. The aggregation rates are directly linked to the property space coordinates by deterministic models from colloidal sciences. These were adapted to biological interactions and describe receptor proteins as inhomogeneous surface patches. Assuming a cell specific receptor density as input parameter, the preferential aggregation of bionanoparticles to U-937 cells in mixture with KARPAS-299 cells could be simulated successfully. In the model, unspecific and biologically specific aggregation modes are superimposed. High bionanoparticle to cell mixing ratios and purely attractive interaction potentials were outmatched by the low probability of bionanoparticle-receptor encounters. Therefore biologically specific aggregation has to be considered as rate limited process at low receptor expression levels.

Outlook

The investigations presented within this thesis leave ample room for further activities. The characterisation of single particle interactions on the microscale by colloidal probe microscopy demands follow-up investigations. The measured interactions would provide a solid basis to draw the final conclusions regarding their effect on macroscale aggregation. Colloidal probe microscopy could also be extended to biological samples to quantify the interaction potentials between ligands and receptors. This knowledge might in future enhance the in silico design of colloidal surface properties that yield a desired aggregation pattern and establish directed self-assembly as bottom-up fabrication method for nanodevices.

Regarding experiments by flow cytometry, a precise distinction of cluster composition at high signal intensities and the calibration of fluorescence intensity signals remain challenging. Furthermore, morphological aspects of complex clusters eluded flow cytometric detection. Structural analysis has only recently been addressed in flow cytometers that are equipped with a high speed camera and can generate snap-

shots of the passing particles. Structural analysis in experiments could be complemented by simulation approaches, either by population balance equations or other methods that yield more detailed geometric information, like Brownian dynamics. These models would predict aggregation rates from first principles that can either be used within a population balance framework or in a comparison to deterministic results. Also, the hydrodynamic conditions could be extended from perikinetic to orthokinetic regimes, thereby meeting an important requirement for many technical applications. Recent studies have shown that the aggregate structure may be subject to additional dynamic effects under the influence of hydrodynamic shear, like restructuring and breakage[5].

With respect to preferential aggregation in biological systems, the investigations provide a systematic basis for follow-up investigations of cellular carrier uptake by endocytosis. To achieve the long-term aim of optimal in vivo drug targeting several intermediate steps are proposed. Once the adsorption of antibody functionalised carrier particles to specific cells in model cell mixtures has been accomplished, perhaps even with an exact quantification of carrier numbers, the remaining transport limitations facing cellular uptake, like endocytosis and intracellular digestion, have to be tackled in well defined environments. Adding a model drug that generates an indirect but unambiguous cellular response, could present a feasible route to validate successful and selective drug administration. Although these kinds of studies are not new to the field of drug targeting, usually originating from biomedical initiatives, a systematic analysis of the essential process parameters in simple model systems is advisable. More intricate interactions of a drug within a living organism include absorption, distribution, metabolism and excretion processes. These are usually addressed in the framework of pharmacokinetics and -dynamics, which is already heavily supported by commercial software packages.

The population balance model developed in this thesis would also a be suitable basis to model other technical applications not involving drug targeting. By adding breakage events into the balance equation, dynamic equilibria could be predicted. This requires first principle models to describe the dynamics of breakage events. Some preliminary work on breakage kernels in population balance approaches can be found in the literature for single-species particle systems[2,3]. A possible application is the prediction of affinity binding constants in sorption processes. These are not only desireable in biological membrane adsorption processes but also in affinity chromatography, both applications representing purification applications up to industrial scales.

Bibliography

[1] B.D. Anderson, T. Nakamura, S.J. Russel, and K.-W. Peng. High CD46 receptor density determines preferential killing of tumor cells by oncolytic measles virus. *Cancer Res.*, 64(14):4919–4926, 2004.

[2] M.U. Bäbler and M. Morbidelli. Analysis of the aggregation-fragmentation population balance equation with application to coagulation. *J. Colloid Interface Sci.*, 316:428–441, 2007.

[3] M.U. Bäbler, M. Morbidelli, and J. Baldyga. Modelling the breakup of solid aggregates in turbulent flows. *J. Fluid Mech.*, 612:261–289, 2008.

[4] R.C. Ball, D.A. Weitz, T.A. Witten, and F. Leyvraz. Universal kinetics in reacion-limited aggregation. *Phys. Rev. Lett.*, 58(3):274–277, 1987.

[5] V. Becker, E. Schlauch, M. Behr, and H. Briesen. Restructuring of colloidal aggregates in shear flows and limitations of the free-draining approximation. *J. Colloid Interface Sci.*, 339(2):362–372, 2009.

[6] H.C. Berg and E.M. Purcell. Physics of chemoreception. *Biophys. J.*, 20:193–219, 1977.

[7] G. Binnig, C.F. Quate, and C. Gerber. Atomic force microscope. *Phys. Rev. Lett.*, 56(9):930–933, 1986.

[8] M. Borkovec and G. Papastavrou. Interactions between solid surfaces with adsorbed polyelectrolytes of opposite charge. *Curr. Opinion Colloid Interface Sci.*, 13:429–437, 2008.

[9] M.S. Bowen, M.L. Broide, and R.J. Cohen. Determination of cluster size distributions using an optical pulse particle-size analyser. *J. Colloid Interface Sci.*, 105 (2):605–616, 1985.

[10] M.S. Bowen, M.L. Broide, and R.J. Cohen. Temporal evolution of the cluster size distribution during brownian coagulation. *J. Colloid Interface Sci.*, 105(2): 617–627, 1985.

[11] H. Briesen. *Modelling of suspension crystallization processes with complex particle characterization*. Habilitation thesis, RWTH Aachen, March 2008.

[12] H.-J. Butt. Measuring electrostatic, van der waals, and hydration forces in electrolyte solutions with an atomic force microscope. *Biophys. J.*, 60:1438–1444, 1991.

[13] H.-J. Butt, M. Jaschke, and W. Ducker. Measuring surface forces in aqueous electrolyte solution with the atomic force microscope. *Bioelectrochem. Bioenerget.*, 38:191–201, 1995.

[14] H.-J. Butt, B. Cappella, and M. Kappl. Force measurements with the atomic force microscope: Technique, interpretation and applications. *Surf. Sci. Rep.*, 59: 1–152, 2005.

[15] P. Carmeliet and R.K. Jain. Angiogenesis in cancer and other diseases. *Nature*, 407:249–257, 2000.

[16] M. Cerbelaud, A. Videcoq, P. Abélard, C. Pagnoux, F. Rossignol, and R. Ferrando. Heteroaggregation between Al_2O_3 submicrometer particles and SiO_2 nanoparticles: Experiment and simulation. *Langmuir*, 24(7):3001–3008, 2008.

[17] J.A. Champion and S. Mitragotri. Role of target geometry in phagocytosis. *PNAS*, 103(13):4930–4934, 2006.

[18] D.L. Chapman. A contribution to the theory of electrocapillarity. *Phil. Mag.*, 25 (6):475–481, 1913.

[19] D.A. Christian, A. Tian, W.G. Ellenbroek, I. Leventhal, K. Rajagopal, P.A. Janmey, A.J. Liu, T. Baumgart, and D.E. Discher. Spotted vesicles, stripped micelles and janus assemblies induced by ligand binding. *Nature Mat.*, 8:843–849, 2009.

[20] L.A. Chtcheglova, J. Waschke, L. Wildling, D. Drenckhahn, and P. Hinterdorfer. Nano-scale dynamic recognition imaging on vascular endothelial cells. *Biophys. J.*, 93:L11–L13, 2007.

[21] P.N. Dean, C.B. Bagwell, T. Lindmo, R.F. Murphy, and G.C. Salzman. Data file standard for flow cytometry. *Cytometry*, 11:323–332, 1990.

[22] P. Debye and F. Bueche. The dielectric constant of polystyrene solutions. *J. Phys. Colloidal Chem.*, 55(2):235–238, 1951.

[23] B. Derjagiun and L. Landau. Theory of the stability of strongly charged lyophobic sols and of the adhesion of strongly charged particles in solutions of electrolytes. *Acta Physicochimica URSS*, 14(6):633–662, 1941.

[24] B. Derjaguin. Untersuchungen über die Reibung und Adhäsion, IV. *Kolloid.-Z.*, 69(2):155–164, 1934.

[25] W. Dittrich and W. Göhde. Impulsfluorometrie bei einzelzellen in suspensionen. *Z. Naturforschung B*, 24(3):360–361, 1969.

[26] D.C. Drummond, M. Zignani, and J.C. Leroux. Current status of pH-sensitive liposomes in drug delivery. *Prog. Lipid Res.*, 39:409–460, 2000.

[27] W.A. Ducker, T.J. Senden, and R.M. Pashley. Direct measurement of colloidal forces using an atomic force microscope. *Nature*, 353:239–241, 1991.

[28] W.A. Ducker, Z. Xu, and J.N. Israelachvili. Measurements of hydrophobic and dlvo forces in bubble-surface interactions in aqueous solutions. *Langmuir*, 10: 3279–3289, 1994.

[29] M. Elimelech, J. Gregory, X. Jia, and R.A. Williams. *Particle Deposition and Aggregation: Measurement, Modelling and Simulation*. Butterworth-Heinemann, 1st edition, 1995.

[30] R.G. Endres and N.S. Wingreen. Maximum likelihood and the single receptor. *Phys. Rev. Letters*, 103:158101, 2009.

[31] T.M. Fahmy, R.M. Samstein, C.C. Harness, and W.M. Saltzman. Surface modification of biodegradable polyesters with fatty acid conjugates for improved drug targeting. *Biomat.*, 26:5727–5736, 2005.

[32] F. Family, P. Meakin, and T. Vicsek. Cluster size distribution in chemically controlled cluster-cluster aggregation. *J. Chem. Phys.*, 83(8):4144–4150, 1985.

[33] D. Feke, N. Prabhu, J.A. Mann, and J.A. Mann. A formulation of the short-range repulsion between spherical colloidal particles. *J. Phys. Chem.*, 88:5735–5739, 1984.

[34] D. Felnerova, J.-F. Viret, R. Glück, and C. Moser. Liposomes and virosomes as delivery systems for anigens, nucleic acids and drugs. *Curr. Opinion in Biotech.*, 15:518–529, 2004.

[35] A. Fernández-Barbero, M. Cabrerizo-Vílchez, R. Martínez-García, and R. Hidalgo-Álvarez. Effect of the particle surface charge density on the colloidal aggregation mechanism. *Phys. Rev. E*, 53(5):4981–4989, 1996.

[36] J. Folkman. Angiogenesis in cancer, vascular, rheumatoid and other disease. *Nature Med.*, 1(1):27–31, 1995.

[37] N. Fuchs. Über die Stabilität und Aufladung der Aerosole. *Z. Physik*, 89:736–743, 1934.

[38] J.E. Fuller, G.T. Zugates, L.S. Ferreira, H.S. Ow, N.N. Nguyen, U.B. Wiesner, and R.S. Langer. Intracellular delivery of core-shell fluorescent silica nanoparticles. *Biomat.*, 29:2008, 2008.

[39] P. Galletto, W. Lin, M.I. Mishchenko, and M. Borkovec. Light-scattering form factors of asymmetric particle dimers from heteroaggregation experiments. *J. Chem. Phys.*, 123:064709, 2005.

[40] R. Gans. Über die Form ultramikroskopischer Goldteilchen. *Ann. Phys.*, 37(5): 881–900, 1912.

[41] C. Gauer, H. Wu, and M. Morbidelli. Effect of surface properties of elastomer colloids on their coalescence and aggregation kinetics. *Langmuir*, 25(20):12073–12083, 2009.

[42] A. Gerstlauer. *Herleitung und Reduktion populationsdynamischer Modelle am Beispiel der Flüssig-Flüssig-Extraktion*. Dissertation thesis, University of Stuttgart, June 1999.

[43] P.-A. Gilbert, A. Kamen, A. Bernier, and A. Garnier. A simple macroscopic model for the diffusion and adsorption kinetics of r-adenovirus. *Biotech. & Bioeng.*, 98(1):239–251, 2007.

[44] A.L. Givan. *Flow Cytometry: First Principles*. Wiley, New York, 2nd edition, 2001.

[45] S.C. Glotzer and M.J. Solomon. Anisotropy of building blocks and their assembly into complex structures. *Nature*, 6:557–562, 2007.

[46] G. Gouy. Sur la constitution de la charge électrique à la surface d'un électrolyte. *J. Phys. Radium*, 9:457–468, 1910.

[47] D.C. Grahame. The electrical double layer and the theory of electrocapillarity. *Chem. Rev.*, 41(3):441–501, 1947.

[48] J. Gregory. The role of colloid interactions in solid-liquid separation. *Water Sci. Techn.*, 27(10):1–17, 1993.

[49] D.G. Grier. Optical tweezers in colloid and interface science. *Curr. Opinion Coll. Interface Sci.*, 2(3):264–270, 1997.

[50] D.G. Grier. A surprisingly attractive couple. *Nature*, 393:621–622, 1998.

[51] H.C. Hamaker. The London-Van der Waals attraction between spherical particles. *Physica IV*, 2(10):1058–1072, 1937.

[52] C. Hanley, J. Layne, A. Punnoose, K.M. Reddy, I. Coombs, A. Coombs, K. Feris, and D. Wingett. Preferential killing of cancer cells and activated human T cells using ZnO nanoparticles. *Nanotechn.*, 19:295103, 2008.

[53] F. Hausdorff. Dimension und äusseres Mass. *Math. Ann.*, 79:157–179, 1919.

[54] C.A. Helm, W. Knoll, and J.N. Israelachvili. Measurement of ligand-receptor interactions. *Proc. Natl. Acad. Sci. USA*, 88:8169–8173, 1991.

[55] H. Helmholtz. Über einige Gesetze der Verteilung elektrischer Ströme in körperlichen Leitern. *Pogg. Ann. Phys. Chem.*, 89:211233, 1853.

[56] D.C. Henry. The cataphoresis of suspended particles: Part I - The equation of cataphoresis. *Proc. R. Soc. A*, 133(821):106–129, 1931.

[57] H. Heuberger, G. Sukhorukov, J. Vörös, M. Textor, and H. Möhwald. Biofunctional polyelectrolyte multilayers and microcapsules: Control of non-specific and bio-specific protein adsorption. *Adv. Funct. Mater.*, 15(3):357–366, 2005.

[58] A.L. Hiddessen, S.D. Rodgers, D.A. Weitz, and D.A. Hammer. Assembly of binary colloidal structures via specific biological adhesion. *Langmuir*, 16:9744–9753, 2000.

[59] F. Hilbrig and R. Freitag. Protein purification by affinity precipitation. *J. Chromatogr. B*, 790:79–90, 2003.

[60] R. Hogg, T.W. Healy, and D.W. Fuerstenau. Mutual coagulation of colloidal dispersions. *Transac. Faraday Soc.*, 62:1638–1651, 1966.

[61] E.P. Honig, G.J. Roebersen, and P.H. Wiersema. Effect of hydrodynamic interaction on the coagulation rate of hydrophobic colloids. *J. Colloid Interface Sci.*, 36(1):97–109, 1971.

[62] M.J. Hounslow, R.L. Ryall, and V.R. Marshall. A discretized population balance for nucleation, growth and aggregation. *AIChE J.*, 34(11):1821–1832, 1988.

[63] H.M. Hulburt and S. Katz. Some problems in particle technology. *Chem. Eng. Sci.*, 19:555–574, 1964.

[64] R.J. Hunter. *Foundations of Colloidal Science*. Oxford University Press, New York, 2nd edition, 2001.

[65] T.N. Hunter, R.J. Pugh, G.V. Franks, and G.J. Jameson. The role of particles in stabilising foams and emulsions. *Adv. Colloid Interface Sci.*, 137(2):57–81, 2008.

[66] A.M. Islam, B.Z. Chowdry, and M.J. Snowden. Heteroaggregation in colloidal dispersions. *Adv. Colloid Interface Sci.*, 62:109–136, 1995.

[67] J.N. Israelachvili. Measurements of hydration forces between macroscopic surfaces. *Chem. Scripta*, 25:7–14, 1985.

[68] J.N. Israelachvili. *Intermolecular and Surface Forces*. Academic Press, Amsterdam, 2nd edition, 1991.

[69] J.N. Israelachvili and G.E. Adams. Direct measurement of long range forces between two mica surfaces in aqueous KNO_3 solutions. *Nature*, 262:774–776, 1976.

[70] J.N. Israelachvili and R. Pashley. The hydrophobic interaction is long range, decaying exponentially with distance. *Nature*, 300(25):341–342, 1982.

[71] J.N. Israelachvili and D. Tabor. The measurement of van der waals dispersion forces in the range 1.5 to 130 nm. *Proc. R. Soc. Lond. A*, 331:19–38, 1972.

[72] R. Jullien and M. Kolb. Hierarchical model for chemically limited cluster cluster aggregation. *J. Phys. A*, 17(12):L639–L643, 1984.

[73] G. Kada, F. Kienberger, and P. Hinterdorfer. Atomic force microscopy in bionanotechnology. *Nano Today*, 3(1-2):12–19, 2008.

[74] D.G. Kendall. Stochastic processes and population growth. *Roy. Stat. Soc.*, 11 (2):230–264, 1949.

[75] A.Y. Kim, K.D. Hauch, J.C. Berg, J.E. Martin, and R.A. Anderson. Linear and chain-like fractals from electrostatic heteroaggregation. *J. Colloid Interface Sci.*, 260:149–159, 2003.

[76] Y. Kong and R. Parthasarathy. Modulation of attractive colloidal interactions by lipid membrane-functionalization. *Soft Matter*, 5:2027–2032, 2009.

[77] S. Kumar and D. Ramkrishna. On the solution of population balance equations by discretization I: A fixed pivot technique. *Chem. Eng. Sci.*, 51(8):1311–1332, 1996.

[78] G. Lagaly, O. Schulz, and R. Zimehl. *Dispersionen und Emulsionen*. Steinkopf, Darmstadt, 1st edition, 1997.

[79] M. Lattuada, P. Sandkühler, H. Wu, J. Sefcik, and M. Morbidelli. Aggregation kinetics of polymer colloids in reaction limited regime: experiments and simulations. *Adv. Colloid Interface Sci.*, 103:33–56, 2003.

[80] D. Leckband. The surface force apparatus - a tool for probing molecular protein interactions. *Nature*, 376:617–618, 1995.

[81] D.E. Leckband, J.N. Israelachvili, F.-J. Schmitt, and W. Knoll. Long-range attraction and molecular rearrangements in receptor-ligand interactions. *Science*, 255:1419–1421, 1992.

[82] K. Lee, T. Kim, P. Rajniak, and T. Matsoukas. Compositional distributions in multicomponent aggregation. *Chem. Eng. Sci.*, 63:1293–1303, 2008.

[83] S. Lee, J. Mandic, and J. Van Vliet. Chemomechanical mapping of ligand-receptor binding kinetics on cells. *PNAS*, 104(23):9609–9614, 2007.

[84] D.M. LeNeveu, R.P. Rand, and V.A. Parsegian. Measurement of forces between lecithin bilayers. *Nature*, 259:601–603, 1976.

[85] M.E. Leunissen, R. Dreyfus, F.C. Cheong, D.G. Grier, R. Sha, N.C. Seeman, and P.M. Chaikin. Switchable self-protected attractions in DNA-functionalized colloids. *Nature Mat.*, 8:590–595, 2009.

[86] M. Lin, W. Kobayashi, M. Skarba, C. Mu, P. Galletto, and M. Borkovec. Heteroaggregation in binary mixtures of oppositely charged colloidal particles. *Langmuir*, 22:1038–1047, 2006.

[87] M.Y. Lin, H.M. Lindsay, D.A. Weitz, R.C. Ball, R. Klein, and P. Meakin. Universal reaction-limited colloidal aggregation. *Phys. Rev. A*, 41(4):2005–2020, 1990.

[88] M.Y. Lin, H.M. Lindsay, D.A. Weitz, R. Klein, R.C. Ball, and P. Meakin. Universal diffusion-limited colloidal aggregation. *J. Phys. Condensed Matter*, 51: 3093–3113, 1990.

[89] L.J. Lis, M. McAlister, N. Fuller, R.P. Rand, and V.A. Parsegian. Interactions between neutral phospholipid bilayer membranes. *Biophys. J.*, 37:657–666, 1982.

[90] J.M. López-López, A. Schmitt, A. Moncho-Jórda, and R. Hidalgo-Álvarez. Stability of binary colloids: kinetic and structural aspects of heteroaggregation processes. *Soft Matter*, 2:1025–1042, 2006.

[91] M.R. Lorenz, V. Holzapfel, A. Musyanovych, K. Nothelfer, P. Walther, H. Frank, K. Landfester, H. Schrezenmeier, and V. Mailänder. Uptake of functionalized, fluorescent-labled polymeric particles in different cell lines and stem cells. *Biomat.*, 27:2820–2828, 2006.

[92] J. Marra and J.N. Israelachvili. Direct measurements of forces between phosphatidylcholine and phosphatidylethanolamine bilayers in aqueous electrolyte solutions. *Biochem.*, 24:4608–4618, 1985.

[93] R. McGraw. Description of aerosol dynamics by the quadrature method of moments. *Aerosol Sci. Techn.*, 27(2):255–265, 1997.

[94] P. Meakin. Formation of fractal clusters and networks by irreversible diffusion-limited aggregation. *Phys. Rev. Lett.*, 51(13):1119–1122, 1983.

[95] P. Meakin and R. Jullien. The effects of restructuring on the geometry of clusters formed by diffusion-limited, ballistic, and reaction-limited cluster cluster aggregation. *J. Chem. Phys.*, 89(1):246–250, 1988.

[96] N. Metropolis and S. Ulam. The monte carlo method. *J. Am. Stat. Assoc.*, 44 (247):335–341, 1949.

[97] G. Mie. Beiträge zur Optik trüber Medien, speziell kolloidaler Metallösungen. *Ann. Phys.*, 25(3):377–445, 1908.

[98] A. Moncho-Jordá, G. Odriozola, M. Tirado-Miranda, A. Schmitt, and R. Hidalgo-Álvarez. Modeling the aggregation of partially covered particles: Theory and simulation. *Phys. Rev. E*, 68:011404, 2003.

[99] L. Nobs, F. Buchegger, R. Gurny, and E. Allémann. Current methods for attaching targeting ligands to liposomes and nanoparticles. *J. Pharm. Sci.*, 93(8): 1980–1992, 2004.

[100] R.W. O'Brien and L.R. White. Electrophoretic mobility of a spherical colloidal particle. *J. Chem. Soc. Farad. Trans. II*, 74(1978):1607–1626, 1978.

[101] G. Odriozola, A. Moncho-Jordá, A. Schmitt, J. Callejas-Fernández, R. Martínez-García, and R. Hidalgo-Álvarez. A probabilistic aggregation kernel for the computer-simulated transition from DLCA to RLCA. *Europhys. Lett.*, 53(6):797–803, 2001.

[102] A. Olsen, G. Franks, S. Biggs, and G.J. Jameson. An improved collision efficiency model for particle aggregation. *J. Chem. Phys.*, 125:184906, 2006.

[103] A. Olsen, G. Franks, S. Biggs, and G.J. Jameson. Collision efficiency factor for heteroaggregation: Extension to soft interactions. *J. Chem. Phys.*, 128:044913, 2008.

[104] J. Olsen, K. Kokholm, O. Noren, and Sjöström. Structure and expression of aminopeptidase N, in: Advances in experimental medicine and biology: Cellular peptidases in immune functions and diseases. *International Conference on Cellular Peptidases in Immune Functions and Diseases*, 421:47–57, 1997.

[105] H. Otsuka, Y. Nagasaki, and K. Kataoka. PEGylated nanoparticles for biological and pharmaceutical applications. *Adv. Drug Delivery Rev.*, 55:403–419, 2003.

[106] R. Pasqualini, E. Koivunen, R. Kain, J. Lahdenranta, M. Sakamoto, A. Stryhn, R.A. Ashmun, L.H. Shapiro, W. Arap, and W. Ruoslahti. Aminopeptidase N is a receptor for tumor-homing peptides and a target for inhibiting angiogenesis. *Cancer Res.*, 60:722–727, 2000.

[107] A.B. Pawar and I. Kretzschmar. Fabrication, assembly, and application of patchy particles. *Macromol. Rapid Commun.*, 31:150–168, 2010.

[108] A. Pierce, A. Chakrabarti, D. Fry, and C.M. Sorensen. Computer simulation of selective aggregation in binary colloids. *Langmuir*, 21(20):2498–2502, 2004.

[109] E.G.M. Plessers, M.A. Cohen Stuart, and G.J. Fleer. Single particle optical sizing (SPOS): Design of an improved spos instrument and application to stable dispersions. *J. Colloid Interface Sci.*, 137(2):350–361, 1990.

[110] E.G.M. Plessers, M.A. Cohen Stuart, and G.J. Fleer. Single particle optical sizing (SPOS): Hydrodynamic forces and application of aggregating dispersions. *J. Colloid Interface Sci.*, 137(2):362–372, 1990.

[111] I. Popa, M. Trulsson, G. Papastavrou, M. Borkovec, and B. Jönsson. Long-ranged attractive forces induced by adsorbed dendrimers: Direct force measurements and computer simulations. *Langmuir*, 25(21):12435–12438, 2009.

[112] E.M. Pridgen, R. Langer, and O.C. Farokhzad. Biodegradable, polymeric nanoparticle delivery systems for cancer therapy. *Nanomedicine*, 2(5):669–680, 2007.

[113] A.M. Puertas, A. Fernández-Barbero, and F.J. De Las Nieves. Induced asymmetries in the heteroaggregation of oppositely charged colloidal particles. *J. Colloid Interface Sci.*, 265:36–43, 2003.

[114] B. Rabideau and R. Bonnecaze. Computational predictions of stable 2D arrays of bidisperse particles. *Langmuir*, 21(23):10856–10861, 2005.

[115] M. Radmacher, R.W. Tillmann, M. Fritz, and H.E. Gaub. From molecules to cells: Imaging soft samples with the atomic force microscope. *Science*, 257:1900–1905, 1992.

[116] D. Ramkrishna. *Population Balances: Theory and Applications to Particulate Systems in Engineering*. Academic Press, San Diego, 1st edition, 2000.

[117] S. Rentsch, R. Pericet-Camara, G. Papastavrou, and M. Borkovec. Probing the validity of the derjaguin approximation for heterogeneous colloidal particles. *PCCP*, 8:2531–2538, 2006.

[118] M. Retsch, Z. Zhou, S. Rivera, M. Kappl, X.S. Zhao, U. Jonas, and Q. Li. Fabrication of large-area, transferable colloidal monolayers utilizing self-assembly at the air/water interface. *Macromol. Chem. Phys.*, 210:230–241, 2009.

[119] S. Rollié and K. Sundmacher. Determination of cluster composition in heteroaggregation of binary particle systems by flow cytometry. *Langmuir*, 24(23):13348–13358, 2008.

[120] S. Rollié and K. Sundmacher. Tracking the clustering dynamics in ternary particle mixtures by flow cytometry. *Powder Technology*, accepted 2010.

[121] S. Rollié and K. Sundmacher. Analyse interagierender Partikel-Zell Systeme mittels Durchflusszytometrie und mehrdimensionalen Populationsbilanzen. *Chemie Ingenieur Technik*, accepted 2010.

[122] S. Rollié, H. Briesen, and K. Sundmacher. Discrete bivariate population balance modelling of heteroaggregation processes. *J. Colloid Interface Sci.*, 336(2):551–564, 2009.

[123] S. Rollié, U. Lendeckel, M. Naumann, U. Reichl, and K. Sundmacher. Dynamics of bionanoparticle targeting in mixtures of human tumour cells by validated population balance modelling. *Soft Matter*, 6(6):1203–1216, 2010.

[124] D.E. Rosner and J.J. Pyykönen. Bivariate moment simulation of coagulating and sintering nanoparticles in flames. *AIChE J.*, 48(3):476–491, 2002.

[125] D.E. Rosner, R. McGraw, and P. Tandon. Multivariate population balances via moment and monte carlo simulation methods. *Ind. Eng. Chem.*, 42:2699–2711, 2003.

[126] P.W.K. Rothemund. Folding DNA to create nanoscale shapes and patterns. *Nature*, 440:297–302, 2006.

[127] W.B. Russel, D.A. Saville, and W.R. Schowalter. *Colloidal Dispersions*. Cambridge University Press, 1st edition, 1991.

[128] P. Sandkühler. *Kinetics of Aggregation and Gel Formation in Colloidal Dispersions*. Dissertation thesis, ETH Zürich, 2004.

[129] P. Sapra and T.M. Allen. Ligand-targeted liposomal anticancer drugs. *Prog. Lipid Res.*, 42:439–462, 2003.

[130] H. Schillers, V. Shahin, L. Albermann, C. Schafer, and H. Oberleithner. Imaging CFTR: A tail to tail dimer with a central pore. *Cell. Physiol. Biochem.*, 14:1–10, 2004.

[131] A. Schmitt, G. Odriozola, A. Moncho-Jordá, J. Callejas-Fernández, R. Martínez-García, and R. Hidalgo-Álvarez. Multiple contact kernel for diffusionlike aggregation. *Phys. Rev. E*, 62(6):83359–8343, 2000.

[132] W.C. Schneider. Dielectric properties of plasticized melamine resins. *SPE Trans.*, 1(2):68–72, 1961.

[133] H.-C. Schwarzer and W. Peukert. Prediction of aggregation kinetics based on surface properties of nanoparticles. *Chem. Eng. Sci.*, 60:11–25, 2005.

[134] H.M. Shapiro. *Practical Flow Cytometry*. Wiley, Hoboken, 4th edition, 2003.

[135] D.J. Shaw. *Introduction to Colloid and Surface Chemistry*. Butterworth-Heinemann, 4th edition, 1992.

[136] H. Shen, J. Tan, and W.M. Saltzman. Surface-mediated gene transfer from nanocomposites of controlled texture. *Nature Mat.*, 3:569–574, 2004.

[137] Y. Sidorenko and U. Reichl. Structured model of influenza virus replication in MDCK cells. *Biotech. & Bioeng.*, 88(1):1–14, 2004.

[138] P.N. Singh and D. Ramkrishna. Solution of population balance equations by MWR. *Comp. Chem. Eng.*, 1(1):23–31, 1977.

[139] A.G. Skirtach, A. M. Javier, O. Kreft, K. Köhler, A.P. Alberola, H. Möhwald, W.J. Parak, and G.B. Sukhorukov. Laser-induced release of encapsulated materials inside living cells. *Angew. Chem.*, 118:1–7, 2006.

[140] C.M. Sorensen. Light scattering by fractal aggregates: A review. *Aerosol Sci. Techn.*, 35:648–687, 2001.

[141] L.A. Spielman and O. Levenspiel. A monte carlo treatment for reacting and coalescing dispersed phase systems. *Chem. Eng. Sci.*, 20(3):247–254, 1965.

[142] O. Stern. Zur Theorie der Elektrolytischen Doppelschicht. *Z. Elektrochem.*, 30: 508–516, 1924.

[143] G.B. Sukhorukov, A.L. Rogach, B. Zebli, T. Liedl, A.G. Skirtach, K. Köhler, A.A. Antipov, N. Gaponik, A.S. Susha, M. Winterhalter, and W.J. Parak. Nanoengineered polymer capsules: Tools for detection, controlled delivery, and site-specific manipulation. *small*, 1(2):194–200, 2005.

[144] D.N. Sutherland. A theoretical model of floc structure. *J. Colloid Interface Sci.*, 25(3):373–380, 1967.

[145] S. Swenson, S. Ramu, and Markland F.S. Anti-angiogenesis and RGD-containing snake venom desintegrins. *Curr. Pharm. Design*, 13:2860–2871, 2007.

[146] D. Tabor and R.H.S Winterton. Surface forces: Direct measurement of normal and retarded van der waals forces. *Nature*, 219:1120–1121, 1968.

[147] V. Uricanu, J.R. Eastman, and B. Vincent. Stability in colloidal mixtures containing particles with a large disparity in size. *J. Colloid Interface Sci.*, 223:1–11, 2001.

[148] H.C. van de Hulst. *Light Scattering by Small Particles*. Dover Publications, New York, reprint edition, 1981.

[149] M. van Dilla, T.T. Trujillo, P.F. Mullaney, and J.R. Coulter. Cell microfluorimetry: A method for rapid fluorescence measurement. *Science*, 163:1213–1214, 1969.

[150] M. Vanni. Approximate population balance equations for aggregation-breakage processes. *J. Colloid Interface Sci.*, 221:143–160, 2000.

[151] E.J.W. Verwey and J.T.G. Overbeek. *Theory of the Stability of Lyophobic Colloids*. Elsevier, Amsterdam, 1st edition, 1948.

[152] M. von Smoluchowski. Versuch einer mathematischen Theorie der Koagulationskinetik kolloider Lösungen. *Z. phys. Chem.*, 92:129–168, 1917.

[153] T.J. Wickham, R.R. Granados, H.A. Wood, D.A. Hammer, and M.L. Shuler. General analysis of receptor-mediated viral attachment to cell surfaces. *Biophys. J.*, 58:1501–1516, 1990.

[154] T.A. Witten and L.M. Sander. Diffusion-limited aggregation, a kinetic critical phenomenon. *Phys. Rev. Lett.*, 47(19):1400–1403, 1981.

[155] C.J. Wright and I. Armstrong. The application of atomic force microscopy force measurements to the characterisation of microbial surfaces. *Surf. Interface Anal.*, 38:1419–1428, 2006.

[156] D.L. Wright, R. McGraw, and D.E. Rosner. Bivariate extension of the quadrature method of moments for modelling simultaneous coagulation and sintering of particle populations. *J. Colloid Interface Sci.*, 236:242–251, 2001.

[157] F. Wurm and A.F.M. Kilbinger. Polymeric janus particles. *Angew. Chem. Int. Ed.*, 48:8412–8421, 2009.

[158] Z.P. Xu, Q.H. Zeng, G.Q. Lu, and A.B. Yu. Inorganic nanoparticles as carriers for efficient cellular delivery. *Chem. Eng. Sci.*, 61:1027–1040, 2006.

[159] H. Zhao, S. Bhattacharjee, R. Chow, D. Wallace, J.H. Masliyah, and Z. Xu. Probing surface charge potentials of clay basal planes and edges by direct force measurements. *Langmuir*, 24(22):12899–12910, 2008.

List of figures

List of tables